Applications of Fast Neutrons in the Development of Novel Sources and Detection Signatures

by

Kristofer B. Ogren

A dissertation submitted in partial fulfillment
of the requirements for the degree of
Doctor of Philosophy
(Nuclear Engineering and Radiological Sciences)
at the University of Michigan
2022

Doctoral Committee:

Professor Igor Jovanovic, Chair
Dr. Steven Dazeley
Professor Wolfgang Lorenzon
Professor Sara Pozzi

Kristofer B. Ogren

kogren@umich.edu

ORCID ID: 0000-0001-9121-1871

To Blake and Teddy

Acknowledgments

I would like to thank my advisor, Professor Igor Jovanovic. Your guidance, encouragement, and thoughtful insights inspired me to achieve more than I would have thought possible. I am grateful for the opportunities you have provided me and for all the time and effort you have devoted to my development as a scientist. I also thank the members of my dissertation committee—Professor Sara Pozzi, Professor Wolfgang Lorenzon, and Dr. Steven Dazeley—for their insights and recommendations throughout the course of the dissertation process. To Dr. Dazeley, I thank you for sharing your expertise in guiding my research for the WATCHMAN calibrations group, and for advocating for me within the collaboration.

I thank the members of the WATCHMAN Collaboration for welcoming me as a partner and sharing with me their deep and varied knowledge in the many physics and engineering fields that underpin antineutrino detector development. In particular, I thank Dr. Morgan Askins and Dr. Felicia Sutanto for their patient guidance in teaching me to use the WATCHMAN Rat-Pac software. I also thank Professor Matthew Malek, Dr. Sam Fargher, and Rob Foster of the University of Sheffield for their contributions to the ^{16}N and ^{17}N calibration source development research. I thank Alex Kavner for his assistance with the electronics and detectors for the ^{17}N experiments. I would like to thank Professor John Mattingly of North Carolina State University and Jesson Hutchinson of Los Alamos National Laboratory for their assistance in organizing and executing the experimental campaigns at the DAF.

I thank Dr. Jason Nattress. You have been a great friend and mentor to me since I

first set foot on the University of Michigan campus. From coding sessions in the Cooley basement to discussions about the future while cruising around Nevada on our way to the DAF, I thank you for setting such a good example for me to follow.

I thank my family and friends who have supported and encouraged me throughout this journey. Most importantly, I thank my wife, Blake Lee Ogren. You have accompanied me every step of the way, through the highs and the lows, and your confidence, love, and support have meant everything to me.

Finally, I would like to acknowledge the organizations and funding sources that made this research possible. This research was supported by the U.S. Department of Homeland Security under Grant Award No. 2014-DN-077-ARI078-02 and 2015-DN-077-ARI096, and by the Consortium for Verification Technology and Consortium for Monitoring, Verification and Technology under U.S. Department of Energy National Nuclear Security Administration award numbers DE-NA0002534 and DE-NA0003920, respectively. Antineutrino-related research was performed under the appointment of the Consortium for Monitoring, Verification and Technology Doctoral Fellowship in Applied Antineutrino Physics.

Contents

List of Figures

List of Tables

List of Abbreviations

ABS acrylonitrile butadiene styrene.

DAF Device Assembly Facility.

DPP PSD Digital-Pulse-Processing Pulse-Shape Discrimination.

DU depleted uranium.

HEU highly enriched uranium.

IBD inverse beta decay.

NNSS Nevada National Security Site.

PSD pulse-shape discrimination.

PSP pulse-shape parameter.

PVT polyvinyl toluene.

SK Super-Kamiokande.

SNM special nuclear material.

SNO Sudbury Neutrino Observatory.

TOF time-of-flight.

Abstract

Fast neutrons are closely linked to nuclear fission, making them important in many nonproliferation applications, both as a measurable signal and as a source of probing radiation. This work examines a number of novel applications of fast neutrons in both the signal and source domains.

Fast neutrons are particularly attractive as an active interrogation probe due to their high penetrability and high cross-section for induced fission in special nuclear material (SNM). Because of this propensity to induce fission, radiographic imaging techniques based on fast neutron transmission can be used to combine geometric verification with detection of fissionable material. A simple experimental method is demonstrated for realizing crude imaging of the geometric configuration of special nuclear material and confirming its fissionable content based on spectroscopic fast neutron transmission measurements, which may be attractive in treaty verification scenarios where more complex or high-precision measurements are undesirable.

In addition to source transmission and the prompt fission signal, delayed neutron emission is a significant aspect of the overall fast neutron signature induced by neutron active interrogation of SNM. Delayed neutrons have unique isotope-specific spectral and temporal characteristics, which can provide the basis for isotope identification. Previous work has shown that measurement of the buildup and decay time profiles of long-lived delayed neutron groups can be used to perform isotopic discrimination in uranium and infer enrichment. However, in bulk materials with an appreciable fissile content (*e.g.*,

^{235}U), delayed neutrons have a high probability of inducing additional fission events, leading to the emission of prompt fission radiation during the delayed neutron time window. Two methods are presented for exploiting the composite nature of this signal to perform isotopic discrimination in uranium based on measurement of the delayed neutron energy spectrum and detection of coincident radiation from delayed-neutron-induced fission. Furthermore, because the long-lived delayed neutron precursors exhibit decay times on the order of tens of seconds, their time profiles are insensitive to the delay associated with scattering or diffusion in shielding, which occur on much shorter time scales. A study of the effects of neutron-moderating shielding on measurements of the delayed neutron time-emission profile is presented.

Fast neutron sources are also useful for inducing activation or transmutation reactions that cannot be produced with lower-energy neutrons or other source particles. One application of this transmutation capability is in the production of certain radionuclides that may be useful for the calibration of nuclear instrumentation. In particular, ^{16}N and ^{17}N are radionuclides that can be produced via (n,p) reactions in oxygen-containing targets, and are of interest for the calibration of large water-based Cherenkov detectors used for antineutrino detection. A demonstration of the production of ^{16}N and ^{17}N using a DT generator neutron source is presented, as well as the design, construction, and testing of a specialized beta-tagging detector. Beta-correlated measurements are performed to examine the feasibility of ^{17}N as a time-tagged neutron source for antineutrino detector calibration.

Chapter 1

Fast Neutrons and Their Applications

1.1 Nuclear Security and Nonproliferation

Throughout the course of history, the pace of scientific advancement has at times been staggering. The field of aerospace engineering provides one of the most astonishing examples: Neil Armstrong's "One Giant Leap For Mankind" came only 66 years after the Wright brothers' first flight at Kitty Hawk - less than a single lifetime. More recently, internet technology took less than two decades to completely revolutionize the way information is shared. Yet rapid innovation is seldom an unqualified good. New technologies may have powerful benefits, but they also raise new threats, which may take time to understand and even longer to combat effectively.

The field of nuclear physics has borne witness to the rapid development of transformative technology and the coincident emergence of potentially devastating threats. After James Chadwick's first theorization and demonstration of the existence of the neutron in 1932 [1, 2], it was only a few short years until the discovery and identification of nuclear fission in early 1939 by Hahn, Strassmann, Meitner, and Frisch [3, 4]. The discovery of a new nuclear reaction generated an intense amount of excitement and activity in physics research, and it did not take long for physicists to recognize the awesome potential of

nuclear fission, both as a source of energy and as a weapon. Less than six months later, Leo Szilard, along with fellow Hungarian physicists Edward Teller and Eugene Wigner, drafted a letter to President Roosevelt. The letter, which was signed by Albert Einstein, warned that the recent advances in nuclear technology could lead to the development of "extremely powerful bombs of a new type", that Nazi Germany was possibly working toward such a weapon, and that the U.S. would be wise to expand its uranium supply and accelerate its own research program [5]. This motivated the U.S. government to take action, which eventually progressed to full-scale development of nuclear weapons with the authorization of the Manhattan Project in January of 1942. From there, it was only a few short years until the first successful nuclear explosion at the Trinity test site in June, 1945. Less than two months later, the first atomic bombs were deployed at Hiroshima and Nagasaki, to devastating effect. Nuclear weapons may have brought World War II to a close, and in doing so ended a horrific chapter in world history, but their terrible destructive power presented an unprecedented danger. The sudden emergence of this new threat and the subsequent struggle to contain it would come to define the field of nuclear security and nonproliferation for decades to come.

If American leaders had hoped to contain the threat of nuclear weapons by maintaining the U.S. monopoly on the technology, they soon received a sobering dose of reality in August 1949, when the Soviet Union conducted their first successful test of a fission bomb. The rapid advance of the Soviet effort, aided by espionage, came as a shock to the Truman administration, which had built its policy approach around the assumption that America would maintain the "atomic secret" well into the future [6]. The sudden evaporation of American nuclear hegemony sparked a reevaluation of national security policy and motivated the Truman administration's decision to pursue the development of new thermonuclear weapon technology [7]. Through the 1950s and into the early 1960s, the United States and the Soviet Union competed to build ever-larger arsenals of ever-

more-powerful nuclear bombs, resulting in a record 175 combined nuclear tests in 1962 [8]. In this tense climate, growing public concern over the fallout from nuclear weapons tests, as well as the near-disaster of the Cuban Missile Crisis, led the U.S. and the Soviet Union to sign the Limited Test Ban Treaty (LTBT), which prohibited atmospheric, underwater, and space-based nuclear testing [9]. Though it only served to slow the pace of the arms race, as underground testing was still permitted, the treaty represented the first major effort to reach a multilateral agreement aimed at curbing nuclear weapons development. For the rest of the 20^{th} century and into the 21^{st} century, the U.S. and Soviet Union (later Russia) continued to engage in bilateral agreements (e.g. SALT, START, New START) to regulate the size of their nuclear arsenals, primarily by limiting the number of warheads and delivery vehicles [10].

While U.S.-Soviet competition remained the focus, the issue of nuclear weapons continued to expand, as other nations sought the power and prestige associated with a nuclear arsenal. By the mid-1960s, the UK, France, and China had all obtained nuclear weapons, and they were later joined by Israel, India, Pakistan, and North Korea, bringing the total number of nuclear weapons states to nine [11]. To arrest the spread of nuclear weapons, broader, multilateral agreements have been negotiated. Two prominent examples include the Nonproliferation Treaty (NPT), in which non-nuclear-weapon states agree not to pursue nuclear weapons development in exchange for the right to use nuclear technology for peaceful purposes, and the Comprehensive Nuclear-Test-Ban Treaty (CTBT), which seeks to ban all nuclear explosion tests, though it has not entered into force [12].

The goals of these agreements are indeed noble, but their effectiveness depends directly on the inclusion of a dependable framework for verifying the compliance of all parties. This concept is embodied by the Russian proverb, *doveryai, no proveryai*, whose translation, "trust, but verify", became a favorite catchphrase of President Ronald Reagan in the context of U.S.-Soviet relations [13]. In the early days of U.S.-Soviet agreements,

test-ban treaties such as the LTBT could be verified by nuclear explosion monitoring using acoustic, radiochemical, and seismic detection systems [14–16]. Advances in satellite technology during the 60s and 70s improved the sensitivity and reach of nuclear explosion monitoring while also providing new photographic reconnaissance capabilities, which became the chief means for verifying weapons limitation agreements, such as those stemming from SALT I and SALT II [17–19]. Generally, verification based on such unilateral intelligence gathering methods avoids the thorny issue of inspections. While this may be an asset when the negotiation of inspection protocols would otherwise present a major roadblock, unilateral monitoring methods are not infallible. For example, Iraq carried out clandestine nuclear weapons development despite being a signatory of the NPT, and many governments and international agencies, such as the IAEA, remained ignorant of their activities and intentions until inspectors uncovered evidence of a weapons program following the Gulf War [20]. This failure prompted significant changes in nonproliferation monitoring, as the IAEA moved to place more emphasis on inspections and equip inspectors with more robust detection tools, including highly sensitive environmental sampling technology [21].

As the example of Iraq illustrates, one of the key challenges of verification is to discover potential nuclear weapons development before the explosion test stage. While verification techniques for arms control agreements remain a critical component of nuclear security, continued innovation is needed to address today's evolving threat landscape. The rise of global terrorist networks in the wake of the September 11^{th} attacks has raised concerns that such groups may try to utilize crude nuclear bombs or radiological dispersal devices for future attacks. Continuing to develop and improve detection technology in support of nuclear safeguards, such as material accountancy and smuggling prevention, is vital to ensure that special nuclear materials[1] do not fall into the wrong hands.

[1] Plutonium, or uranium enriched in the isotopes ^{233}U or ^{235}U, as defined by the 1954 Atomic Energy Act.

In the case of nations that may attempt to follow North Korea's example by clandestinely reprocessing partially-spent nuclear fuel from reactors to produce plutonium for weapons development[22], long-distance measurement techniques, such as antineutrino detection, may provide the means for monitoring nuclear reactors, which could in turn detect operational conditions associated with potential material diversion or plutonium production [23, 24].

Because of their close association with nuclear fission, neutrons are a key component of nonproliferation technology, both as a measurable signal and as a source of probing radiation. On the signal side, neutron sensors and measurement techniques are an integral part of a wide variety of nuclear security and safeguards applications, including material accountancy, emergency response, and treaty verification [25]. As an interrogation source, neutrons easily induce fission and augment characteristic radiation signatures in special nuclear material, facilitating material identification for treaty verification or smuggling prevention, and neutron-induced transmutation reactions can be used to produce a variety of useful radioisotopes for instrumentation characterization and calibration [26, 27]. Just as Chadwick's discovery of the neutron was central to the development nuclear weapons, neutron-based signals and sources have a central role to play in maintaining the present and future security of a nuclear-armed world.

1.2 Sources of Fast Neutrons

Neutrons are generally classified based on their energy. At the low end of the spectrum are thermal neutrons, which have an energy of approximately 0.025 eV. While it is possible to generate neutrons with lower energy ("cold neutrons"), complex processes are typically needed to reduce the neutron energy, which involve specialized moderator configurations and cryogenic materials [28–30]. Thermal neutrons are defined as such be-

cause they are in thermal equilibrium with the surrounding medium, and 0.025 eV is the most probable energy for a free neutron at 300 K according to the Maxwell-Boltzmann distribution [31]. At thermal energies, the cross-sections of certain types of neutron-based nuclear reactions for a particular nuclide may differ dramatically from their values at higher neutron energies. For instance, ^{3}He, ^{6}Li, and ^{10}B all have high cross-sections for thermal neutron capture, but the capture cross-section decreases markedly with increasing neutron energy. Due to their high sensitivity to thermal neutrons, such isotopes are often used in capture-based neutron detectors or incorporated as neutron-absorbers in shielding materials. Thermal neutrons are also closely associated with nuclear reactors, as most operating nuclear reactors rely on maintaining a high population of thermal neutrons to drive the fission chain reaction.

The range from about 1 eV up to a few hundreds of keV encompasses slow- and intermediate-energy neutrons. In this energy region, many atomic nuclei exhibit narrowly-spaced resonances in their neutron interaction cross-sections, which arise from the energy levels of the compound nucleus formed during a neutron-nucleus interaction [32]. Because these energy levels are characteristic of the isotope undergoing the interaction, they can be leveraged to obtain information about material composition. When a material is bombarded with slow- or intermediate-energy neutrons, the neutrons will be captured, scattered, or transmitted preferentially according to the corresponding cross-sections of the material's constituent elements. By observing the subsequent gamma-ray emissions (following neutron capture) or recording the energy of the transmitted neutrons, the resonances can be identified. These techniques are called neutron resonance capture analysis (NRCA) and neutron resonance transmission analysis (NRTA) and are used to determine material composition in a wide variety of applications, from nuclear safeguards to archaeology [33, 34].

Neutrons with energy between approximately 1 MeV and 20 MeV are classified as fast

neutrons. The primary sources of neutrons in this energy range are nuclear processes such as fission, fusion, and delayed neutron emission. Because of their close association with fission and fusion, fast neutron signals are intrinsically linked with nuclear energy and weapons technology, making them the principal energy classification of interest for nuclear security and nonproliferation applications. Fast neutrons also provide many advantages as a source of probing radiation for active interrogation, as they are highly penetrating and can readily induce nuclear reactions that become much less probable at energies below a few MeV. For example, nuclides such as ^{238}U, ^{237}Np, and ^{232}Th cannot be induced to fission by thermal neutrons, but are fissionable by fast neutrons. Apart from fission, many transmutation reactions become possible at fast neutron energies, facilitating the production of radioisotopes for detector calibration and medical applications.

At energies above about 20 MeV, neutrons are referred to as ultrafast. Whereas fast neutrons are associated with nuclear processes, ultrafast neutrons are primarily produced in particle cascades induced by cosmic-ray interactions. As a result, ultrafast neutrons are mainly of interest for space-based applications or as a component of the neutron background in certain measurements.

The focus of this dissertation is on fast neutrons, particularly in the context of nuclear security and nonproliferation applications. As such, some additional discussion of fast neutron sources is warranted. The fission process is one of the principal sources of fast neutrons, especially in relation to neutron emission by SNM. In general, the fission neutron signal is divided into two temporal components, prompt and delayed. Prompt neutrons are emitted instantaneously when the nucleus undergoing fission breaks apart. The average number and energy spectrum of the prompt neutrons emitted depends on the fissioning isotope, as well as the type and energy of the particle that induced the fission. For example, in the well-known case of thermal fission of ^{235}U, the energy spectrum peaks near 1 MeV with a high-energy tail extending up to approximately 17 MeV,

resulting in an average prompt neutron energy of approximately 2 MeV [35]. While the prompt neutron energy spectrum does change for different incident neutron energies, the effect on the average energy is generally small [36]. In contrast, the average number of prompt neutrons emitted by fission events can vary substantially for different isotopes and incident neutron energies [37].

The second component of the fission neutron signal comes from the emission of delayed neutrons by fission fragments, which is a well-known phenomenon [38–40]. The products of fission reactions include a variety of unstable nuclei, which are typically neutron-rich and undergo beta decay. A fraction of the decaying nuclei also release their energy through neutron emission. The delay between the initial fission event and these secondary emitted neutrons depends on the chain decay kinetics, which are characteristic of the fission fragments, and ranges from a few hundreds of nanoseconds to tens of seconds. The beta-delayed neutrons are commonly divided into a set of groups based primarily on similarities in their precursor half-lives [41]. The specific parameters for the groups depend on the isotope undergoing fission, as well as the type and energy of the fission-inducing particle. Each delayed neutron group also possesses a characteristic energy spectrum. While most delayed neutrons are categorized as fast neutrons, they have somewhat lower average energy than prompt fission neutrons, typically on the order of a few hundreds of keV.

Fusion reactions involving hydrogen isotopes are another well-established means of producing fast neutrons [42]. The most commonly employed reactions are deuterium-deuterium (DD) fusion and deuterium-tritium (DT) fusion. The DD reaction,

$$\mathrm{D} + \mathrm{D} \rightarrow {}^{3}\mathrm{He} + n, \tag{1.1}$$

has one branch with a Q-value of 3.3 MeV and emits a neutron with an energy of

2.45 MeV, while the DT reaction,

$$\mathrm{D} + \mathrm{T} \rightarrow {}^{4}\mathrm{He} + n, \tag{1.2}$$

has a Q-value of 17.6 MeV and emits a 14.1-MeV neutron. Using these reactions as the core neutron production mechanism, neutron generators have been developed which can produce high neutron fluxes, as continuous or pulsed beams [43, 44]. The high flux of high-energy fast neutrons produced by these generators is useful for a wide variety of applications, including activation analysis, radiography, oil-well logging, and medical therapy [45]. Fusion-based fast neutron generators are convenient for inducing fission in SNM and thus play an important role in many active interrogation applications for nuclear security and nonproliferation, which are detailed in Section 1.4.

Outside of fission and fusion processes, a wide variety of alternative methods exist for inducing fast neutron emission. High-energy photon sources can be used to induce fission in SNM, thereby producing a fast neutron signature that can be used to characterize the material [46]. While the cross-sections for photofission are lower than those of neutron-induced fission, very high photon fluxes can be achieved, and photon sources produce much lower active neutron background rates, which can be advantageous for measuring prompt neutron signatures. Intense photon sources, such as linear accelerators, can also be used to produce fast neutrons via (γ,n) reactions in target materials such as deuterium, ^{9}Be, or uranium [47]. Particle accelerators can also be used to generate fast neutrons through a process called spallation. Spallation sources produce fast neutrons by breaking apart nuclei in a heavy target material using a beam of high-energy charged particles, such as protons, with the added advantage that the resulting neutron flux can be easily controlled via the driving beam [48]. Additionally, recent advances in laser technology have led to the development of laser-driven methods for neutron generation [49].

Finally, neutrons in the fast to ultrafast energy range can be produced naturally by

cosmic-ray interactions in the environment. Ultrafast neutrons typically originate from cosmic-ray spallation interactions in the upper atmosphere, but lower-energy neutrons can be produced when neutrons or muons from the initial interaction cause secondary spallation in materials near the Earth's surface. Because the cosmic rays cannot be easily shielded, these spallation neutrons are an ever-present contributor to background radiation. For small detectors in a laboratory setting, the flux of these background neutrons is usually low enough so as not to significantly impede most measurements. However, for large-scale rare-event detectors, cosmogenic fast neutrons can be a very important source of background that must be precisely characterized to accurately model and assess detector performance [50].

1.3 Measurement of Fast Neutron Signatures

1.3.1 Fundamentals of Neutron Interactions

Discussion of the equipment and techniques used to measure fast neutron signatures first requires an understanding of the fundamentals of neutron interactions with matter. As neutral particles, neutrons are not subject to the Coulomb force that dominates charged-particle interactions. Instead, neutrons passing through a given medium interact directly with the atomic nuclei, primarily through elastic scattering collisions. In an elastic collision, the incident neutron transfers some of its energy to an atomic nucleus according to the expression

$$E_R = \frac{4A}{(1+A)^2}\left(\cos^2\theta\right) E_{\mathrm{n}}, \tag{1.3}$$

where E_R is the energy transferred to the recoil nucleus, A is the number of nucleons in the recoil nucleus, θ is the angle of recoil in the laboratory reference frame, and E_{n} is the energy of the incident neutron. The remaining energy is carried away by the scattered

neutron. The maximum energy transfer occurs in backscatter collisions, where $\cos(\theta)$ is unity, and is given by

$$E_{R\,\max} = \frac{4A}{(1+A)^2} E_{\mathrm{n}}. \tag{1.4}$$

As Eqs. (1.3) and (1.4) show, a neutron can only transfer all of its energy in a single elastic collision if the recoil nucleus is a single proton (hydrogen). For all other nuclides, the incident neutron will retain some of its initial energy after scattering.

While neutrons of all energies undergo elastic scattering, fast neutrons possess enough energy to undergo inelastic collisions as well. In an inelastic collision, part of the energy transferred from the neutron elevates the recoil nucleus to one of its excited states. The excited nucleus then promptly de-excites via gamma-ray emission. Because these gamma rays are associated with specific elements and excited states, they can be used to gain insight into atomic structure and the composition of target materials [51, 52].

Apart from scattering, neutrons can also interact via a wide range of nuclear reactions. Many of these reactions involve the absorption, or capture, of the incident neutron accompanied by the release of secondary radiation. The secondary radiation may take the form of gamma rays, charged particles (such as protons or alpha particles), or other neutrons. In the case of fission, all three radiation types are emitted. At low energies, the incident neutron adds very little energy to the system, so only reactions with a positive Q-value can take place. As described in Section 1.2, this means that slow and thermal neutrons are more readily captured by certain nuclides than others. Due to their higher energy, fast neutrons are able to trigger the same nuclear reactions in a wider variety of target materials, which may require a net input of energy (negative Q-value).

1.3.2 Neutron Detector Types and Operating Principles

The operating principles of neutron detectors depend on the energy range of the neutrons they are designed to detect. Slow neutrons possess little kinetic energy, which makes them

very difficult to detect via scattering. Instead, most slow neutron detector designs utilize the secondary radiation emitted by nuclear reactions to provide the detection signal. While radiative capture, or (n,γ), reactions are the most probable capture reaction type in most materials, they have a drawback in their detection mechanism due to the inherent difficulties involved with gamma-ray detection [53]. Reactions that emit charged-particle products, such as such as (n,p) or (n,α), are much more straightforward to detect and thus provide the basis for most slow neutron detectors. Table 1.1 provides a summary of target nuclei, reaction products, cross-sections, and Q-values for commonly used neutron-capture reactions.

Table 1.1: Summary of neutron capture reactions. Two Q-values are listed for neutron capture by ^{10}B, where the resulting ^{7}Li nucleus may be left in the ground state (2.79 MeV) or excited state (2.31 MeV). Cross-sections listed are for thermal capture.

Reaction	Cross-section (b)	Q-value (MeV)
^{3}He$(n,p)^{3}$H	5330	0.764
^{6}Li$(n,\alpha)^{3}$H	940	4.78
^{10}B$(n,\alpha)^{7}$Li	3840	2.79 or 2.31

Detectors based on the ^{3}He$(n,p)^{3}$H reaction utilize pressurized ^{3}He as the gaseous medium in a proportional counter. When a neutron is captured, the resulting proton and triton produce ionization in the gas, which is converted into an electronic pulse, signaling a detected event. Proportional counters are also a popular design for detectors based on the ^{10}B$(n,\alpha)^{7}$Li reaction, with BF_3 used as the fill gas. Similarly, conventional proportional counters can also be made into neutron detectors by coating the inner walls with a thin layer of solid boron-containing material. As with ^{3}He detectors, ionization from the heavy charged particles produced by the capture reaction (a ^{7}Li nucleus and an alpha particle, in this case) provides the detection signal. While ^{3}He offers an advantage in terms of its capture cross-section, boron-based detectors are much less expensive to

produce, partly because of the much higher isotopic abundance of ^{10}B relative to ^{3}He. Both detector designs share the advantages associated with gaseous proportional counters, which include low sensitivity to gamma-ray background and a simple, robust design, at the cost of lower neutron interaction rates, especially at higher energies. To increase their efficiency, ^{3}He and BF_3 detectors are often surrounded with neutron moderators, which increase the likelihood of capture in the detector by thermalizing incoming neutrons before they reach the active volume. Following this principle, an array of multiple BF_3 proportional counters embedded in a polyethylene moderator is used as the primary detector for the neutron measurements presented in Chapter 5.

In contrast with ^{3}He and ^{10}B, lithium cannot be used as the fill gas in a proportional counter [53]. Instead, it is usually incorporated into scintillating materials, such as glass or organic liquids [54, 55]. In these detectors, the ionization caused by the ^{6}Li$(n,\alpha)^{3}$H reaction products is collected as scintillation light to form the detection signal. While the cross-section for neutron capture by ^{6}Li is somewhat lower than the corresponding values for ^{3}He and ^{10}B, the Q-value is much higher, which can be a significant advantage for discriminating neutron captures from lower-energy events, such as gamma-ray interactions.

It should be noted that, when moderators are used to slow the incident neutrons, capture-based detection provides no information about the incident neutron energy spectrum. For unmoderated ^{3}He detectors, the energy of fast neutrons can be measured, as the signal generated by the capture event will be proportional to the sum of reaction Q-value and the incident neutron energy. However, this is not an efficient strategy for performing fast neutron spectroscopy, as the capture cross-section for ^{3}He decreases rapidly with increasing neutron energy. Instead, most fast neutron detectors rely on elastic scattering collisions as the means for detection, which provide a signal that is related to the incident neutron energy. As Eq. (1.3) illustrates, light nuclei are the most suit-

able for recoil-based neutron detection. In practice, this means that scintillators made from hydrogenous organic crystals, plastics, and liquids are the most commonly employed materials for fast neutron detection.

Unlike gaseous neutron detectors, organic scintillators are highly sensitive to both neutrons and photons. Neutrons interact via elastic collisions with protons and carbon that comprises the scintillator material; the ionization caused by the recoiling proton produces the majority of scintillation light as the detection signal. For photons, recoiling electrons, primarily from Compton scattering or pair-production interactions, produce the scintillation response. The amount of scintillation light emitted is usually described by Birks' law,

$$\frac{dL}{dx} = S\frac{\frac{dE}{dx}}{1 + kB\frac{dE}{dx}}, \tag{1.5}$$

where dL/dx is the light yield per unit path length of the recoiling particle, S is the absolute scintillation efficiency, dE/dx is the energy loss via ionization and excitation per unit path length, k is a constant related to the light quenching of the material, and B is a proportionality constant [56]. As Birks' law shows, the effects of quenching mean that the light output response varies for particles with different stopping powers (dE/dx).

For electrons, the light output response is fairly linear at energies above a few hundred keV, which gives rise to the use of *electron equivalent* units [57, 58]. The *electron equivalent* (ee) is defined as the amount of light that would be produced in a scintillator by an electron of a given energy and provides an absolute standard for scaling the detector response across different particle types. Due to their higher stopping power, recoiling protons from neutron interactions experience greater light quenching compared to electrons. While this leads to nonlinearity in the light output response, complicating measurements of the neutron energy, it also provides an important means for discriminating neutron and gamma-ray events in the detector. Specifically, protons experience greater light quenching because their higher stopping power allows them to excite the scintillating medium

to a greater density of excited states. Electrons typically induce excitation of the first singlet state of the scintillator, which results in the emission of prompt fluorescence light. In contrast, the higher stopping power of protons allows them to excite higher singlet states with greater density. The higher singlet states de-excite to the first singlet state through radiationless (vibrational) transitions, which leads to greater dissipation of the excitation energy as heat and an overall reduction in the quantity of prompt fluorescence light produced relative to the energy deposited [59]. Additionally, proton recoils excite a greater density of triplet states. The triplet states de-excite on slower time scales through inter-system crossing to the first singlet state, leading to the emission of delayed fluorescence light [60]. The combination of suppressed prompt fluorescence and greater relative contribution of delayed fluorescence means a greater proportion of the light produced by proton recoils occurs at later times relative to electron recoils, leading to a difference in the temporal shape of the pulse profile. The ability to perform pulse-shape discrimination (PSD) on this basis is a key capability for many organic scintillators, which allows neutron signatures to be more easily distinguished from gamma-ray background.

In addition to recoil- and capture-based neutron detectors, composite designs exist which seek to combine the strengths of both detector types. Through a judicious choice of detector materials and geometry, the individual detector responses to capture and recoil interactions can be isolated for the same incident neutron. This allows the high distinguishability of the capture to be leveraged alongside the energy information recorded by the recoil to provide a more refined representation of the incident neutron signature. Composite detectors designed according to this principle, which utilize scintillating ^{6}Li-glass incorporated into a matrix of hydrogenous plastic scintillator, play a central role in the experiments presented in Chapters 3 and 4.

1.3.3 Components of the Neutron Signature

The neutron signature has several characteristics, each of which can be used to obtain information about the location, amount, and type of source. The simplest quantity to measure is the overall neutron detection rate. This type of measurement can provide a straightforward indication of the presence of SNM with a high passive neutron emission rate, such as plutonium, simply by observing a neutron detection rate that is elevated above known background levels. While such passive measurements are not applicable to all types of SNM, they are relevant in many nuclear security applications, such as portal monitoring, where simple, robust, and easy-to-operate detection systems are needed. Additionally, the multiplicity of a fission neutron source can be determined by surrounding it with multiple detectors and measuring the rate of coincident neutron events. Neutron multiplicity measurements are a common assay technique used in nuclear safeguards for determining the effective plutonium mass contained in mixed samples of nuclear material, such as spent fuel [61].

While it is not an inherent characteristic of the source itself, determining the spatial position of a potential neutron source is an important aspect of many nuclear security and safeguards applications, including material accountancy, border security, and emergency response. By utilizing segmented detectors or detector arrays, the spatial distribution of neutron events in the detector can be used to determine the position of the neutron source. Single-volume neutron detectors with high directional sensitivity are also being developed [62]. Furthermore, high-resolution source localization can be performed through the use of specialized shielding masks, such as coded apertures, which create a unique detector response based on the location of the neutron source [63, 64].

The energy spectrum of a fast neutron source is often one of its most prominent identifying characteristics. As detailed previously in this chapter, energy spectroscopy for fast neutrons is usually performed based on elastic collisions in recoil-based detectors.

However, measurement of the true incident neutron energy spectrum is complicated by the nonlinear light output response to proton recoils in organic scintillators, as well as the variability of neutron energy deposition during elastic scattering. As a result, analytical methods are often required to reconstruct the neutron energy spectrum. For well-separated, discrete spectra, the *spectrum stripping* technique can be used, which involves successively subtracting the detector response for each discrete energy in descending order to identify each contribution to the spectrum [65]. More complex energy spectra, such as those emitted by fission or (α,n) sources, typically require more advanced mathematical techniques to reconstruct the neutron spectrum in a process known as *spectrum unfolding* [66]. For neutron sources that emit multiple correlated particles, the energy spectrum can also be determined using time-of-flight (TOF) measurements. Detection of the correlated particle (*e.g.* a gamma ray, for a neutron emitted by a fission source) indicates the time the neutron is emitted, and the time delay is recorded between the emission and subsequent arrival of the neutron in a detector located at a fixed standoff distance. The energy of the neutron is thus given by

$$E_{\mathrm{n}} = \frac{mv^2}{2}, \text{ for } v \lesssim 0.1c, \tag{1.6}$$

or

$$E_{\mathrm{n}} = \frac{mc^2}{\sqrt{1 - \frac{v^2}{c^2}}}, \text{ for } v \gtrsim 0.1c, \tag{1.7}$$

where m is the neutron mass, c is the speed of light, and v is the velocity of the neutron calculated based on the time taken to travel from the source to the detector.

Lastly, sources of fast neutrons often exhibit unique temporal characteristics that can be used to gain insight into the quantity and composition of the neutron-emitting material. For example, measurements of the Rossi-alpha distribution, which involve counting the number of neutron events that occur over a set period of time following an

initial event, can be used to determine the effective ^{240}Pu mass of complex plutonium-containing samples [37, 67]. Many other measurement techniques for examining the time characteristics of the neutron signature use active interrogation to produce nuclear reactions in a target material and observe the time evolution of the induced radiation signal. The next section introduces a number of commonly employed active interrogation techniques that utilize fast neutron sources and signals.

1.4 Active Interrogation

Whereas passive measurements record the signal emitted through spontaneous radioactive decay, active interrogation relies on an external source of probing radiation to induce emission from a target object. The signals induced via active interrogation are typically much more intense than passive signals and carry a time signature of the interrogating source, which allows them to be more easily distinguished from natural background. The benefits of active interrogation are particularly well-illustrated by the case of highly enriched uranium (HEU). HEU is mostly composed of ^{235}U, which has a very low spontaneous fission rate, resulting in minimal passive neutron emission. Additionally, the characteristic gamma rays emitted by ^{235}U are relatively low-energy and thus are easily attenuated by surrounding materials or the uranium metal itself. As a result, HEU is difficult to detect using passive methods alone. However, when ^{235}U is induced to fission by an external neutron or photon source, it emits many high-energy gamma rays and neutrons, which are highly penetrating and much easier to detect.

Many different particle types and energies are used to perform active interrogation, such as the fast neutron generators outlined in Section 1.2. An even greater variety of measurement methods and applications exist to extract and record useful information from the radiation signals induced by active interrogation. It is beyond the scope of this

dissertation to discuss all of them here. In the following sections, a brief overview is given for each of the active interrogation methods used in the research encompassed by this dissertation.

1.4.1 Neutron Radiography

Radiography is the oldest form of active interrogation, which began with Wilhelm Röntgen's use of recently-discovered X-rays to record an image of his wife's hand in 1895 [68]. Since then, radiographic imaging has come into wide use, especially in the field of medicine. Generally speaking, radiographic measurements are made by irradiating a target object with photons or neutrons and recording an image based on the transmission of the source particles through the target object. High-energy photons, such as X rays, are the source particle of choice for most radiography applications, including medicine, dentistry, and cargo and luggage screening. Photon-based radiography is well-suited for imaging dense or high-Z materials, which readily attenuate photons due to the strong Z-dependence of the interaction cross-section. In contrast, neutron interaction cross-sections do not exhibit a definitive functional dependence on Z; still, neutrons are generally more easily attenuated by low-Z materials due to favorable energy transfer in collisions. As a result, neutron radiography can complement photon-based methods by facilitating the imaging of lighter materials. Furthermore, because neutron sources offer a high cross-section for induced fission, they can be used to simultaneously probe for fissionable materials while performing radiographic imaging, which is of interest for border security and treaty verification applications. A more detailed discussion of the principles and applications of neutron radiography is presented in the introduction to Chapter 2.

1.4.2 Induced Fission Signatures

The ability to induce fission in SNM is one of the key aspects of fast-neutron active interrogation sources. As discussed previously, the higher intensity of induced fission signals allows for characteristic information, such as the energy spectrum or multiplicity, to be more easily measured. The range of available information is greatly expanded when the timing characteristics of the fission signature can be examined. Pulsed neutron generators offer significant advantages in this respect, as they provide the ability to observe the time evolution of the fission signal between generator pulses, as well as after the source has been turned off. While the induced prompt fission signals disappear quickly after the source is turned off, delayed signatures can persist for several seconds or even minutes. Chapters 3 and 4 provide a detailed introduction to the measurement techniques used to detect and characterize SNM based on signatures in the delayed time domain, with an emphasis on signals that arise from beta-delayed neutron emission.

1.4.3 Transmutation

Transmutation is defined as the conversion of one element or isotope into another by means of a nuclear reaction or radioactive decay. Most neutron-nuclear reactions result in a product nuclide that is different from the initial nuclide, which is often an unstable isotope that undergoes radioactive decay. This is the central concept at work in neutron activation analysis, in which the radiation emitted by the products of neutron activation is used to characterize the composition of the target material [69]. Fast neutrons are particularly useful in this regard, as their higher energy allows them to induce transmutation reactions such as (n,p) and (n,α) in a broad range of target nuclides.

The radioisotopes produced by neutron-nuclear reactions are also useful for a wide range of applications in medicine, agriculture, and scientific instrumentation. Due to the extremely high neutron fluxes they produce, nuclear reactors are the primary suppliers of

radioisotopes for industrial and medical applications, which are produced via activation or as the products of fission reactions [70]. However, fast neutron generators can also be used to produce useful radioisotopes, especially those with shorter half-lives that must be produced on-site for their intended application [71]. Chapter 5 presents the application of fast-neutron-induced transmutation in the production of radioisotope sources for antineutrino detector calibration.

1.5 Dissertation Structure

The following chapters in this dissertation may be considered as a collection of standalone manuscripts connected by a common thread of fast-neutron-based technology. While all of the experiments utilize fast neutrons as both sources and measurable signatures, the primary contribution of each chapter can be categorized as either source or signature development. Chapters 2–4 are particularly closely related, as they present the results of three successive experimental campaigns performed at the same facility. These experiments utilize fast neutrons to detect and characterize SNM by inducing fission signatures through active interrogation. While fast neutrons are used as the source of probing radiation, the focus is on the development of measurement techniques for capturing information about the induced fission signature. Taken collectively, these measurement methods provide complementary information which may prove beneficial when combined with other established active interrogation techniques in nuclear security and verification applications. In Chapter 5, the view is broadened from a focus on SNM detection to encompass a wider range of physics applications, such as rare-event detection. Here, the role of the fast neutrons is to produce radioisotopes through transmutation. A case study is presented on the production of ^{16}N and ^{17}N, which are of interest for the calibration of large antineutrino detectors.

Chapter 2

Spectroscopic Fast Neutron Radiography

Fast neutrons offer a number of favorable characteristics for radiography, especially when applied to measurements of SNM. In this chapter, a simple approach to fast neutron radiography in a treaty verification setting is presented. The goal is to utilize readily available and inexpensive detection equipment to realize crude imaging of the geometric configuration of SNM, confirm its fissionable content, and obtain information on its approximate fissile mass. Measurements were performed at the Device Assembly Facility (DAF), located at the Nevada National Security Site (NNSS), in the first of several experimental campaigns encompassed in this dissertation. In this experiment, monoenergetic neutrons from D(d,n)^{3}He and T(d,n)^{4}He reactions and a linear array of liquid scintillation detectors are used to perform spectroscopic neutron imaging of up to 13.7 kg of highly enriched uranium in a spherical geometry. Detection of material diversion is demonstrated in a simple test case, and the presence of fissionable material is confirmed based on the measurement of high-energy prompt fission neutrons, including estimating the quantity of material from the comparison of measured and predicted fission neutron emission rates. This chapter includes edited portions of the 2018 publication in *AIP Advances*, entitled "Spectroscopic fast neutron transmission imaging in a treaty verification setting" [72].

2.1 Introduction

The effectiveness of international treaties aimed at preventing nuclear weapons proliferation and promoting disarmament relies on the technological capability to monitor and confirm the compliance of all participants. With the recently-signed Joint Comprehensive Plan of Action on the Iranian nuclear program, as well as the new START treaty with Russia, there is a clear need for a robust framework of verification technology. For example, the multi-stage dismantlement process includes warhead authentication, separation of the nuclear material from non-nuclear components (such as the delivery vehicle and high explosives), and storage of the SNM cores in an appropriate container, all of which require evidence of adherence to treaty protocols. Measurement of the characteristics of SNM cores such as geometry, composition, and fissile mass can provide the necessary information to ensure compliance with such treaty regulations and general safeguards standards[26, 73, 74].

However, the design of a verification system is complicated by the fact that such measurements necessarily involve the collection of highly classified data. As such, the protection of state secrets represents a significant hurdle that must be cleared for a verification technique to be considered viable. While this problem has traditionally been addressed through engineered *information barriers*, which prevent the inspector from directly observing the classified information being measured, this approach involves a high degree of complexity and susceptibility to tampering through the use of information *trapdoors* to falsify results or leak sensitive information[73, 75]. Current information barrier systems can also be expensive to implement and reduce confidence in verification measurement results[76]. The political reality associated with such mechanisms thus presents a significant barrier to their adoption and implementation. As a result, there is considerable interest the application of *zero-knowledge protocols*, in which measurements do not record any sensitive information directly, but instead may form part of a differential

comparison against a declared standard or template[75]. Such templates usually consist of a complex radiation signatures that are used to "fingerprint" SNM components[73, 77]. For example, with the aid of a ^{252}Cf active-interrogation source, analysis of an array of induced neutron signals in the time and frequency domains has been used to successfully distinguish and identify nuclear weapons components based on reference signatures[78, 79]. In addition to more complex signature-matching techniques, template-matching methods have been proposed that involve detector arrays which are pre-loaded with geometric or other characteristic data in such a way that only the differential information between the test object and the template is ever recorded by the measurement system[75]. This paper focuses on characterizing the performance of a measurement technique that has a potential for future incorporation into such future template-matching systems.

There are a number of potential methods by which a host may attempt to deceive inspectors, including replacement, diversion, or dilution of nuclear material. By measuring the type of material, as well as its composition, fissile mass, and geometry, a verification system can detect potential anomalies such as *spoofs* (false geometries or materials designed to mimic the true SNM core) or diversion of material[73]. One measurement technique which is particularly well-suited to the detection of geometric anomalies is transmission radiography. Radiographic measurements are typically performed with high-energy photons or fast neutrons, though other types of particles, such as muons, are sometimes used[26]. Photon radiography leverages the Z-dependence of the mass attenuation coefficient to localize regions of high-Z or dense material in the transmission image. Sources that span a multitude of photon energies can be used to determine the effective Z (Z_{eff}) of the material by exploiting differences between either the photoelectric and Compton-scatter cross-sections (at lower energies) or Compton-scatter and pair-production cross-sections (at higher energies)[80, 81]. Elemental identification through photon radiography is limited by the fact that a thick mass of low-Z material

may attenuate source photons similarly to a thinner mass of high-Z material. Although accuracies to within 5–10% when determining Z_{eff} have been achieved[82], difficulties are still present in distinguishing SNM from similarly dense, high-Z materials such as lead or tungsten.

Neutron transmission radiography using fast neutrons has also been used to construct high-resolution geometric images of complex configurations of mixed materials[83]. In a process analogous to the one employed for photon radiography, the composition of the material can be reconstructed based on the neutron interaction cross-section, which varies greatly with energy for lighter elements[81]. Simple transmission radiography using fast neutrons has been used to image SNM components, and the performance of such a system in restricted-dose or high-background situations can be further improved through use of the associated-particle technique[84]. In addition to transmission radiography, many established techniques exist for neutron imaging based on passive or induced emissions[85–87]. Fast-neutron imaging using coded-aperture measurements can precisely locate neutron sources, and may be useful for verification applications such as warhead counting[85]. High-fidelity imaging of SNM samples such as plutonium mixed oxide (MOX) fuel has also been achieved through the use of emitted-neutron computed tomography in a collimated slit imaging system[86]. While the sensitivity of such high-resolution neutron imaging poses problems for information barrier development, algorithms which prevent the storage of image data may increase the viability of such systems in a verification setting[88]. Alternatively, a low-resolution fast-neutron radiograph may be attractive because significant diversions could be detected without collecting detailed geometric information. Such a radiographic image could play a part in a geometric template-based verification method, which has shown promise for application to a zero-knowledge protocol[75].

It is also desirable for verification measurements to confirm whether SNM is present and in what quantity. While SNM may be difficult to distinguish from other dense, high-

Z materials using simple transmission radiography alone, it can be readily identified from the presence of fission neutrons induced by a well-chosen interrogation source. By isolating the induced-fission neutron signal from source/background interference, the relative quantity of fissile material may also be deduced. More accurate determinations of fissile mass have been achieved by interrogating SNM with continuous or pulsed neutron beams and measuring neutron multiplicity moments[89, 90]. Imaging based on induced-fission neutrons has also been demonstrated using a pulsed DT interrogation source and time-of-flight measurements to discriminate active background[87]. While much of this prior work has demonstrated excellent radiographic and neutron-source imaging capabilities, the increase in performance often comes with added system complexity, specialization, and cost. This work presents a simplified spectroscopic neutron radiography system that is cost-effective, easily implemented, and constructed from readily-available components. Such a basic design can be used to perform crude geometric imaging, confirm the presence of fissile material, and estimate its quantity. The detection of material diversion is also demonstrated using both transmission images and the abundance of the detected neutrons attributed to nuclear fission.

2.2 Experimental Setup and Simulation

2.2.1 Experiment

Experimental data were collected in a series of measurements over a four-day period at the Device Assembly Facility (DAF), Nevada National Security Site. All measurements were made using a horizontally oriented linear detector array of eight 2×2 inch EJ309 organic liquid scintillators coupled to Hamamatsu R7724 photomultiplier tubes, located at a height of 89.5 cm from the floor, and evenly spaced over an array length of 106.5 cm. The detectors were powered by two CAEN DT-5533 high-voltage power supplies, and the

signals digitized using a CAEN DT-5730 14-bit 500 MS/s desktop waveform digitizer.

The target used for transmission radiography measurements was a spherical configuration of the Rocky Flats highly enriched uranium (HEU) shells. The shells have a bulk density of 18.664 g/cm^3 and an isotopic content listed in Table 2.1[91].

Table 2.1: Isotopic Content of Rocky Flats HEU

Uranium Isotope	Weight Percentage (1971)
^{233}U	Not Recorded
^{234}U	1.02
^{235}U	93.16
^{236}U	0.47
^{238}U	5.35

Each individually numbered shell is hemispherical in shape, and each consecutive pair of shells (1–2, 3–4, etc.) represents two nearly identical hemispheres that form one spherical shell. Two different configurations of the Rocky Flats shells were used in this experiment: a "full" configuration including shells 01–24, and a "half" configuration including only shells 13–24 (inner shells 01–12 were removed, leaving an empty core). Figure 2.1 shows a schematic representation of the shell geometry, and the exact dimensions for each shell can be found in Reference [91].

Two monoenergetic neutron sources of 2.45 MeV and 14.1 MeV neutrons produced from D(d,n)^{3}He (DD) and T(d,n)^{4}He (DT) fusion reactions were used, respectively. A Thermo Scientific model MP 320 neutron generator with interchangeable DT and DD tubes was employed with an approximate isotropic neutron yield of 10^6 and 10^8 neutrons/s for the DD and DT reactions, respectively. The operating parameters for the neutron generator using the DD tube were 95 kV and 60 µA, while in the DT tube case the operating parameters were 70 kV and 45 µA.

The detectors were tested and calibrated using a ^{252}Cf source and a ^{137}Cs source. Neutron transmission measurements were subsequently made using the DD source with the target in the "full" configuration. The laboratory setup can be seen in Figures 2.2–2.3.

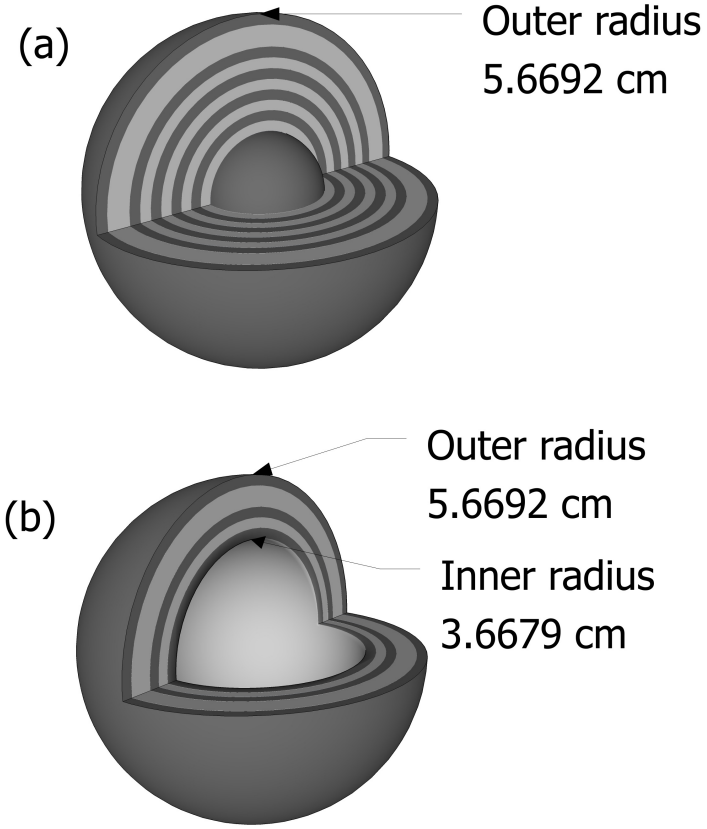

Figure 2.1: Geometric configurations of the Rocky Flats HEU shells: (a) full configuration; (b) half configuration.

The DD source and HEU target were placed on a table at a height of 77 cm, such that the height of the source and target centers aligned with the axes of the detectors to within 1 cm. The source-target distance was 30 cm from center to center, and the source-detector distance was 155.5 cm from center to center. Four transmission measurements were taken for a cumulative measurement time of approximately 3 hours, for an average measurement time of about 45 minutes. The HEU target was then replaced with a hollow tungsten sphere with an inner radius of 6.4 cm and an outer radius of 8.9 cm, and a 35–minute measurement was made to obtain transmission data for a non-fissile material. Measurements of the raw DD source (beam on, no target) and background (beam off, no

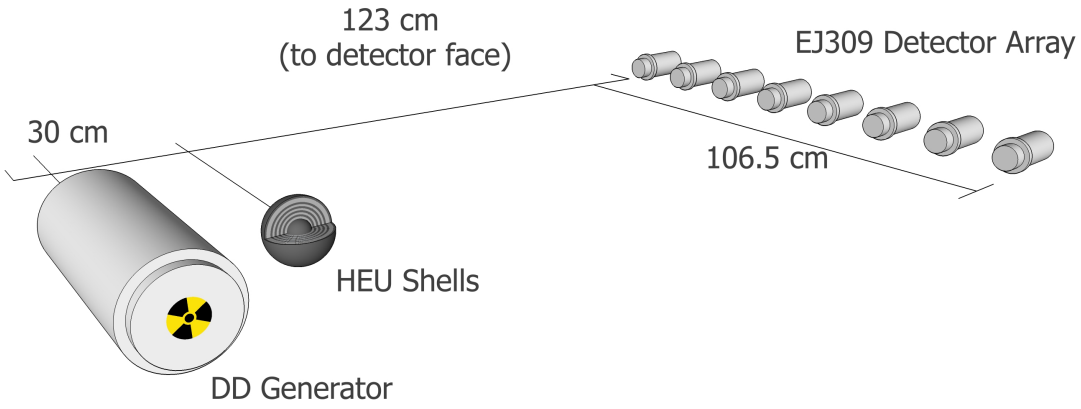

Figure 2.2: Laboratory schematic for DD transmission measurements. DT measurements used a geometrically identical setup.

target) were also recorded for about 17 minutes each.

The following measurements were made on the HEU target in the "half" configuration using both the DD and DT sources. Five DD transmission measurements of the HEU target were taken over a total measurement time of 3 hours and 20 minutes, for an average measurement time of 40 minutes. Three DT transmission measurements were then taken over a total of 21 minutes, at an average measurement time of about 7 minutes. Much shorter measurement times were used for the DT generator because the greater source strength allowed for much quicker accumulation of statistics. The dimensions of the experimental setup remained unchanged from the prior measurement in the "full" configuration.

The final set of DT transmission measurements was conducted on the "full" HEU target, as well as two shielded configurations. The first shielded configuration used a hollow polyethylene sphere with a thickness of 3.81 cm placed around the target with a gap of 2 cm between the HEU and polyethylene shield. The second shielded configuration

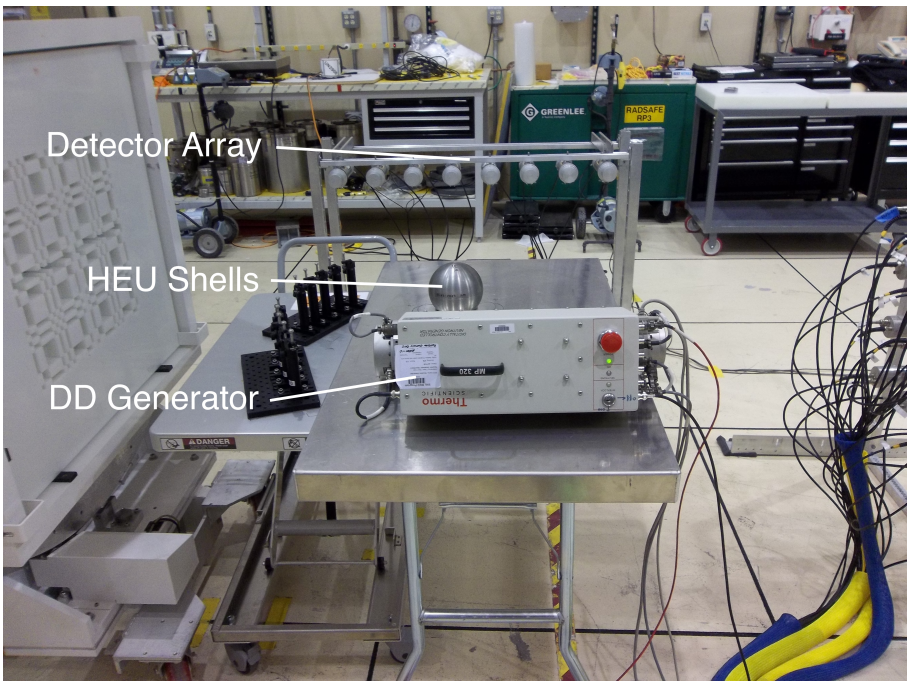

Figure 2.3: View of the laboratory setup

used a hollow tungsten shield with a thickness of 2.54 cm and a 0.7 cm gap between the shield and HEU sphere. Total measurement times were 85 minutes for the bare target, 60 minutes for the poly shield, and 15 minutes for the tungsten shield.

2.2.2 Simulation

Simulations of the laboratory measurements were made in the Geant4 framework[92] with an accurate description of the experimental geometry. The HEU target was simulated using the isotopic contents listed in Table 2.1 and the spatial dimensions for each shell[91]. For the EJ309 organic liquid scintillators, a density of 0.959 g/cm^3 and an atomic composition of 9.85% H and 90.15% C by weight were assumed[93]. Conversion of neutron interactions into light output pulses for the 2-inch detectors utilized the exponential model described in Reference [94], which was then tailored to produce light output spectra that matched experimental results. The DD and DT generators were modeled as 2.45 MeV and 14.1 MeV monoenergetic neutron sources, respectively, and projected

into a cone encompassing the full detector array. All Geant4 simulations utilized the QGSP_BERT_HP physics library, and each simulation generated a total of 100 million events.

2.3 Results

2.3.1 Calibration and PSD Performance

Detector light output was calibrated using the Compton edge for ^{137}Cs characteristic gamma rays at 478 keVee. The location of the edge was determined through comparison of simulated light output spectra with and without light output resolution broadening, with a resulting crossing point at 90% of the Compton maximum. The light output resolution function was defined using a previously described parameterization method[95].

CAEN's Digital-Pulse-Processing Pulse-Shape Discrimination (DPP PSD) Control Software was used to collect and save two preset integral regions, Q_{long} and Q_{short}, for each event. Based on differences in the light output pulse profile for neutron and photon detection events, comparison of the areas of these two integral regions provides the basis for discrimination between both particle types. The waveform integration bounds were set to [t_s, t_s+28 ns] and [t_s, t_s+160 ns] for Q_{long} and Q_{short}, respectively, where t_s is the start time of the waveform (trigger position–gate offset). The pulse-shape parameter (PSP) was calculated as

$$PSP = \left(Q_{\text{long}} - Q_{\text{short}}\right)/Q_{\text{long}}. \tag{2.1}$$

Figure 2.4 shows an example PSP distribution for a single detector during a DD neutron transmission measurement with the full HEU target in place. A threshold of 200 keVee was applied, and neutron pulses were selected by fitting a Gaussian model over the recoil

region (PSP range of 0.27–0.45). The Gaussian fits for the neutron and photon regions are also shown in Fig. 2.4, with a figure of merit of 1.50 for the two curves. The neutron region was then defined by a one-sigma cut around the centroid of the Gaussian fit for each detector channel. At high light outputs, curvature in the photon region caused it to overlap with the neutron-pulse PSP range, so an upper light output cut of 4 MeVee was also applied.

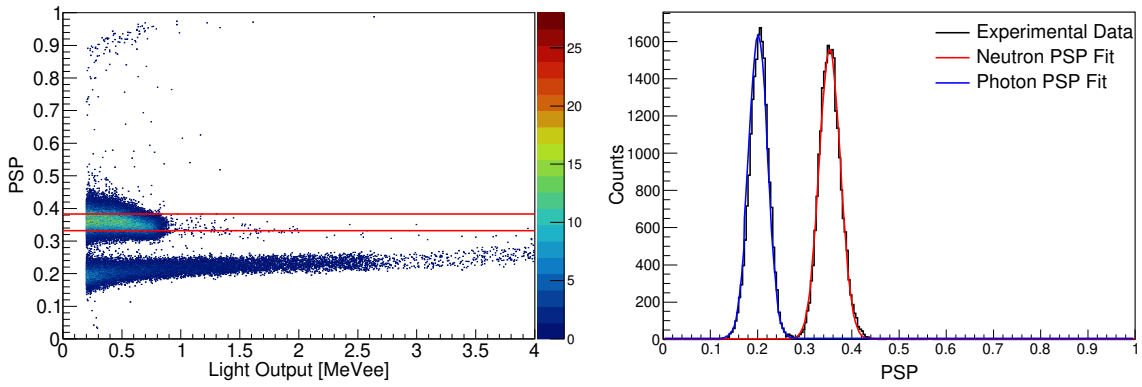

Figure 2.4: Left: Example DD measurement PSP distribution for a single detector channel. Red lines indicate the neutron cut region. Right: Gaussian model fits for neutron and photon PSP regions.

For the DT neutron measurements, significant pile-up effects in the lower light output range caused a curvature in the PSP distribution. To eliminate this skewing effect and provide a more robust definition of the neutron PSP range, a light output threshold of 4 MeVee was applied. The PSP range for each detector channel corresponding to neutron pulses was then defined using the same process used for the DD data, though the PSP range where the Gaussian fit was applied was much smaller (0.16–0.22). The resulting figure of merit was 1.60. Figure 2.5 shows the PSP distribution for the DT measurements for a single detector both before and after the application of the 4 MeVee light output threshold. Gaussian model fits for the neutron and photon regions are shown in Fig. 2.6.

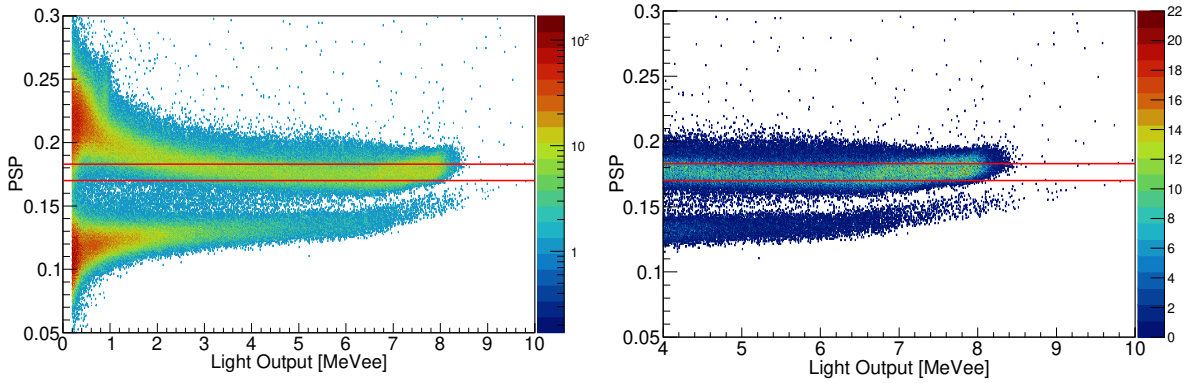

Figure 2.5: Example DT measurement PSP distribution for a single detector channel. At right is the distribution with a 4 MeVee threshold applied. Red lines indicate the neutron cut region.

2.3.2 DD Transmission

Neutron transmission data were used to construct one-dimensional image profiles for each tested target configuration. This technique could be relatively easily incorporated into a template-matching system to protect sensitive information, as a comparison of the measured transmission profile to a pre-loaded template for a particular target would allow a differential determination to be made without revealing the geometric characteristics of the target. Figure 2.7 shows the DD neutron transmission images for the full and half target configurations, representing a hypothetical differential measurement. Each channel corresponds to a single detector in the array, forming an eight-pixel one-dimensional transmission profile of the target object based on the total neutron count rate seen by each detector. Even for such crude resolution, the two scenarios are clearly distinguishable, and the diversion of material is apparent.

Validation of the experimental results and further explorations of potential measurement system capabilities were conducted by Geant4 simulation. To begin, reconstruction of the laboratory conditions in simulation was beset by a number of uncertainties, including an unknown neutron flux from the DD source and the magnitude and spectrum of

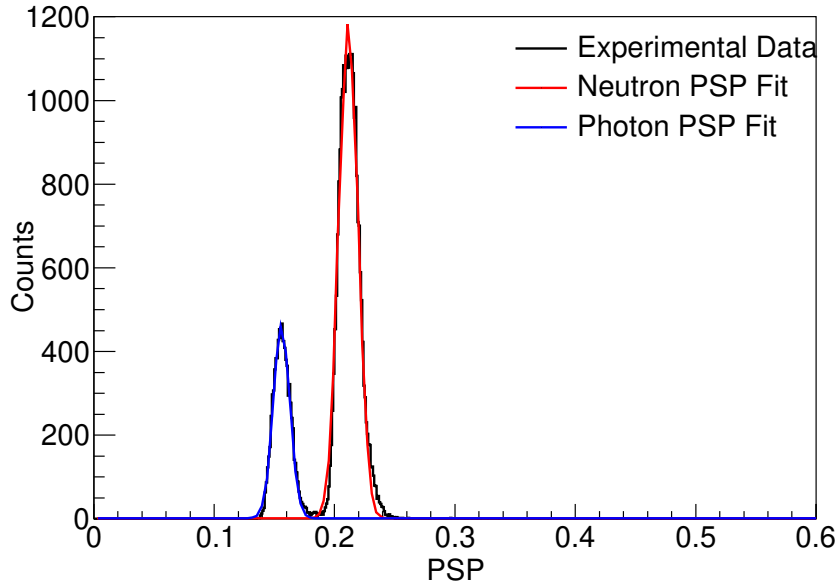

Figure 2.6: Gaussian model fits for neutron and photon PSP regions using the DT source and a 4 MeVee light output threshold.

the room-return neutrons. Based on experimental measurements of the raw DD source and initial simulations of absolute detector efficiency at each channel position, the source neutron flux was estimated to approximately 10^6 neutrons/s. However, using this flux as the basis for simulation, the simulated and experimental data still exhibit a significant disagreement.

Since the room geometry is complex and the information is lacking to model it accurately, an alternative method is needed to account for the effect of room return neutrons on the measurements. It is hypothesized that raising the light output threshold would have a disproportionate effect in discriminating lower-energy scattered neutrons, and thus greatly suppress the room-return contribution to the measured spectra. Figure 2.8 shows a comparison of experimental and simulated results for increasing light output threshold increments of 100 keVee from the initial threshold of 200 keVee up to 600 keVee, which was the upper bound for the light output cut before measurement and simulation

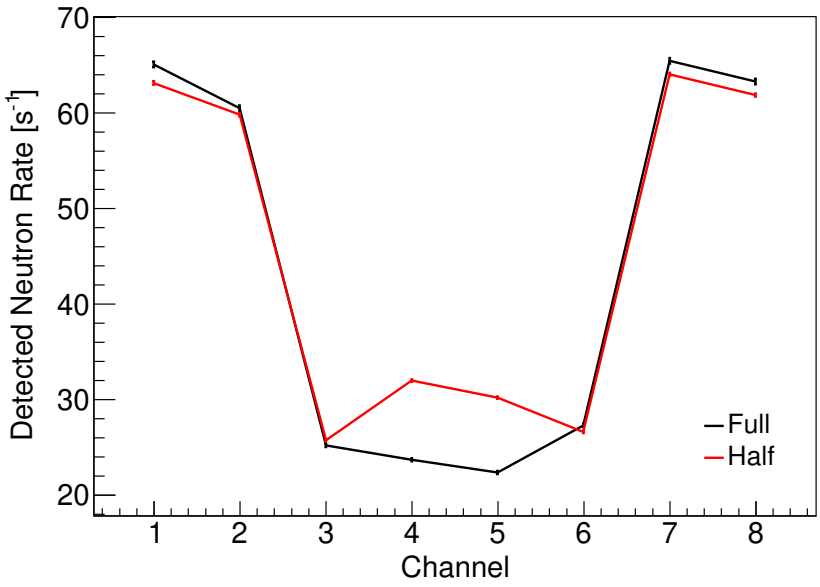

Figure 2.7: Experimental DD neutron transmission images for full and half HEU target configurations. Statistical error bars are included in the plot, but are too small to be easily visible.

statistics start to significantly deteriorate.

The increased light output cuts demonstrate effective suppression of the room return, but not all of the room return is rejected by this method. A significant amount of high-Z material is present in the experimental environment, and even for abundant lower- and mid-Z concrete constituents such as silicon or oxygen, elastically scattered neutrons can still retain a large fraction of their initial energy. Furthermore, there is some spread in the energy of the neutrons emitted by the generator. For neutrons emitted at an angle of $\pi/2$ from the direction of the generator ion beam, which was the configuration used for this experiment, the energy spread is small and the neutron energy is near 2.45 MeV, but neutrons emitted in the same direction as the ion beam can vary in energy from about 2.7 MeV to as much as 3.1 MeV[96]. As a result, the energy range of room-return neutrons extends above the full energy of the primary transmission DD neutrons, making it impossible to discriminate room return entirely using light output cuts alone.

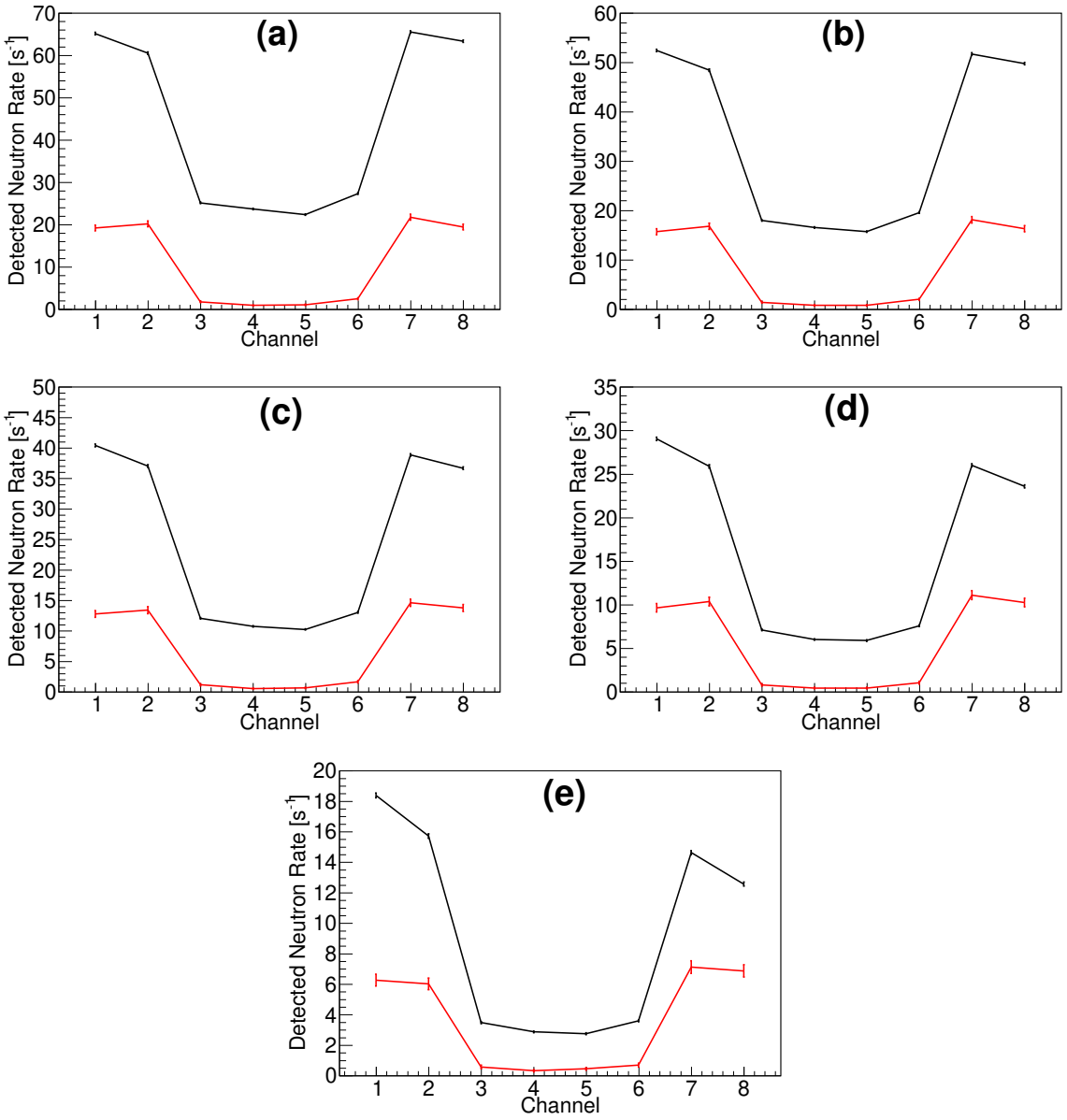

Figure 2.8: DD transmission images, experiment (black) vs simulation (red). Light output cuts: (a) 200 keVee; (b) 300 keVee; (c) 400 keVee; (d) 500 keVee; (e) 600 keVee. Progressively increasing light output cuts show an increased suppression of room-return contribution.

In addition to their effects on the detector array, scattered neutrons from the DD source can also return to the HEU object to cause additional fission events. This would lead to a higher fission rate than predicted from fast fission alone, and may account for

a large part of the initial discrepancy between simulated and experimental data. To validate this idea, the effect of a uniform, randomly-directed scattered neutron flux over the HEU sphere was simulated in Geant4, which resulted in a nearly uniform increase in the observed neutron count rate across the detector array.

It is also apparent from the comparison of simulated and experimental data that an additive correction for room return and an increased fission rate does not fully account for the discrepancy, as the two data sets are not separated by a near-constant offset. Therefore, the original estimation of DD source neutron flux, which has a scaling effect on the count rate, also needs to be adjusted. Notably, the discrepancy between simulation and experiment at higher light output thresholds was not fully accounted for by a constant scaling factor either, meaning that the differences were most likely due to some combination of the uncertainty in the knowledge of the DD generator flux and the magnitude of additive effects from room return and fission from scattered neutrons. To account for these effects, the simulated neutron transmission rate, N_{trans}, was adjusted according to two correction parameters. The first is a source strength scaling factor, S, which is intended to provide a more accurate estimate of the overall DD generator flux, and an additive factor, R, which accounts for the effects of room return and fission from the scattered neutron flux. The model for the detected neutron count rate is thus given by:

$$N_{\text{total}} = S\left(N_{\text{trans}} + R\right). \tag{2.2}$$

The correction in Eq. (2.2) shows a linear relationship between the total additive effects and the intensity of the source. This is expected since the contributions of neutron multiplication within the target and scattering in the room should scale linearly with the source intensity. The cosmic neutron background was measured to be negligible, so it is ignored by the model. Notably, in the presence of a significant cosmic neutron

background, the model would need to be adjusted to account for an additional background that would not exhibit a linear relationship to source intensity.

Once determined, the model was then optimized for the combination of S and R that led to the best least-squares fit to the experimental data. From the optimized neutron flux scaling factor, the DD generator flux was estimated to be 1.5×10^6 neutrons/s. A separate validation measurement was later performed at the University of Michigan, in which the neutron count rate was recorded using the same model of DD generator and the same size and type of detector used in the DAF experiment. The EJ309 detector efficiencies were calculated based on Geant4 models, resulting in an intrinsic neutron detection efficiency of about 30% for neutrons in the energy range produced by the generator. Based on this detection efficiency, the total neutron flux produced by the DD generator during the validation measurement was estimated to be 1.6×10^6 n/s, which is in keeping with estimates from the DAF laboratory setting. For the estimated DD generator flux, the additive factor was determined to be about 2.4 neutron counts per second. Based on Geant4 simulation, the scattered neutron flux entering the HEU object would need to be about 2–3 orders of magnitude lower than the DD generator flux in order to achieve this count rate from fission events induced by scattered neutrons. Further simulations were carried out to determine whether this magnitude of scattered flux was consistent with the DAF laboratory setting. Using the approximate geometry for significant laboratory objects such as the aluminum table and concrete floor, the total scattered neutron flux through the HEU sphere was determined to be approximately 0.3% of the total DD source flux. Therefore, the predicted flux from scattered neutrons is sufficient to cause an appreciable effect on the overall count rate, providing further physical justification for the additive factor in the mathematical adjustment model.

Figures 2.9–2.11 show the comparison of simulated and experimental data at a 600 keVee light output threshold after application of the corrected neutron flux estimate and additive

factors. After correction, the simulations are in good agreement with the experimental results, with Pearson correlation coefficients (PCC) of 0.963 and 0.956 for the "full" and "half" configurations, respectively. There is still a significant disagreement between the simulated and experimental results in the outer detector channels, which is likely due to uneven room-return contributions from large objects at either side of the array, which cannot be well approximated by a constant additive term. For example, there was a large coded aperture sheet of high-density polyethylene located to one side of the experimental setup, which may be partly responsible for the higher count rates in channels 1 and 2. However, as Figure 2.3 shows, there are other objects (*e.g.*, metal tables) that may also contribute significantly to scattering. When considering a region of interest that excludes the outermost channels in the detector array to focus on the area where the target object's shape is defined, the PCC improves to 0.997 for the "full" configuration, and 0.991 for "half".

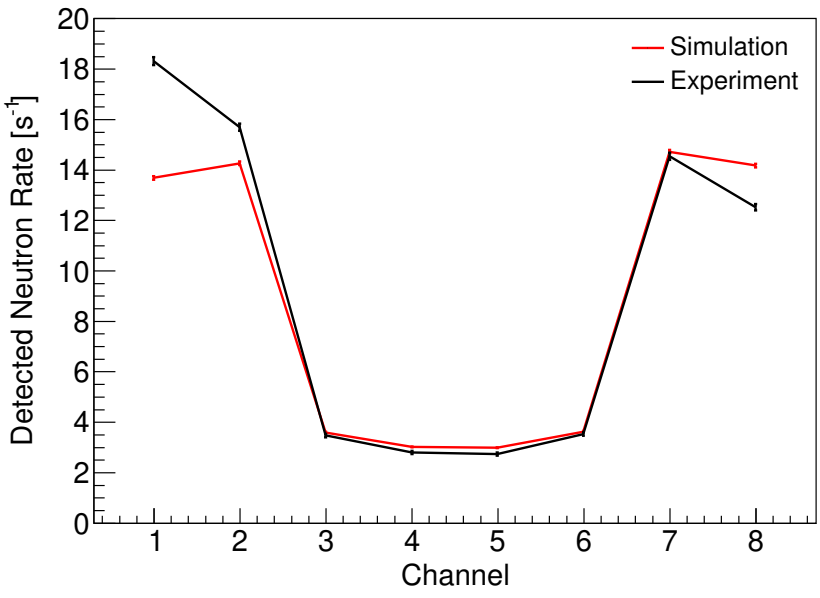

Figure 2.9: Experimental and simulated DD neutron transmission images for the HEU target in "full" configuration.

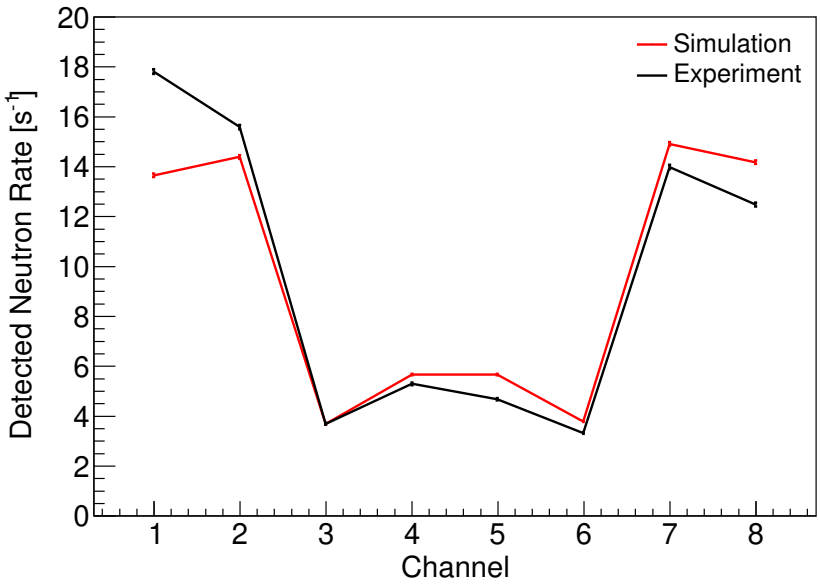

Figure 2.10: Experimental and simulated DD neutron transmission images for half HEU target.

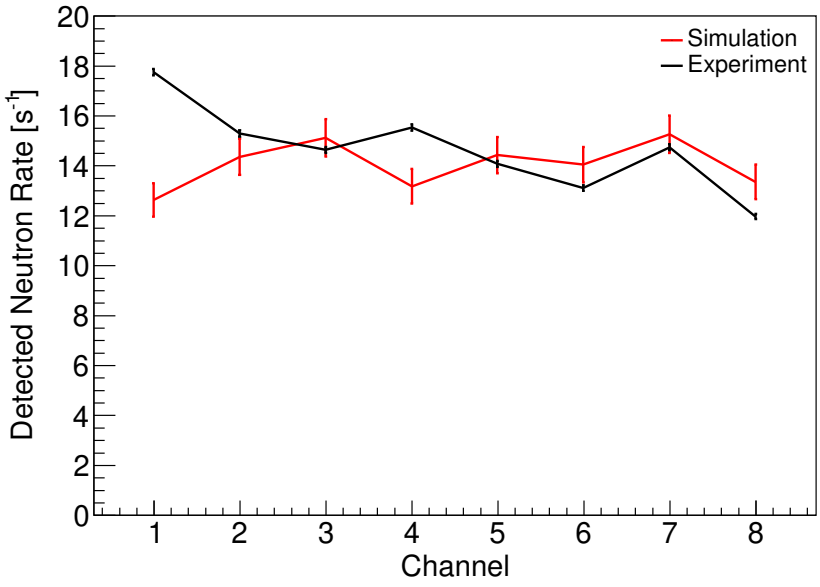

Figure 2.11: Experimental and simulated DD neutron transmission images for the DD source only (no object in place).

Having established that the transmission imaging system can detect a relatively large diversion of material, it is of interest to determine what spatial resolution may be achieved. To this end, neutron transmission was simulated for each incremental shell configuration between the full and half configurations. Figure 2.12 shows the simulated transmission results for each two-shell increment (corresponding to one spherical layer) for a measurement time of approximately 70 minutes.

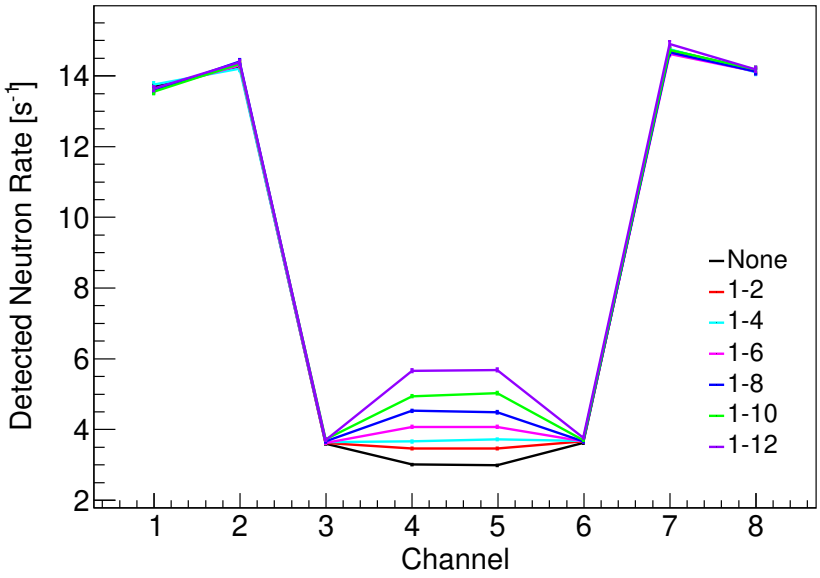

Figure 2.12: Calculated DD neutron transmission images for incremental shell configurations. The legend indicates the shell numbers that have been removed from the full configuration of shells (1–24).

Each incremental configuration, corresponding to an average inner-radius difference of 0.3–0.4 cm, is individually distinguishable within statistical error bounds. Finer resolution is likely achievable with longer measurement times, with the limiting factor being the total time allotted for measurement in a particular verification scenario. Another limit on resolution comes from the geometry of the target. For smaller amounts of diverted material, the size of the empty inner cavity is small relative to the spacing of detectors in the array. Since the two central detectors are not placed exactly along the central axis of the

target, the change in interceding material for small-cavity configurations (*e.g.*, between the 1–2 and 1–4 configurations in Figure 2.12) is less pronounced than it would be for a more centrally located detector. While it is obvious that a detector array with more pixels would provide a more detailed transmission image, this suggests that a greater number of centrally located pixels would also provide better discrimination of shell configurations, especially when the amount of removed material is small.

2.3.3 DT Transmission

Figure 2.13 shows the corresponding DT neutron transmission images for the full and half shell configurations with a light output threshold of 4.0 MeVee. The two scenarios are clearly distinguishable, with an even greater separation compared to the DD source measurements.

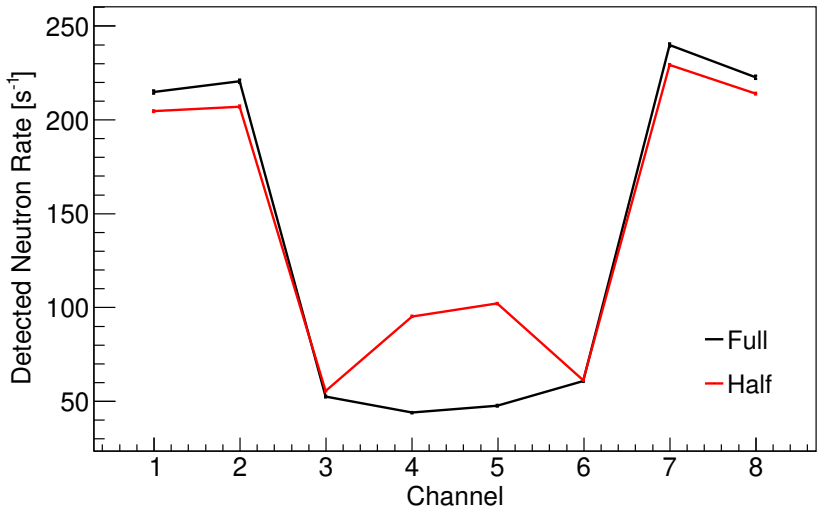

Figure 2.13: Experimental DT neutron transmission images for full and half HEU target configurations.

Experimental results were once again validated with simulation in Geant4. Simulated results for the DT neutron measurements were scaled using the same modeling and op-

timization techniques applied to the DD data. For the Thermo Scientific MP-320 DT generator used in this experiment, the expected neutron yield for operational settings of 70 kV and 50 µA is approximately 5–7 $\times 10^7$ neutrons/s[97]. This agrees well with the source neutron flux of 5.0×10^7 neutrons/s estimated by the simulation scaling model. Figures 2.14–2.15 show the comparison of simulated and experimental data for the "full" and "half" shell configurations, respectively. Once again, the simulated transmission images agree well with the experimental measurements, with PCC values of 0.999 and 0.997 for the "full" and "half" configurations.

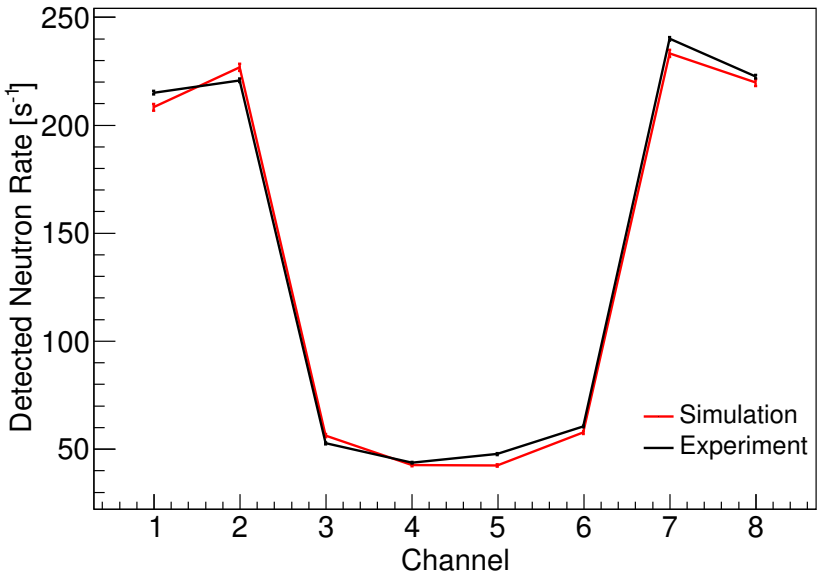

Figure 2.14: Experimental vs simulated DT neutron transmission images for full HEU target.

As with the DD source, the spatial resolution capabilities of the DT-based system were explored in simulation. Figure 2.16 shows the resulting neutron transmission images for each incremental shell configuration.

The transmission images appear to show even greater stratification compared to the DD data, and the 0.3–0.4 cm shell increments are once again well-resolved from each

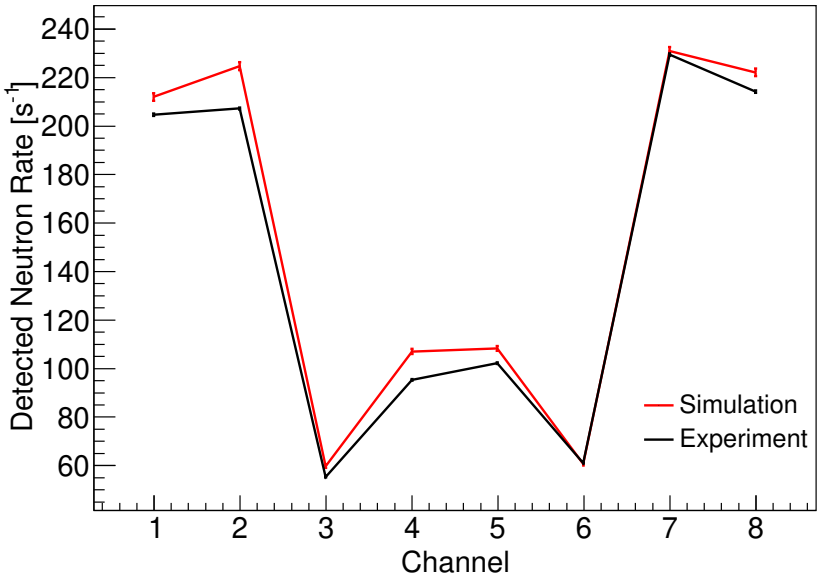

Figure 2.15: Experimental vs simulated DT neutron transmission images for half HEU target.

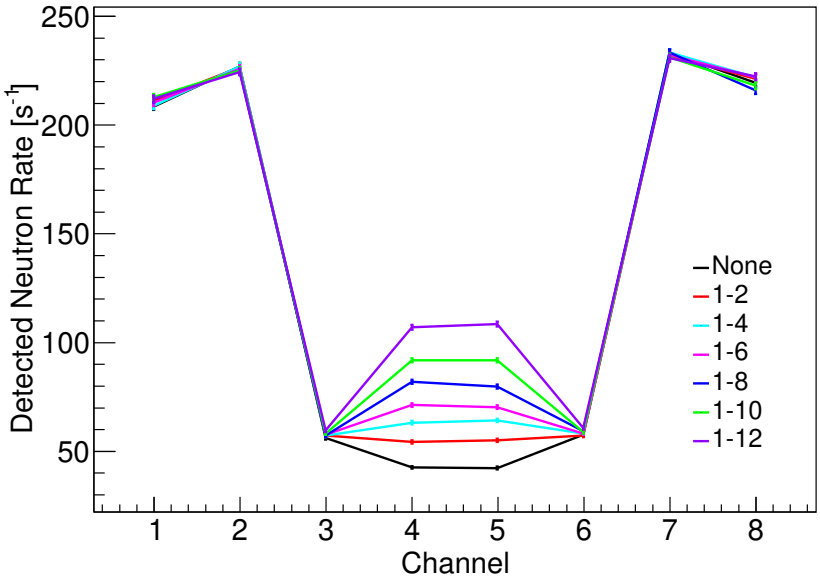

Figure 2.16: Comparison of DT neutron transmission images for incremental shell configurations. The legend indicates the shell numbers that have been removed from the full configuration (shells 1–24).

other. Due to the greater intensity of the DT source, this level of discrimination is achievable in about 80 seconds of measurement time.

The capabilities of the DT transmission imaging system were also tested under two shielding scenarios. Figure 2.17 shows the transmission image for the full HEU shell configuration with the 3.81 cm polyethylene shield in place. As a consequence of the high light output cut of 4.0 MeV, the transmission image is derived primarily from neutrons that do not lose energy by interacting in the shield. The neutron detection rate is dramatically reduced from the unshielded scenario, but any complications due to neutron moderation are eliminated by the use of a higher light output threshold. Though the difference in detected neutron rate between the detectors that are obscured by the target and those that are not is less pronounced in the overall image profile, the geometric shape of the target is still readily distinguishable, which suggests that detection of geometric anomalies would not be significantly inhibited by such a shield.

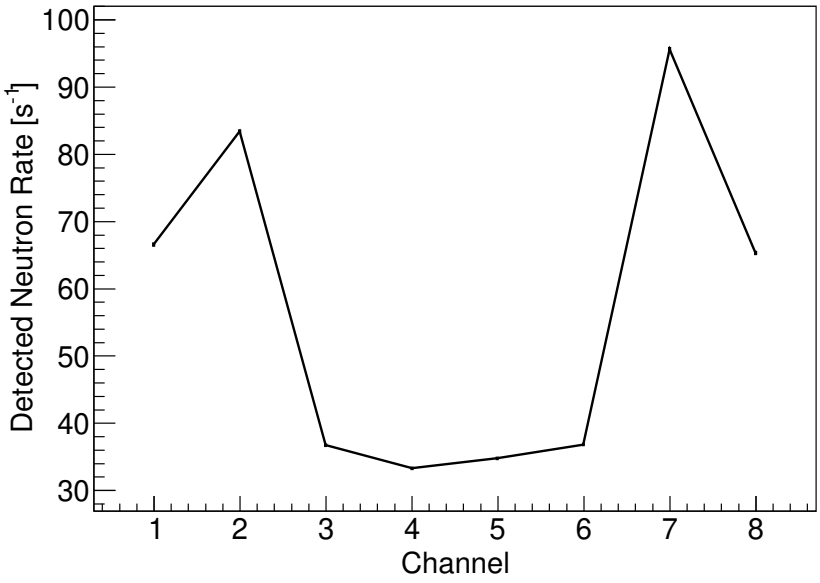

Figure 2.17: DT neutron transmission image for the full HEU sphere behind a 3.81 cm polyethylene shield.

Figure 2.18 shows the transmission image for the full HEU shell configuration surrounded by a 1-inch spherical layer of tungsten shielding. The profile is widened due to the greater radius of the target object, but there is no clear distinction between the central HEU core and the tungsten shielding. For 14.1 MeV neutrons, the total interaction cross-section of tungsten differs from that of ^{235}U by only about 6%[98]. Therefore, it is reasonable to assume that a sphere of pure HEU would generate a similar profile, which may not be distinguishable from the case where some of the HEU is replaced with a tungsten shield. Under such circumstances, additional measurements such as fission-neutron counting may be needed to differentiate the two scenarios.

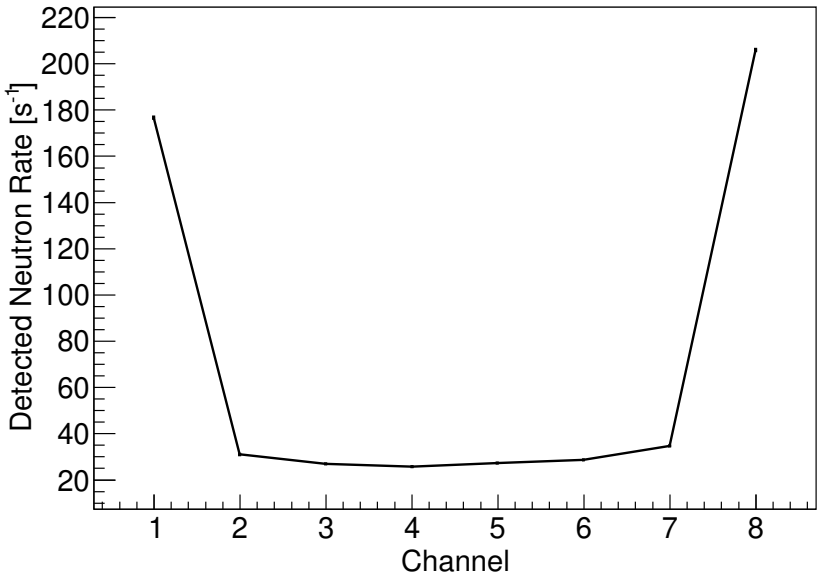

Figure 2.18: DT neutron transmission image for the full HEU sphere with a 2.54 cm tungsten outer shielding layer.

2.3.4 Fission Neutrons

While geometric transmission imaging can detect material diversion that causes a change in the core geometry, differential determination becomes much more difficult if some

or all of the SNM is replaced with a similarly dense, high-Z material. As shown in Figure 2.18, replacement of some or all of an HEU core with tungsten may still present a very similar neutron transmission profile. To guard against such cases, it is desirable that a verification system not only confirm the presence of SNM, but also provide an estimate of the quantity of fissile material. The energy spectrum for prompt neutrons from fast fission of ^{235}U is well known, and prompt neutrons with energies as high as 8–10 MeV can be observed for incident neutron energies in the range of 0–7 MeV[99]. Therefore, by imposing a lower detection threshold that is above the maximum light output for 2.45 MeV DD neutrons, only the signal from fission neutrons is measured, and the presence of SNM can be confirmed and quantified.

For the experimental data, fission-neutron thresholds were defined for each individual detector based on the measurements of the raw DD source with no target in place. The threshold was placed just above the endpoint light output for DD neutrons, providing a very conservative limit, and thus relatively high confidence that any measured neutrons originate only from fission. The measured fission-neutron rate for the "full" shell configuration (13.74 kg of HEU) was 0.733 $\pm$ 0.0082 neutrons/s, while the measured rate for the "half" configuration (10.04 kg of HEU) was 0.513 $\pm$ 0.0065 neutrons/s. A background rate of 0.18 $\pm$ 0.0135 neutrons/s above the fission-neutron threshold was also observed for the source-only data. Measurement of the tungsten sphere did not produce any appreciable fission-neutron signal above the background rate.

Figure 2.19 shows a comparison of experimental fission-neutron measurements with simulated results for each incremental shell configuration. The background rate from the source-only data has been added to all simulated results to better represent the laboratory setting. Since the count rate for high-energy fission neutrons is very low, and the probability is high that any of these neutrons would retain nearly all of their energy when scattering off the materials in the room, this measurement is very sensitive to room

return. To mitigate this sensitivity, a concrete floor was included in the simulation, using the composition for ordinary concrete (NIST) as defined in the PNNL materials compendium[100]. However, simulated transmission remained somewhat lower than the experimental data even after adjusting for background. As previously discussed, the increased rates in the experimental data are likely caused by the flux of scattered neutrons through the HEU object, which causes additional fission events beyond those caused by fast neutrons from the DD source.

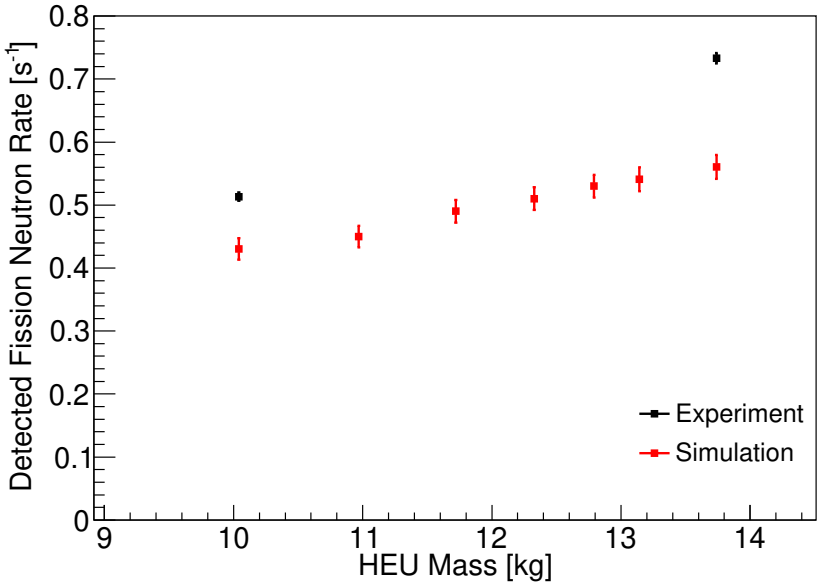

Figure 2.19: Simulated and experimental fission-neutron count rates for various HEU shell configurations.

The full and half HEU configurations both exhibit an elevated fission-neutron count rate compared to the background and tungsten measurements, confirming the presence of fissile material. The two shell configurations are also well-resolved from each other, showing that the fission-neutron rate can be used to determine the approximate fissile material quantity. The experimental results represent cumulative data collected over a total live time greater than three hours, whereas the simulated results correspond to a

measurement time of just over one hour. The trend of the simulated results in Figure 2.19 is encouraging, as the fission-neutron rate increases with HEU mass and suggests that differences of less than 1 kg are resolvable.

Though the system demonstrates the ability to discriminate two simple test cases based on fission neutron rate, it is important to note the limits of its applicability. In the presence of a significant amount of hydrogenous shielding material, high-energy fission neutrons would be moderated and thus could not be used to confirm the presence of SNM. Therefore, the current system requires some *a priori* knowledge that the test object is bare or minimally shielded. Furthermore, the single-view radiographic approach used in this experiment is limited to 2D measurements, and reconstruction of the full 3D geometry would require tomography. As a result, there could be some geometric ambiguities that may not be resolved by a 2D measurement, which could lead to inconsistencies between the inferred geometry based on radiographic measurements and the detected rate of high-energy fission neutrons.

2.4 Summary

The goal of this study has been to demonstrate the capabilities of a simple spectroscopic neutron transmission measurement system to realize crude geometric imaging of an SNM target, as well as confirm the presence of fissionable material and approximate its quantity. Using monoenergetic neutrons from DD and DT reactions, low-resolution transmission profiles were successfully constructed, from which one could readily detect the removal of the central core (3.7 kg) of a 13.7 kg HEU sphere. Simulated results suggest that even greater spatial resolution could be achieved with this system, allowing for the removal of as little as 0.5–1 kg of material to be confidently detected. Spatial resolution could likely be improved further by increasing the number of image pixels (detectors), which

would facilitate much greater distinction of relatively small diversions near the core of the target.

By applying high light-output discrimination to the transmitted neutron spectrum, the emission rate of prompt fission neutrons was successfully measured, thereby confirming the presence of SNM and giving an estimate of its relative quantity. Removal of 3.7 kg of HEU from the original 13.7 kg target was readily detected on the basis of fission-neutron rate alone, and simulated results suggest that diversions of less than 1 kg could be resolved by the system. However, the measurements of fission neutrons were inhibited by the size of the array and its distance from the HEU target, which covered a very small fraction of the emission solid angle. A custom-designed fission-neutron sensing array placed much closer to the HEU target would likely be able to provide much greater resolution in the determination of fissile mass for much shorter measurement times.

Both geometric transmission imaging and estimation of fissile mass based on prompt fission neutrons may be useful in a treaty verification setting, such as a template-matching measurement. The transmission measurement approach demonstrated here could form the basis of differential measurements of the geometric profile and prompt fission-neutron emission rate of a purported SNM sample. Further refinements of this simple approach could lead to a robust inspection tool for preventing the clandestine diversion of material during warhead dismantlement or for confirming compliance with certain nonproliferation treaty benchmarks.

Chapter 3

Prompt Neutron Signatures Induced by Delayed Neutrons

Fast neutrons are highly effective at inducing fission in SNM, making them a common choice for active interrogation applications. Fast neutrons are also emitted by the induced fission events in both the prompt and delayed time regimes, providing a signature that can be used to characterize the material. When dealing with bulk samples of SNM, secondary interactions within the material itself can lead to changes in the overall emitted signature. In materials that contain an appreciable fissile (*e.g.,* ^{235}U or ^{233}U) fraction, such as highly-enriched uranium (HEU), delayed neutrons have a high probability of inducing additional fissions. As a result, the overall delayed neutron signature consists of two distinct components: the "primary" delayed neutrons (emitted directly by fission fragments), and the "secondary prompt" fission neutrons produced in fission induced by primary delayed neutrons.

This chapter focuses on the experiments conducted in the third DAF measurement campaign, which builds upon the delayed neutron time profile measurement methods developed in the second DAF campaign detailed in the 2018 publication in *Physical Review Applied*, entitled "Discriminating Uranium Isotopes Using the Time-Emission

Profiles of Long-Lived Delayed Neutrons"[101]. In this chapter, two experimental approaches are demonstrated for discriminating between ^{235}U and ^{238}U isotopes based on the measurement of delayed neutron-induced fission products. First, HEU and depleted uranium objects are differentiated through the detection of high-energy prompt neutrons from delayed fission using both recoil-based organic liquid scintillators and thermalization spectra from a custom-built capture-gated composite detector. Secondly, coincident radiation measurements are used as the basis for discrimination by comparing the overall rates and time evolution of fission events when delayed neutrons are present. This chapter includes edited portions of the 2020 publication in *Physical Review Applied*, entitled "Discriminating Uranium Isotopes Based on Fission Signatures Induced by Delayed Neutrons"[102].

3.1 Introduction

Measurement methods that can provide detailed information on the composition of SNM are integral to many nuclear security and nonproliferation applications. In particular, determination of the relative isotopic abundance of ^{235}U and ^{238}U plays a central role in international safeguards inspections, the production and accounting of nuclear fuel, and verification of proper storage and dismantlement of weapons components under disarmament treaties [37, 103, 104]. Active interrogation sources use external radiation to induce nuclear reactions in a target material, and are commonly employed to characterize the content of SNM by inducing fission to augment both the prompt and delayed neutron and gamma-ray signatures emitted by the material [26].

When SNM is interrogated using a pulsed neutron source, the induced fission signature persists even after the source is turned off. Source neutrons become thermalized in the surrounding material, and their population decays with a characteristic time on the order

of a few microseconds [105]. When SNM is present, these thermalized neutrons can induce additional fission events, providing a secondary source of neutrons, which causes the overall population of thermalized neutrons to decay more slowly. Measurements of the neutron dieaway can thus provide an indication of the presence of fissile material, and are a well-established means for detecting and characterizing SNM [106, 107]. Unlike the common dieaway technique, this work focuses on another persistent signal: the emission and subsequent interaction of delayed neutrons in the interrogated material. By recording the sample response over a much longer timescale (tens of seconds), it is also possible to deduce additional signatures from ^{235}U and ^{238}U and gain insight into the isotopic content of the sample.

The measurement of delayed neutron signatures has long been established as an effective method for detecting fissionable materials [108]. As outlined in Chapter 1, delayed neutrons are organized into groups based on the shared characteristics of their fission-fragment precursors. The parameters that define each group differ based on the isotope undergoing fission and the incident particle that induced the fission. Because the delayed neutron groups for a particular fissionable isotope have a unique set of individual decay constants, each isotope possesses a characteristic aggregate temporal profile for delayed neutron emission, which can be used as the basis for identification. Despite the fact that delayed neutrons account for only a small fraction of the overall fission neutron yield, detection systems that utilize active interrogation to intensify the emitted delayed neutron signal have been successfully used to detect and identify fissionable materials [27, 109–113].

Previous studies have applied this principle to differentiate SNM samples by measuring the decay of the delayed neutron rate for short-lived [114] and long-lived groups [115–117]. In prior work by the University of Michigan Applied Nuclear Science Group, both the buildup and decay time profiles of long-lived delayed neutron groups were utilized to

perform isotopic discrimination and infer the enrichment level of uranium [101]. While the energy and timing characteristics of delayed neutrons have been determined by dedicated precision measurements, the observed delayed neutron signature for bulk materials can be complicated by additional interactions before the delayed neutrons escape the object. In the case of fissile materials such as ^{235}U and ^{239}Pu, delayed neutrons with an average energy of 250–450 keV can readily induce numerous additional fission events. This delayed neutron-induced fission is a basic concept in nuclear reactor kinetics, where it represents an important consideration in maintaining the desired state of criticality in a reactor. In the context of neutron energy spectrum, however, it leads to an overall delayed signal that is a superposition of two components: "primary" delayed neutrons, which are emitted directly from the decay of fission fragments, and the prompt fission neutrons, where the fission is induced by delayed neutrons. In fact, in order to measure the delayed neutron energy spectra with a high degree of accuracy, sample sizes have been restricted to small amounts (<10 g) of material with the express purpose of limiting distortions caused by fission multiplication [41, 118, 119].

Because the prompt fission products of the delayed neutron-induced fission events are emitted nearly instantaneously, they mimic the time distribution of the delayed neutrons, and do not significantly alter the measured neutron temporal profile (notwithstanding the potential differences in detector efficiency when measuring the time-evolving neutron spectrum). In contrast, the overall delayed energy spectrum is significantly changed by the introduction of prompt fission neutrons, which typically have much higher energies than delayed neutrons. Furthermore, the prompt neutrons from delayed fission are accompanied by additional coincident neutrons and gamma rays. The determining factor in the relative abundance of prompt fission products in the delayed signal is the average fission cross-section of a particular material in the delayed neutron energy range. Because this cross-section may differ significantly between isotopes, as is the case for ^{235}U

and ^{238}U, the detection of high-energy prompt neutrons and coincident radiation from fission in the delayed signature of SNM may provide the basis for isotopic identification.

In previous work it has been demonstrated that proton beams are an effective means for inducing delayed neutron signatures in SNM targets and can discriminate fissionable materials at lower dose rates than photon- or neutron-based sources [120]. The report also proposes that measurement of delayed neutrons above a certain energy threshold would indicate the presence of delayed neutron-induced fission and provide a method for discriminating uranium isotopes.

Here, two experimental methods are presented for disambiguating the genesis of delayed neutrons as a means for discriminating ^{235}U and ^{238}U. In the first approach, which leverages the method proposed in Ref. [120], recoil-based organic liquid scintillators and a custom-built capture-gated composite detector are used to perform spectroscopic measurements of delayed neutrons, and highly-enriched uranium (HEU) is successfully differentiated from depleted uranium (DU) based on the presence of high-energy prompt neutrons in its delayed signature. While the measurement of high-energy prompt neutrons from delayed neutron-induced fission has previously been proposed as a method for discriminating uranium isotopes, a review of the relevant literature suggest that this work represents the first time that such energy information has been specifically targeted and extracted from the overall delayed signature as a means for isotopic identification. The second approach demonstrates the first use of coincidence counting to observe the contribution of delayed neutron-induced fission to the overall fission rate and successfully differentiate HEU from DU on this basis.

3.2 Materials & Methods

Experimental measurements were performed at the DAF, NNSS, using HEU and DU test objects. The HEU object was constructed from the Rocky Flats shells, which are described in detail in in Chapter 2 and Ref. [91]. Shells 01–24 were assembled into a spherical object with an approximate mass of 13.8 kg. The depleted uranium object also consisted of a set of hemispherical shells arranged to form a sphere. The mass of the DU object was 12.8 kg, which was the closest approximation to the HEU object mass that could be achieved with the available shell configurations. Each uranium object was interrogated with 14.1-MeV neutrons produced by a Thermo Scientific P211 DT neutron generator, with an approximate isotropic yield of 10^8 n/s. The objects were placed at a distance of 13 cm from the generator, as measured from the center of the object to the center of the target plane in the generator tube. The DT generator was operated at a pulse rate of 100 Hz with a pulse width of approximately 10 µs, which was consistent across all measurements.

In each measurement, the uranium object was surrounded by an array of detectors, which included one 5.1-cm diameter NaI(Tl) detector, two 7.6-cm diameter Eljen EJ309 organic liquid scintillators [93], and one custom-built heterogeneous composite scintillator. The composite detector is a larger version of the prototype described in Ref. [121], and consists of an array of $1\times1\times76$ mm^3 GS20 lithium glass square rods embedded in a cylindrical matrix of scintillating polyvinyl toluene (PVT) with a height and diameter of 12.7 cm. The GS20 glass is 6.6% lithium by weight, and is enriched to approximately 95% ^{6}Li. A diagram of the composite detector design is shown in Fig. 3.1.

The principal detection mechanism for the composite detector is neutron capture by ^{6}Li, which has a reaction Q-value of 4.8 MeV and releases a triton and an alpha particle. The short range of the heavy charged particle products means that they generally deposit most of their energy in the lithium-doped glass, which possesses very different

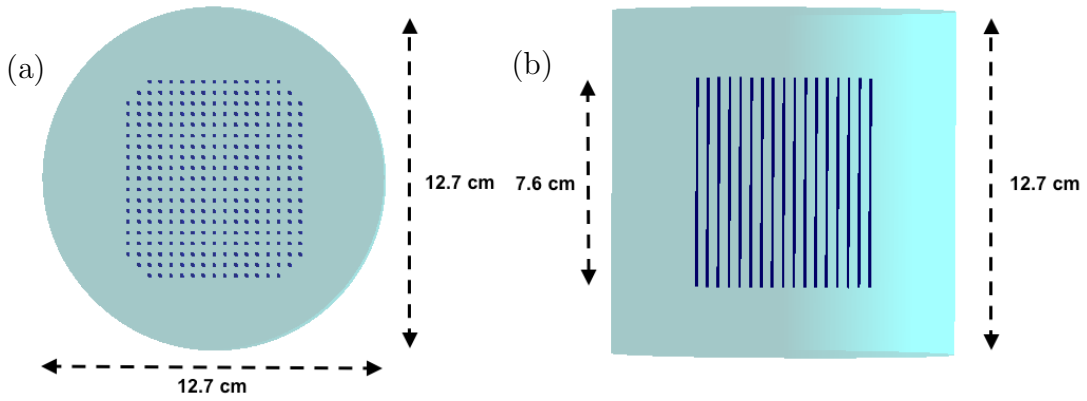

Figure 3.1: Geant4 rendering of the composite detector geometry: (a) top and (b) side view

scintillation properties from the PVT plastic. As a result, neutron capture events are easily distinguishable by both a characteristic pulse shape and the characteristic Q-value of the reaction. The PVT matrix surrounding the lithium glass rods serves a dual purpose. Not only does it increase the capture efficiency of the detector by moderating the incident neutrons, but the scintillation response of the PVT to proton recoils in the neutron thermalization process provides a signal whose magnitude is correlated to the incident neutron energy [122]. The recoil pulses from neutron thermalization are also correlated in time with the subsequent capture pulses. Though there can be significant variation in the time separation between pulses due to thermal neutron diffusion in the PVT, the average time to capture ranges from a few µs to about 10 µs, depending on the detector design and size. By exploiting this time coincidence between a capture pulse and the preceding proton recoil pulse, spectroscopic neutron energy analysis can be performed [123].

For each measurement, the composite detector was placed vertically at a distance of 21 cm from the central axis of the PVT cylinder to the center of the uranium object. The NaI(Tl) and EJ309 scintillators were placed at different locations around the object, each at a distance of 11 cm from the center of the object to the front face of the detector. Fig. 3.2 shows the experimental setup used for measurement of both uranium objects.

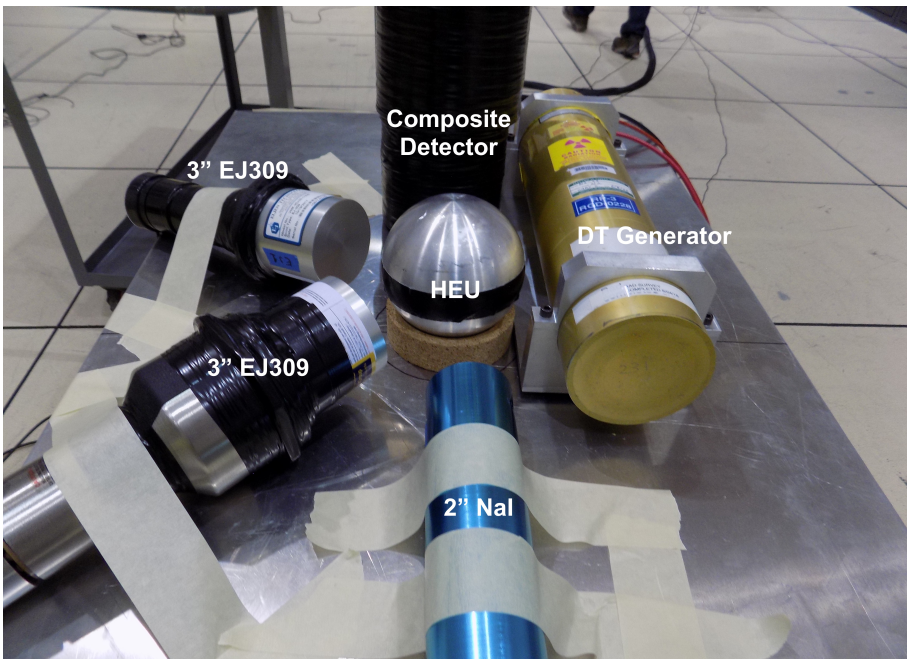

Figure 3.2: Experimental setup during measurement of the HEU object.

The detector electronics included Hamamatsu model R6527 and R6231 photomultiplier tubes (PMT), which were coupled to the composite detector (biased at 1750 V) and one of the EJ309 detectors (biased at 900 V), respectively. The other EJ309 detector was coupled to a 7.6-cm diameter Bicron PMT (biased at 1200 V), and the NaI(Tl) was a Gamma Spectacular GS-2020 integrated detector and PMT unit (biased at 750 V). Each detector was powered using a CAEN DT5533 high-voltage power supply, and the output was digitized using a CAEN DT5730 14-bit, 500-MHz desktop waveform digitizer with DPP PSD firmware. Data acquisition and storage was performed using CAEN Multi-Parameter Spectroscopy Software (CoMPASS) [124]. For each waveform, short-gate (Q_{short}) and long-gate (Q_{long}) charge integrals were recorded to provide the basis for pulse shape discrimination. The integration boundary parameters were defined relative to t_{start}, the start of the waveform determined by the leading edge trigger time in the digitizer. Q_{short} was integrated from $t_{\text{start}} - t_{\text{offset}}$ to $t_{\text{start}} + t_{\text{short}}$, and Q_{long} was integrated from $t_{\text{start}} - t_{\text{offset}}$ to $t_{\text{start}} + t_{\text{long}}$, where t_{offset} is the offset time prior to the start of the

waveform, and t_{short} and t_{long} are the endpoints for the short-gate and long-gate integration windows, respectively. The integration parameters were optimized for each detector prior to the experiment, and are presented in Table 3.1.

Table 3.1: Waveform integration parameters.

Detector	t_{offset} (ns)	t_{short} (ns)	t_{long} (ns)
Composite	24	36	376
EJ309 - 1	24	36	376
EJ309 - 2	50	50	350
NaI(Tl)	24	176	776

The neutron generator was operated in a series of on/off cycles, during which the induced delayed neutron signatures of the HEU and DU objects were recorded. In each cycle, the generator was turned on for one minute, then off for one minute. Each object was interrogated over a period of approximately 2.5 hours (approximately 70 on/off cycles), and the data collected during the generator off time was aggregated to form the overall delayed signal. Passive measurements of the HEU and DU objects were also recorded, for 3 minutes and 10 minutes, respectively. The detectors were calibrated using ^{137}Cs and AmBe sources.

3.3 Simulation

To estimate the expected contrast in the delayed neutron emission spectra from bulk samples of HEU and DU, Monte Carlo simulations were conducted. Using MCNPX-Polimi [125], spherical HEU and DU objects of the approximate size and mass of the experimentally measured assemblies were interrogated with 14.1-MeV neutrons, and the time of generation and initial energy of emitted neutrons were recorded upon their arrival in a liquid scintillation detector. The prompt and delayed neutron spectra were separated using a simple time threshold, where neutrons arriving at the detector within 10 µs of the

generation of the source particle were vetoed. The time threshold was chosen based on the simulated time distribution of prompt neutrons. A cutoff of 10 µs excludes 99.99% of the prompt neutrons, while the vast majority of delayed neutrons arrive much later than 10 µs after their parent fission event. Within the delayed neutron data, primary delayed neutrons and prompt neutrons from delayed fission were differentiated by tracking their individual histories in the MCNPX-PoliMi collision file output. Based on the particle and generation numbers of each delayed neutron, the corresponding parent fission event was located within the fission chain in the uranium object. If the time delay between the parent fission and detection of the delayed neutron was greater than 10 µs, the event was categorized as a primary delayed neutron. Otherwise, it was considered to be a prompt neutron from delayed fission. This analysis method allowed for estimation of the relative contribution of each type of delayed neutron to the overall delayed spectrum emitted by each object. For HEU, prompt neutrons from delayed fission account for about 65% of the delayed neutron signature, with the remaining 35% contributed by primary delayed neutrons. In contrast, primary delayed neutrons made up over 98% of the emitted signal for DU.

In addition to the experimental object materials, simulations of the expected relative proportion of primary delayed neutrons and prompt neutrons from delayed fission were performed for a variety of uranium enrichments to explore the potential for finer determination of the enrichment level based on the induced neutron spectrum. Fig. 3.3 shows the proportion of the overall delayed neutron signal that is expected to be contributed by secondary prompt neutrons as a function of enrichment. Table 3.2 shows a summary of the simulated neutron spectrum breakdown for selected enrichment levels.

While higher-energy prompt neutrons make up only a small fraction of the delayed neutron spectrum for DU, their proportion increases rapidly as enrichment increases from 0.2% to 20%, and they already form a significant part of the delayed signal for 5%-enriched

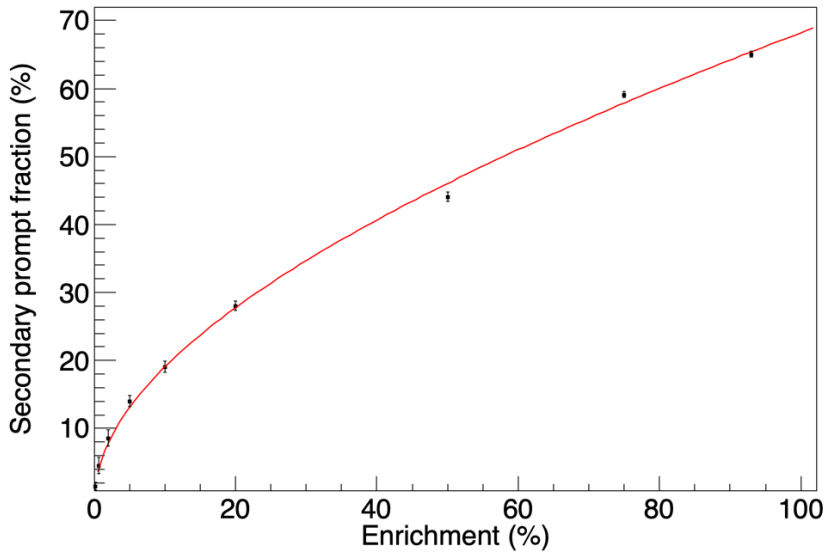

Figure 3.3: Simulated contribution of secondary prompt neutrons to the overall delayed neutron signature as a function of uranium enrichment. The red line is provided only as a guide to the eye.

Table 3.2: Simulated contribution to overall delayed neutron spectrum from primary delayed neutrons and prompt neutrons from delayed fission for selected uranium enrichments.

Material (Enrichment)	Primary Delayed	Prompt
DU (0.02%)	98.5%	1.5%
LEU (5%)	86%	14%
LEU (20%)	72%	28%
HEU (93%)	35%	65%

LEU. As a result, it may be possible to distinguish LEU from natural uranium based on the presence of higher-energy neutrons in the delayed neutron signature. Furthermore, the relative contribution from prompt neutrons doubles as enrichment increases from 5% to 20%, and more than doubles again for weapons-grade enrichment levels (>90%). Such separation suggests that the proportion of higher-energy delayed neutrons may serve as an observable for estimating the enrichment level of uranium-containing materials.

For each material, the fractional contributions of primary delayed neutrons and prompt neutrons from delayed fission were used to approximate the delayed neutron energy spec-

tra, which were then used to simulate the expected response in the composite detector using the Geant4 framework [92]. While MCNPX is better suited for simulating the production of delayed neutrons, Geant4 does not have the same geometrical limitations, making it the more convenient choice for modeling the complex structure of the composite detector. To simulate the light output response to proton recoils during thermalization in the PVT, the detector was bombarded with neutrons with energies sampled from the delayed [41] and prompt [126] energy spectra in accordance with their relative proportion for each isotope. The light output produced by neutron elastic scatters on protons in the detector was modeled using a similar method to the one described in Ref. [94], with a polynomial function of the form

$$L = aE - b\left[1 - \exp(-cE)\right], \tag{3.1}$$

where L is the light output, E is the energy deposited on the proton, and a, b, and c are fitting parameters. The light output contribution from scatters on carbon nuclei was assumed to be approximately 2% of the energy deposited. A Gaussian broadening function was parameterized and applied to the calculated light output according to the method outlined in Ref. [127]. Fig. 3.4 shows the simulated delayed neutron energy spectra for bulk HEU and DU, as well as the expected light output response of the composite detector. The light output units are MeVee (MeV electron equivalent), where 1 MeVee represents the light output generated by 1 MeV of electron energy deposition.

The simulated delayed energy spectra and corresponding detector response show very significant differences for each material based on the presence of delayed fission events, especially at higher neutron energies. This suggests that ^{235}U and ^{238}U should be readily distinguishable based on the presence of high-energy neutrons in the measured delayed signal.

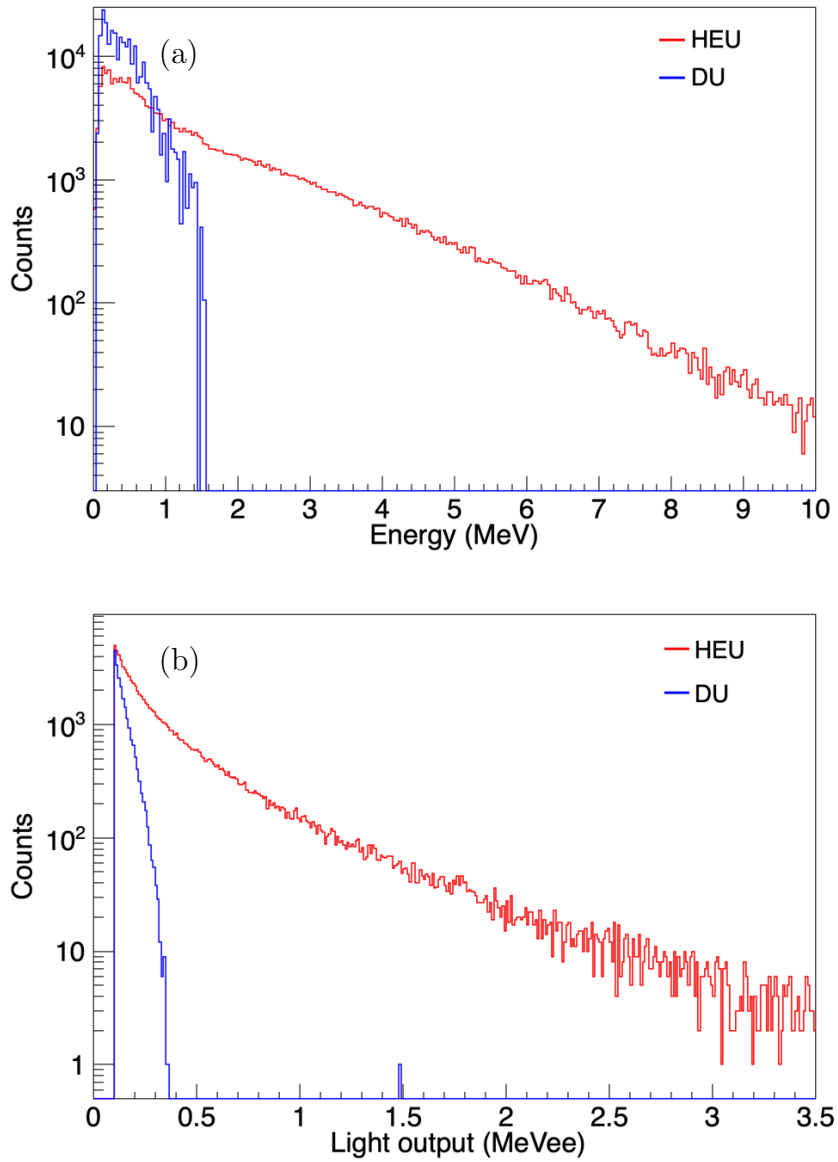

Figure 3.4: (a) Simulated delayed neutron energy spectra for bulk HEU and DU, based on proportional contribution of prompt products of delayed fission, and (b) simulated response of the composite detector to overall HEU and DU delayed energy spectra. In both cases, counting results are based on simulation of 250,000 source particles.

3.4 Experimental Results & Discussion

A significant advantage of the composite detector is that it provides strong discrimination of neutron-capture events on ^{6}Li, which can then be used to identify potential preceding thermalization events in the detector and extract spectroscopic energy information from the incident neutrons. Fig. 3.5 shows the pulse-shape parameter (PSP) and light output distribution for the AmBe calibration measurement in the composite detector, where the PSP is defined by Eq. (2.1). The parameter space located around $PSP = 0.55$ and light output of about 0.32 MeVee corresponds to neutron capture events. A 3-σ cut was established in two dimensions around this region, and any events falling within the cut were classified as neutron captures in the subsequent measurements.

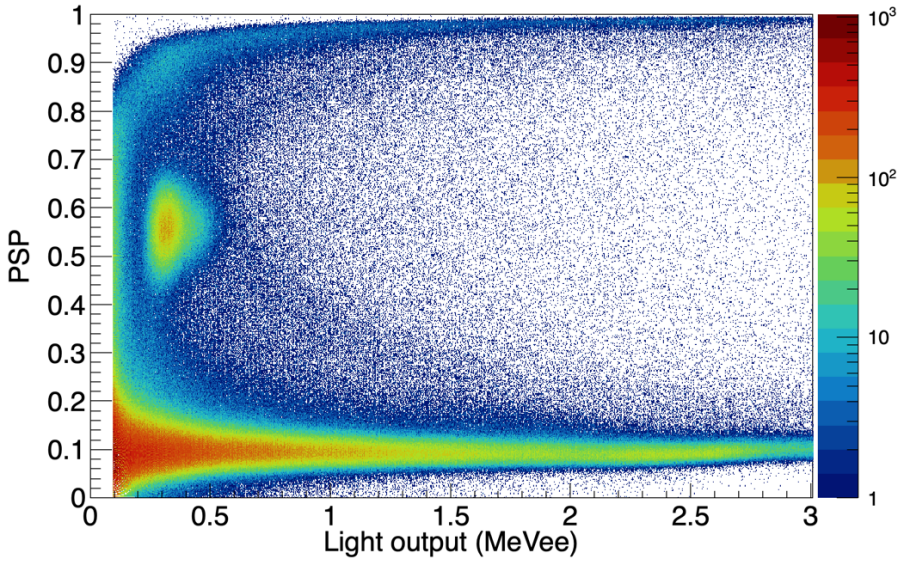

Figure 3.5: Calibration PSP and light output distribution in the composite detector when exposed to an AmBe source. Neutron captures were identified using a 3-σ cut around the island feature centered at $PSP = 0.55$ and light output of 0.32 MeVee.

3.4.1 Delayed Neutron Energy Analysis

The delayed neutron energy spectra for HEU and DU were compared by analyzing the capture-gated light output response in the composite detector. For each neutron capture event, the previously recorded pulse was examined to determine if it could have been caused by thermalization of the fast neutron in the PVT prior to capture. Because the type of PVT used in the composite detector is not PSD-capable, there is only one recoil region corresponding to both neutron and gamma-ray interactions. A Gaussian fit to this region established a mean PSP value of 0.0865, and pulses exhibiting deviation from the mean greater than 3-σ were rejected. Geant4 simulations were also used to determine the time scale of neutron thermalization in the composite detector. Both prompt and delayed incident neutron energy spectra were modeled; the results indicate that 99% of captures occur within 76 µs of the initial scattering interaction in the detector, and that incident neutron energy has little effect on the shape of the time distribution of capture-gated recoil pulses. As such, only recoil pulses that occur within 76 µs before the subsequent capture event were included in the capture-gated light output distribution. Fig. 3.6 shows the resulting capture-gated light output distributions for HEU and DU.

While some increase in the delayed neutron counting rate is expected for HEU relative to DU due to the greater mass of the HEU object and increased fission cross section for 14.1-MeV neutrons, the higher overall rate is also consistent with increased multiplication caused by delayed neutrons. However, the marked increase in high-light-output events for HEU indicates a significant difference in the overall energy spectrum, which can be explained by the presence of higher-energy prompt neutrons from delayed fission. Such differences in the shape of the neutron energy spectrum may provide the basis for discrimination between isotopes and inference of the enrichment level.

The capture-gated event rates above 400 keVee are 58.95 s^{-1} for HEU and 18.76 s^{-1} for DU. HEU and DU could be distinguished based on rate comparison, but such a

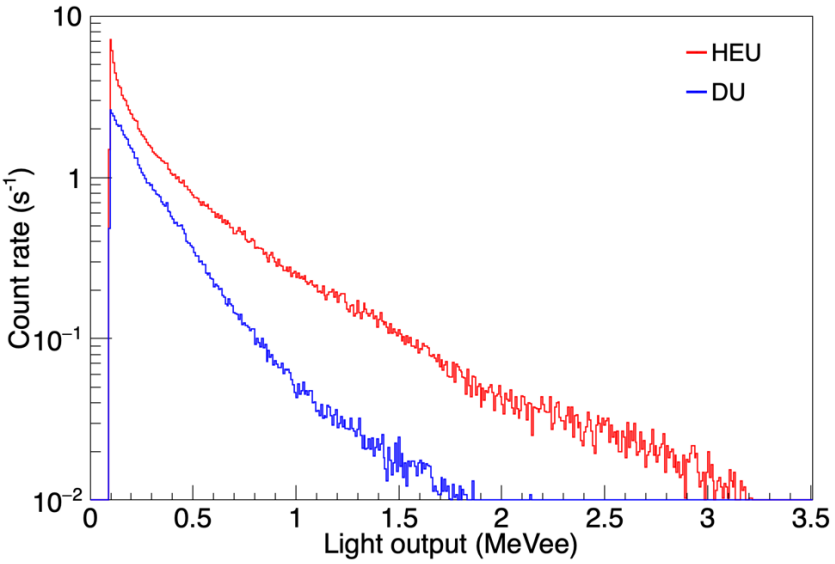

Figure 3.6: Comparison of experimentally measured capture-gated light output distributions in the composite detector for HEU and DU. Recoil events with $PSP = 0.0865 \pm 3\sigma$ and a recoil-capture coincidence time < 76 µs were accepted. The count rate for DU above 400 keVee is consistent with the measured rate of gamma-ray accidentals within the recoil-capture acceptance window.

method relies on the knowledge of sample mass. A more robust isotope discrimination method would be based on differences in the shapes of the neutron energy spectra. One possibility is to use a simple ratio of two different regions of the energy spectrum, which would provide a characteristic number associated with the proportion of prompt neutrons from delayed fission in the spectrum (and thus an indicator of enrichment). Fig. 3.7 shows a diagram of the proposed metric, which is the ratio of the integral of the high-energy tail of the neutron spectrum to the integral of the entire spectrum. This ratio is defined as R, and its standard deviation is σ. A figure of merit (FOM) for discrimination could be determined using the expression

$$\mathrm{FOM} = \frac{\overline{R}_{\mathrm{HEU}} - \overline{R}_{\mathrm{DU}}}{\sigma_{R_{\mathrm{HEU}}} + \sigma_{R_{\mathrm{DU}}}}, \tag{3.2}$$

similarly to a standard method used for evaluating pulse-shape-discrimination perfor-

mance of scintillators.

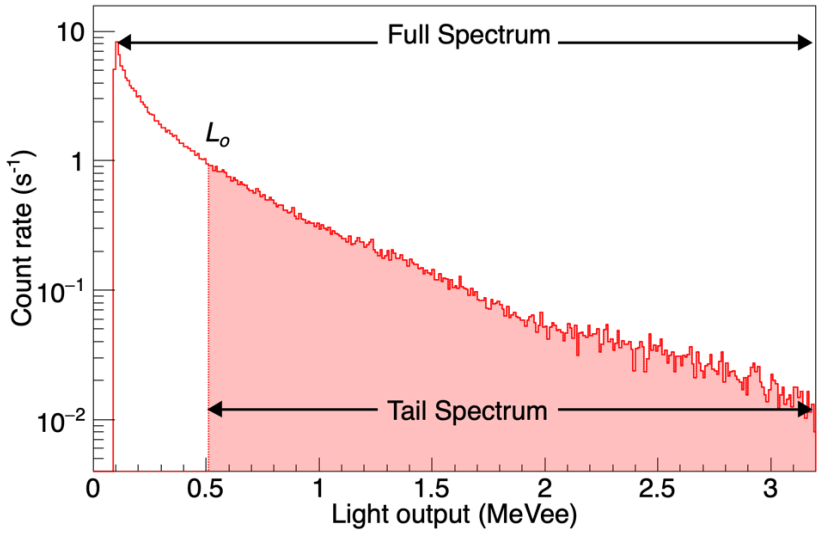

Figure 3.7: Diagram of the proposed integration regions for determining the characteristic spectral shape ratio. The example spectrum shown is for HEU.

The ratio R is determined by the choice of parameter L_o, which is the light-output threshold separating the high-energy tail from the rest of the spectrum. The threshold $L_o = 515$ keVee shown in Fig. 3.7 is the result of optimizing for the maximum separation between the ratios for HEU and DU along with the minimum statistical error. The maximum ratio separation occurs at 515 keVee, where the HEU ratio, R_{HEU}, is 0.302 and the DU ratio, R_{DU}, is 0.178. While the minimum statistical error of 1.1% occurs a higher L_o value of about 700 keVee, the error at 515 keVee is only very slightly higher at 1.24%. As such, the marginal loss in ratio separation by moving the L_o value closer to 700 keVee would be greater than the marginal improvement in statistical error.

The shape-based discrimination method appears promising when applied to the experimental data. Using the L_o value of 515 keVee, the tail-spectrum count rates were 45.8 s^{-1} and 12.2 s^{-1} for HEU and DU respectively, while the total-spectrum count rates were 151.7 s^{-1} and 68.8 s^{-1}. These experimental count rates allow for 3-σ discrimination of the HEU and DU characteristic ratios within 2 seconds of measurement time after the

neutron generator has been turned off. Total measurement time would be just over one minute, as the one minute interrogation time is necessary to build up the delayed neutron populations.

Examination of the time distribution of coincident recoil-capture pulses can provide additional insight into the observed light output spectra. While the simulated light output response for delayed neutrons from ^{238}U is largely restricted to below 400 keVee, the experimentally measured distribution extends to higher light outputs. Since the delayed neutrons do not have enough energy to produce higher light output pulses in the detector (and a large fraction cannot even produce a pulse above a 100 keVee detection threshold), this suggests either that there is a higher rate of delayed fission than predicted by tabulated nuclear data, or that the capture-gated light output distribution is dominated by gamma-ray accidentals from background or passive emission by the DU object. If accidentals dominate, then the distribution $I(t)$ of time differences between two adjacent pulses is governed by the general expression

$$I(t) = r \exp(-rt), \tag{3.3}$$

where t is the time between two pulses, and r is the rate of accidentals. In the scenario where there are very few true thermalization events, Eq. (3.3) predicts that the time distribution should exhibit a simple exponential decay shape. Fig. 3.8 shows the experimental recoil-capture coincidence time distributions for HEU and DU, which have been fitted with an exponential function representing the expected contribution of background accidentals.

In both cases, the exponential function was fitted to the time window beyond 90 µs, where the contribution of true neutron thermalization events is negligible (less than 1% of the total distribution). The model is then extended back over the range of possible neutron thermalization times. In the case of DU, the exponential function is consistent

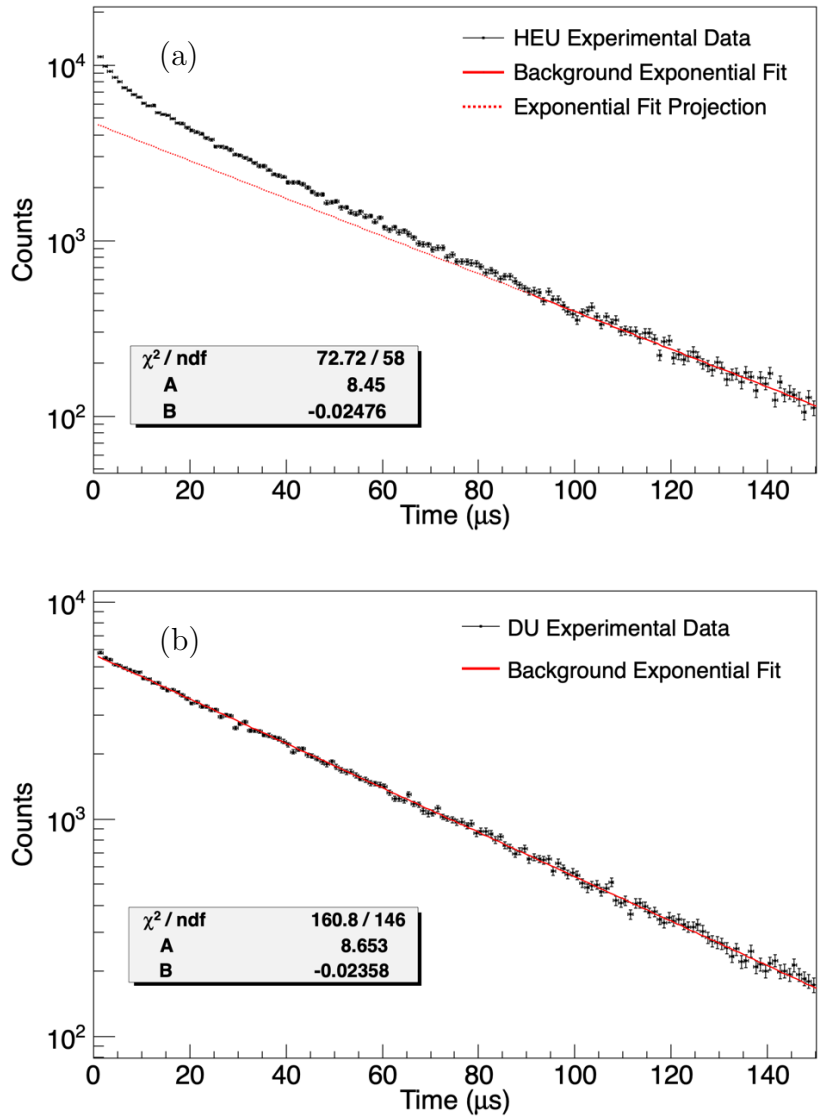

Figure 3.8: Experimental recoil-capture coincidence time distributions in the composite detector for (a) HEU and (b) DU. Each curve is fitted with an exponential function representing the expected contribution of background accidentals. For HEU, the χ^2 value applies only to the range of times beyond 90 μs. For DU, the χ^2 value applies to the full range.

with the entire distribution, suggesting that few, if any, of the pulses preceding neutron capture events are caused by thermalization of delayed neutrons. In contrast, the time distribution for HEU departs significantly from a simple exponential shape in the neutron

thermalization window, and the point where this deviation becomes noticeable is near the maximum thermalization time of 76 µs predicted by simulation. After subtracting the background exponential fit, 98.5% of capture-gated recoil pulses occur within the 76 µs time window, in close agreement with the simulated result of 99%. The significant difference in the time-to-capture curves for HEU and DU suggest that this signal may provide yet another means for performing isotopic discrimination. Furthermore, the decay constant of the exponential fit is very similar for each data set, which suggests a common cause of accidentals, such as gamma-ray background.

The overall rate of recoil pulses recorded by the composite detector between generator runs for DU is consistent with the assertion that the events in the DU capture-gated spectrum above 400 keVee are caused by gamma-ray accidentals in the thermalization window. When the generator is turned off following interrogation, the observed rate of recoil pulses is approximately 2.1×10^4 s^{-1}. At this rate, the average time between events is 48 µs, and the probability of observing a random recoil pulse within the 76 µs time window preceding a capture pulse is 79.5%. In the experimental results, 74.0% of recorded capture events are accompanied by a preceding pulse within 76 µs.

The observed rate of events within the thermalization window is close to the prediction if all thermalization candidate pulses were truly from gamma-ray accidentals, but it is still somewhat too low. This may be explained by the effects of delayed neutron contributions to the recoil PSP region and pileup pulses in the neutron capture region. Specifically, if the recoil rate contains significant contributions from delayed neutrons, the rate of events in the thermalization window will be higher than expected for random gamma-ray accidentals because neutron recoils are much more likely to be followed by a subsequent capture event. Furthermore, misclassified pileup pulses in the capture PSP region are less likely to be preceded by a neutron recoil event. This results in a situation where the random gamma-ray rate, and thus the probability of an event within the thermalization

time window, is slightly overestimated.

To correct for the effects of delayed neutron recoils on the estimation of the gamma-ray accidental rate, a 400 keVee light output threshold was applied, effectively removing neutron contributions from the spectrum. The threshold was determined based on the simulated light output response of the composite detector to delayed neutrons, as shown in Fig. 3.4. The overall rate of recoil events above the threshold was 5.6×10^3 s^{-1}, resulting in an average time between events of 177 µs and a 34.9% probability of observing a random event within the 76 µs thermalization window. In the experimental data, 33.9% of capture events were accompanied by a preceding recoil event within 76 µs, which strongly suggests that gamma-ray accidentals contribute significantly to the the rate of recoil-capture coincidence events in the DU light output spectrum (Fig. 3.6) above 400 keVee. Table 3.3 provides a summary of the recoil rates, probability of gamma-ray accidentals in the thermalization window, and comparison to experimental data, both with and without application of the 400 keVee light output threshold.

Table 3.3: Summary of overall recoil rates in the composite detector and probability of gamma-ray accidentals within the 76 µs thermalization window. Predicted probabilities based on the overall rate are compared to experimental results.

	All Events	Events >400 keVee
Recoil Rate (s^{-1})	2.1×10^4	5.6×10^3
Average Time Between Events (µs)	48	177
Probability of Event Within 76 µs (%)	79.5	34.9
% of Captures with Preceding Event Within 76 µs	74.0	33.9

Recoil-based organic liquid scintillators are poorly suited to detecting lower-energy

primary delayed neutrons because those neutrons are unlikely to produce a response above a detection threshold of about 100 keVee. However, higher-energy prompt neutrons from delayed fission can be easily detected, as they are far more likely to produce a pulse above the threshold. Fig. 3.9 shows the PSP and light output distributions measured by the EJ309 detector for HEU and DU, respectively. In the HEU data, a fast neutron recoil region around PSP=0.28 is readily apparent. However, this feature is entirely absent from the DU distribution. This stark contrast provides convincing evidence that the presence or absence of high-energy fission neutrons in the delayed neutrons spectrum can be used to perform isotopic discrimination.

3.4.2 Delayed Neutron Coincidence Analysis

Coincidence measurements were also used to detect the presence of delayed neutron-induced fission events. Coincidence time distributions were recorded for HEU and DU using two different detector pairings: composite-EJ309 and composite-NaI(Tl). In each case, the coincidence event rate recorded during the neutron generator off cycles was compared with the rate observed during passive measurement for each uranium object. Example coincidence time distributions measured during the delayed neutron window are shown in Fig. 3.10 for the composite-EJ309 and composite-NaI(Tl) detector pairings, respectively. The prominent coincidence peaks provide a clear indication that fission events continue to take place during the delayed neutron window. A summary of the measured coincidence rates for each detector pairing and scenario is presented in Table 3.4.

Because both samples contain ^{238}U, which undergoes spontaneous fission, the comparison between HEU and DU is not as simple as noting the presence or absence of coincident radiation from fission. While the relative change in the total coincidence rate after interrogation (when delayed neutrons are present) is much greater for HEU, suggesting that much of the change is due to delayed neutron-induced fission events, this interpretation

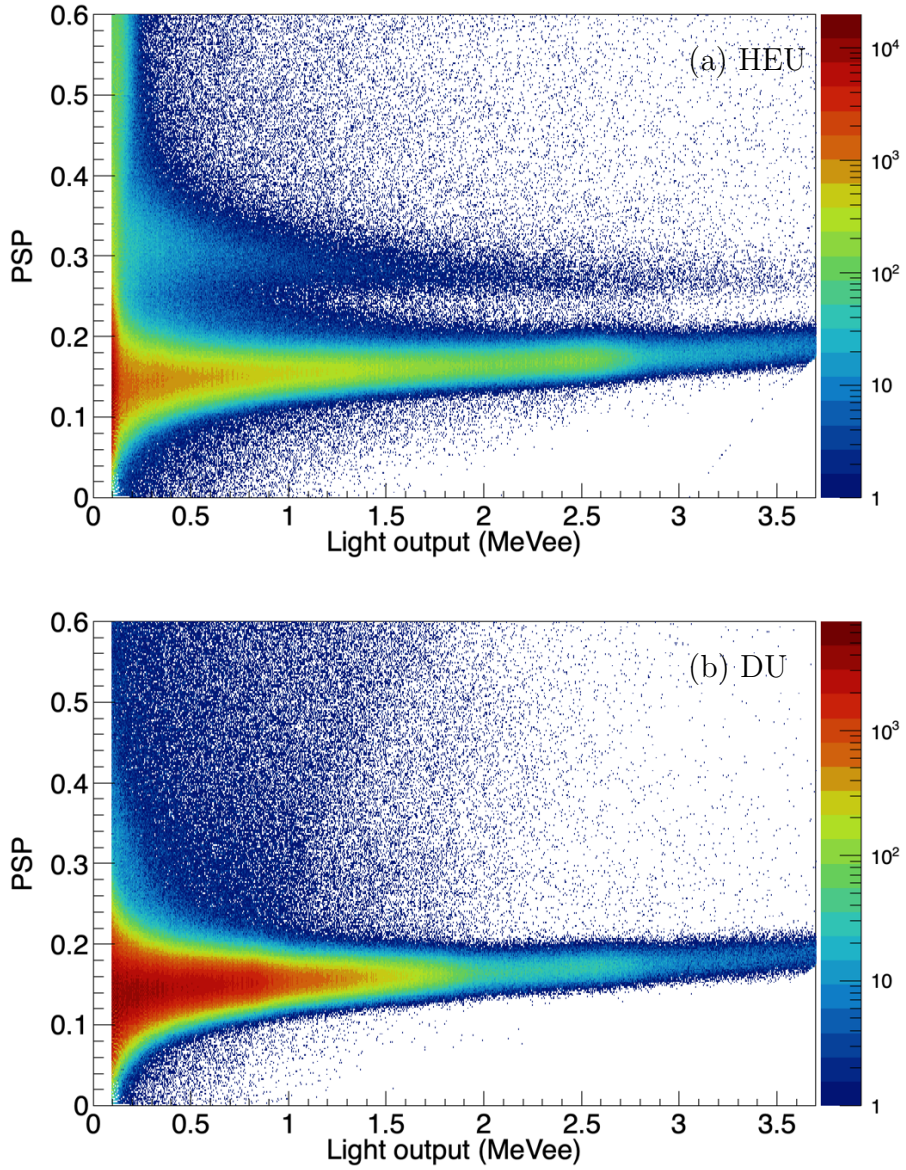

Figure 3.9: *PSP* and light output distributions measured in EJ309 for (a) HEU and (b) DU.

must be weighted against a number of complicating factors.

The measured passive coincidence rates for each material are too high to be attributed to spontaneous fission alone. ^{238}U has a specific activity of 12.44 MBq/kg, and a spontaneous fission probability of 5.4×10^{-7} per decay. Thus, based on the material composition

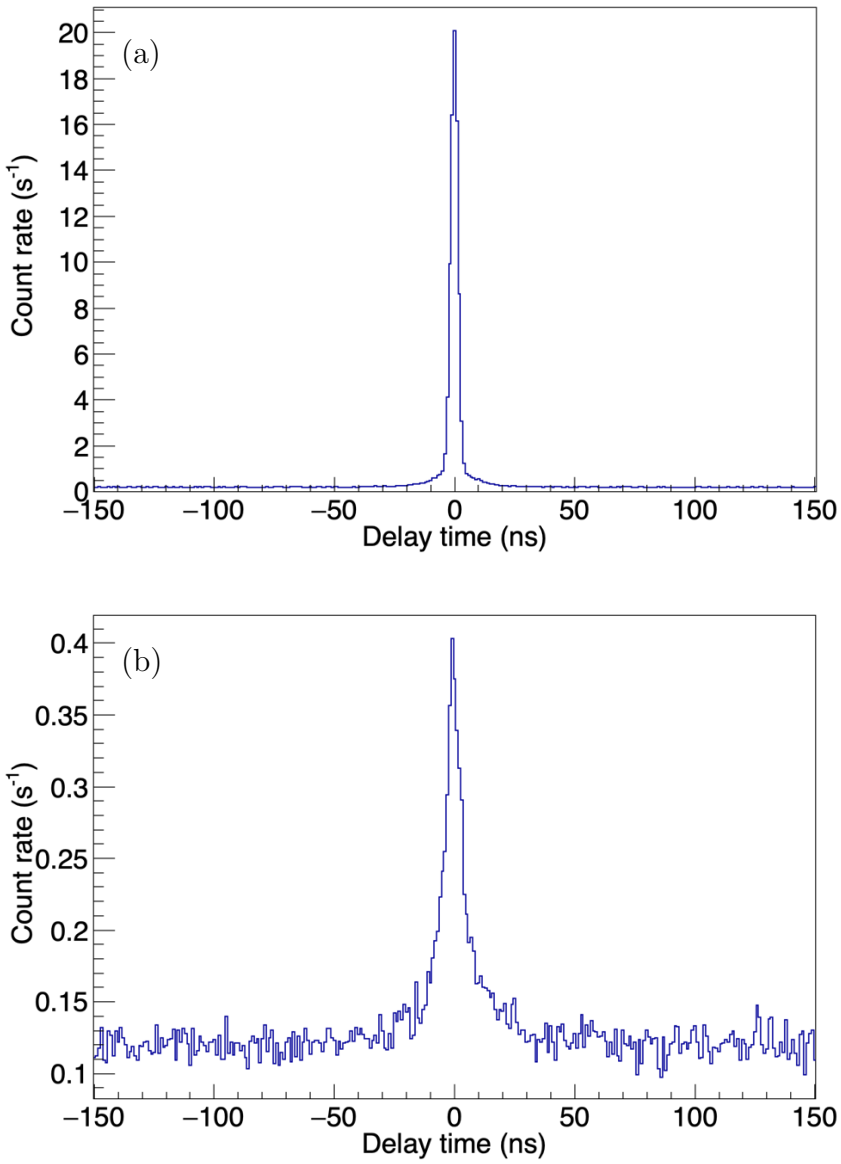

Figure 3.10: Coincidence time distributions for HEU measured during the delayed neutron time window based on (a) composite-EJ309 and (b) composite-NaI(Tl) detector pairings.

and total mass, the expected spontaneous fission rate for the DU and HEU objects would be 87 fission/s and 5 fissions/s, respectively. MCNPX simulations of the experimental configuration show that the probability of a fission event producing observable coincident pulses in the composite and EJ309 detectors is 0.3% for HEU and 0.053% for DU. For

Table 3.4: Measured coincidence rates for HEU and DU for composite-EJ309 and composite-NaI(Tl) detector pairings. For each material, the coincidence rate observed during delayed signal measurements was compared to the coincidence rate for passive measurements.

	HEU	DU
Composite-EJ309		
Passive Rate (s^{-1})	55.87 ± 0.70	50.30 ± 0.34
Active Rate (s^{-1})	89.17 ± 0.25	58.90 ± 0.16
% Change	60%	17%
Composite-NaI(Tl)		
Passive Rate (s^{-1})	1.70 ± 0.25	2.62 ± 0.14
Active Rate (s^{-1})	3.78 ± 0.10	2.91 ± 0.07
% Change	122%	11%

coincidence pulses in the composite and NaI(Tl) detectors, the probabilities are 0.08% and 0.0006% for HEU and DU, respectively. Table 3.5 shows the expected spontaneous fission (SF) tagging rates for each object based on the calculated spontaneous fission rates and simulated tagging probabilities.

Table 3.5: Simulated spontaneous fission (SF) rates, tagging probability, and expected tagged event rates for HEU and DU using each detector pairing.

	HEU	DU
Composite-EJ309		
SF Rate (s^{-1})	5	87
Tagging Probability	0.30%	0.053%
Tagged Event Rate (s^{-1})	0.015	0.046
Composite-NaI(Tl)		
SF Rate (s^{-1})	5	87
Tagging Probability	0.08%	0.006%
Tagged Event Rate (s^{-1})	0.004	0.0052

In both the case of HEU and DU, the expected tagging rates are several orders of magnitude lower than the experimentally observed coincidence rates. Further investigation of the coincidence pulses showed that they were consistent with true recoil events and not caused by spurious sources such as electronic noise. The measurement environment at Device Assembly Facility is complex, with many other objects near the experimental setup

being subjected to bombardment by 14.1-MeV neutrons, so the high coincidence rates may be partially explained by gamma-ray radiation from neutron activation products. In addition to any fission byproducts within the test objects, the entire experimental array was placed on a carbon steel table, so coincident gamma rays from ^{60}Co (produced by neutron irradiation of Fe) may be a contributing factor. While MCNPX simulations show the likelihood for crosstalk to be low (<2% for the composite-EJ309 pairing, negligible for composite-NaI(Tl)), a high background gamma-ray flux due to activation following the neutron generator operation could lead to an appreciable coincidence signal in the composite-EJ309 detector pairing due to crosstalk.

With respect to thermal neutron background, MCNPX simulations show that thermal neutrons incident on the HEU object are about 70% as likely to produce coincident pulses as spontaneous fission events within the object when averaged over all directions, and much more likely to produce coincident pulses when incident near the EJ309 and composite detectors. As such, even a small thermal neutron flux could cause an appreciable change to the measured coincidence rate for HEU. Given that neutron-emitting calibration sources were present in the room during the experiment, it is possible that thermal neutron induced fission played a part in elevating the measured passive coincidence rates.

With the goal of eliminating events that were not caused by fission, the coincidence rates were reexamined while only accepting neutron recoil pulses from the EJ309 detector. Fig. 3.11 shows the coincidence time distributions for HEU and DU after interrogation with the neutron generator when only neutron recoil pulses are accepted from the EJ309 detector, with simulation results overlaid. Notably, the neutron-based coincidence time distribution for HEU is much broader than the corresponding distribution for DU and distributions where all event types were accepted. This is due to differences in the time of flight for different neutron energies, and perhaps to some extent by the fact that coincident pulses may be produced by radiation from different generations in the fission chain

reaction. The broadening of the HEU coincidence distribution is also accurately reflected in the MCNPX model, which has a full-width at half maximum (FWHM) of 15.7 ns, compared to 16.1 ns for the experimental data. The DU distribution also agrees well with simulation, including the asymmetry of the coincidence peak, which is caused by neutron events in the EJ309 detector. For this simulation, the best agreement with experimental data is achieved when only gamma-ray recoils are considered in the composite detector. This provides further support for the conjecture that low-energy neutrons often do not register a recoil pulse in the composite detector.

Table 3.6 presents a summary of the experimentally measured coincidence rates when the neutron recoil criterion is applied. When coincidence events are required to contain at least one neutron interaction, the differences between the HEU and DU coincidence rates become much more pronounced. In the case of DU, the coincidence rate more than doubles, even though delayed neutrons are not expected to cause an increase in coincidences due to fission. However, this is most likely due to an increased number of pileup events in the neutron recoil region for EJ309, as Fig. 3.9(b) suggests. While the passive coincidence rate for HEU is still quite high relative to expectation, it is much lower than when all events are considered. Given the presence of other neutron sources in the experimental space, it is also reasonable to assume that some of the discrepancy is accounted for by additional fissions caused by thermal neutrons. Most notably, the overall coincidence rate for HEU after interrogation is more than 100 times higher than the rate for DU, and the change in the HEU coincidence rate between the passive and

Table 3.6: Experimental fission tagging rates for HEU and DU using the composite-EJ309 detector pairing, with only neutron events accepted for the EJ309 detector.

	HEU	DU
Passive Rate (s^{-1})	0.442 ± 0.054	0.035 ± 0.007
Active Rate (s^{-1})	9.14 ± 0.07	0.079 ± 0.005
% Change	1968%	126%

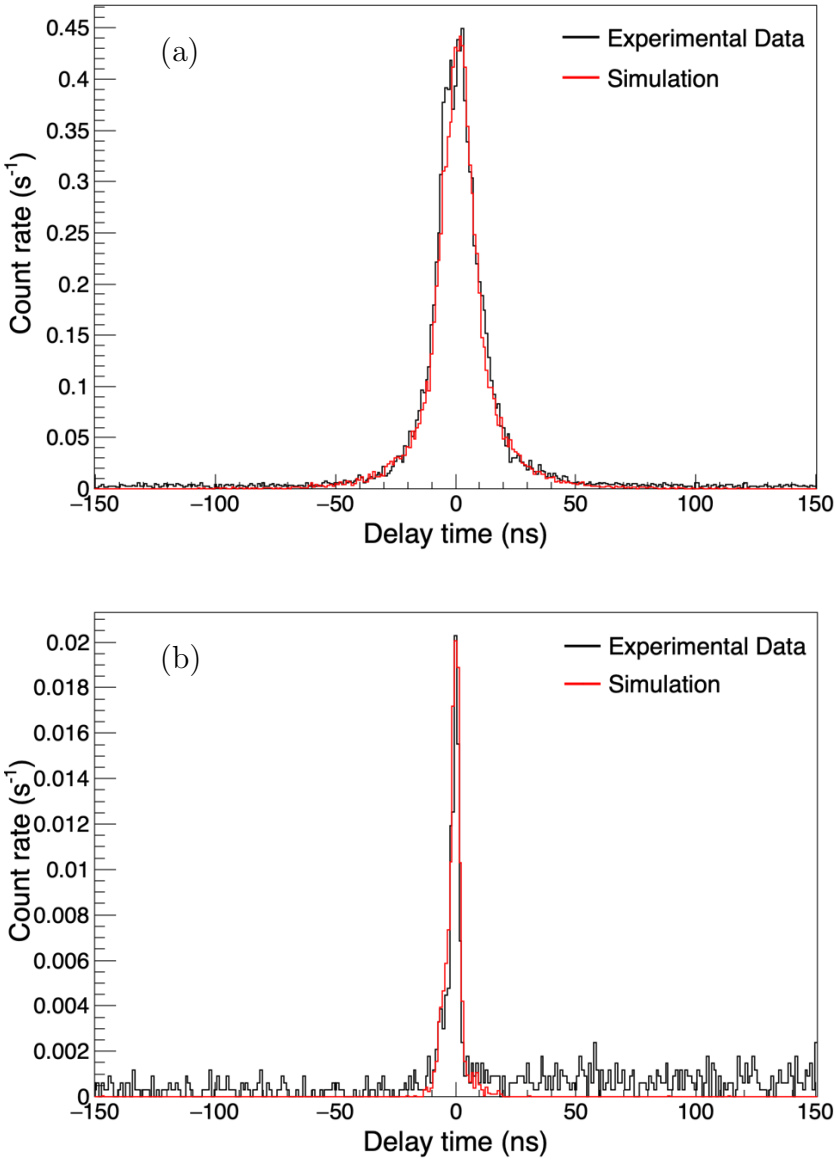

Figure 3.11: Coincidence time distributions using the composite-EJ309 detector pairing for (a) HEU and (b) DU, where only neutron recoil events are accepted in the EJ309 detector. Simulated distributions are overlaid in red.

active measurements is very significant, increasing by more than a factor of 20. This is consistent with the expectation that delayed neutrons will induce additional fission at a much greater rate in HEU than DU, providing the basis for discrimination.

Furthermore, the time evolution of the rate of coincidence events from fission can provide valuable information on the ^{235}U content of the test material. Because the delayed neutron groups for each uranium isotope constitute a unique set of decay time constants, the overall delayed neutron time emission profile can be used to discriminate between isotopes and infer enrichment. Delayed neutron-induced fission events occur on the same timescale as their delayed neutron precursors, so coincidence-based measurements of the rate of delayed fission events should exhibit the same temporal shape predicted for delayed neutron emission. Fig. 3.12 shows the time distribution of coincidence events for HEU in the period after the neutron generator has been turned off.

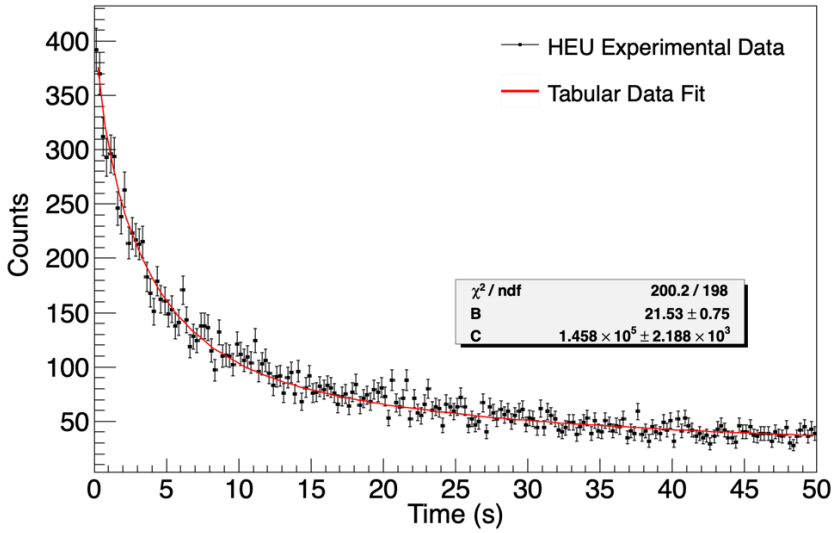

Figure 3.12: Time distribution of delayed coincidence events in HEU, measured using the composite-EJ309 detector pairing. Only neutron recoil pulses were accepted from the EJ309 detector. The fit is based on tabular nuclear data and parameterized with only a scaling factor (C) and constant background term (B).

The composite-EJ309 detector pairing was used again, but while accepting only neutron recoil events from the EJ309 detector. The experimental data are fitted with a parameterized model based on a six-group superposition of delayed neutrons, whose decay constants are obtained from tabular nuclear data; the procedure is described in

depth in Ref. [101]. The experimental results show close agreement with the model ($\chi^2 = 200.2/198$), which confirms that the coincidence events are caused by delayed neutron-induced fission and suggests that discrimination based on the delayed neutron time emission profile can also be performed using fast neutron measurements, provided that the material is fissionable by lower-energy delayed neutrons. The coincidence-based approach presented here could supplement the methods described in Ref. [101], providing an additional point of distinction between isotopes.

In conclusion, two measurement methods have been demonstrated for differentiating the components of delayed neutron signals in bulk samples of SNM based on their origin. Fission radiation coincidence counting and spectroscopic neutron energy measurements have been shown to provide a significant refinement in the ability to capture information on delayed neutron-induced fission as a means for performing isotopic identification. For fission rate measurements, high background gamma-ray rates hindered the usefulness of NaI(Tl) detectors, and detectors with the ability to discriminate fast neutron recoils were necessary to isolate the fission signature. For fissionable materials with large differences in fission cross-section at typical delayed neutron energies, such as ^{235}U and ^{238}U these types of measurements are sufficient to successfully perform isotopic discrimination. Further refinement of the capture-gated neutron spectroscopy technique to detect small changes in the delayed neutron energy signature would provide even greater precision in differentiating materials. The measurement approaches presented here have the potential to complement existing delayed neutron analysis techniques, and when employed in concert with methods that focus on time-dependent signatures, they may lead to even greater accuracy in SNM characterization.

Chapter 4

The Effects of Shielding on Delayed Neutron Temporal Signatures

As high-energy neutral particles, fast neutrons are able to easily penetrate most materials, which is particularly advantageous in measurement scenarios where shielding is present. In this chapter, the experiments from the fourth and final measurement campaign at the DAF are presented, which extends the study of delayed neutron time profiles from the second and third campaigns to shielded scenarios. Because the long-lived delayed neutron precursors exhibit decay times on the order of tens of seconds, their time profiles are insensitive to the delays associated with scattering or diffusion in shielding materials, which occur on much shorter time scales. The use of capture-based neutron detectors can also mitigate the effects of shielding, because unlike recoil-based detectors, they do not have a low-energy detection threshold, so that neutrons that lose their energy in the shielding are still detectable.

To investigate the effects of neutron-moderating shielding on the delayed neutron buildup and decay time profiles, polyethylene-shielded HEU and depleted uranium objects are measured using two different capture-gated detector designs. Simulations are used to explore the potential effects on isotopic discrimination and enrichment estimation at

intermediate enrichment levels and differing shield thicknesses beyond what could be tested during the experimental measurement. This chapter includes edited portions of the 2021 publication in *Nuclear Instruments and Methods in Physics Research, Section A*, entitled "The effects of low-Z shielding on uranium isotope discrimination using the time-emission profiles of long-lived delayed neutrons" [128].

4.1 Introduction

The detection and identification of SNM is a critical element of national security, nuclear material safeguards, and nonproliferation efforts. Across a wide variety of detection scenarios, there is a high probability that the SNM will be concealed by some degree of shielding, whether intentional or incidental [129, 130]. HEU presents an especially difficult case, as its passive signal of weak neutron emission and lower-energy gamma rays can be easily obscured by a relatively small amount of shielding [131]. Active interrogation can overcome shielding by probing the target material with penetrating radiation to induce nuclear reactions, such as fission, that emit a strong signal that may be much easier to detect than passive emissions [26].

Neutron-based active interrogation methods are suitable for shielded-SNM scenarios because neutrons have much longer attenuation lengths in materials that readily shield gamma rays, and much lower neutron signal rates are needed to establish the presence of SNM [104]. Differential neutron die-away measurements are a well-established technique for SNM detection [106, 107], which have been successfully employed to identify plutonium and HEU objects surrounded by significant shielding [132]. Delayed neutron signatures represent another long-established means for characterizing SNM [108, 109], and a wide variety of techniques have been developed for detecting fissionable materials by measuring the delayed neutron signals induced through active interrogation [27, 110, 111, 113].

In addition to detection, isotopic discrimination is an integral feature of many techniques for uranium assay, where the capability to distinguish between HEU and DU is desired [26]. Neutron die-away measurements can be used to estimate the isotopic composition of uranium, but they are often restricted to reporting an effective fissile mass, which must be compared against calibration standards or other *a priori* knowledge in order to determine ^{235}U content, and thus enrichment [133]. Delayed neutron time-emission profiles are also unique to the fissioning isotope, and previous studies have demonstrated that the decay time profile of short-lived and long-lived delayed neutron groups can be used to discriminate different types of SNM [114–117].

In prior work, it has been demonstrated that the buildup and decay time profiles of long-lived delayed neutron groups can provide the means to discriminate between ^{235}U and ^{238}U and infer the enrichment of uranium [101]. The isotopic determination is made by comparing the measured temporal profile against the expected shape derived from tabular nuclear data, eliminating the need for a calibration standard. Another powerful feature of using long-lived delayed neutrons as the basis for discrimination is that the shape of the time-emission profile is not sensitive to the presence of shielding. This is because the characteristic decay times for the six delayed neutron groups in ^{235}U and ^{238}U range from a few tenths of a second to tens of seconds [41], while neutron scattering and thermalization in shielding materials occurs on a much shorter time scale (nanoseconds to microseconds), so the temporal signature of the delayed neutrons is not significantly distorted by interactions with the shielding. In contrast, the neutron energy spectrum is altered by energy losses through interactions with the shielding material. As a result, recoil-based detectors may be less effective, as energy losses in the shielding reduce the number of neutrons that can produce recoils with energy above the detection threshold. Capture-based detectors offer an advantage in this situation, as they do not have a low-energy detection threshold, and the downward shift of the neutron energy spectrum can

improve the capture efficiency.

Delayed neutron measurements still face some potential limitations depending on the type and amount of shielding present. Specifically, different delayed neutron groups have different energy spectra, which may be attenuated at different rates by the shielding material. For the same reason, detector efficiencies may also vary depending on the delayed neutron energy spectrum. Notably, for bulk samples of HEU, most of the neutron signal observed during the delayed neutron time window can consist of prompt neutrons from fission induced by the delayed neutrons in the bulk material [102]. As a result, the effects of any preferential shielding based on neutron energy are mitigated in the case of HEU, since the secondary prompt neutrons exhibit a time-independent, Watt energy spectrum. Furthermore, because delayed neutrons from ^{235}U and ^{238}U have very similar mean energies, they induce secondary fission events in ^{235}U at similar rates. This means that, even at intermediate enrichments, the time profile of higher-energy secondary prompt neutrons will reflect the same relative isotopic proportions as the emitted delayed neutrons. This response to shielding differs somewhat from the differential die-away method, where shielding can increase multiplication through neutron reflection [134, 135], which may lead to an overestimate of fissile mass. In such scenarios, measurement of the delayed neutron time-emission profile can yield helpful complementary information that may help resolve potential ambiguities in the estimated isotopic content. The delayed neutron time profile can also be used to positively identify ^{238}U, which can be difficult to distinguish from background in a shielded configuration using die-away only [132].

In this chapter, delayed neutron time-emission profiles are measured for uranium objects surrounded by a neutron-moderating shield. Whereas the experiments described in Chapter 3 focused on measurements of bare uranium [101, 102], this study examines the effects of low-Z shielding on the measurement technique. HEU and depleted uranium objects are interrogated using a portable fast neutron generator, and the buildup and

decay time profiles of the long-lived delayed neutron groups are recorded using two different capture-based composite scintillator detector designs. The measured delayed neutron time profiles show good agreement with the expected shapes predicted from tabular nuclear data, demonstrating that uranium isotopes can be successfully differentiated on this basis even when neutron-moderating shielding is present.

4.2 Materials & Methods

The experimental measurements were performed at the DAF. As with the previous experiment presented in Chapter 3, a 13.8 kg HEU test object was constructed using the Rocky Flats shells, along with a DU object with a mass of 12.8 kg, which was the closest approximation of the HEU object mass achievable with the available materials. Further details on the uranium test objects can be found in Chapters 2 and 3, as well as Ref. [91].

Both uranium test objects were surrounded by a 1-inch thick spherical polyethylene shield. The thickness of the shield was chosen such that neutrons emitted by the test objects had a high probability of interacting with the shield, yet the attenuation was not so great as to severely inhibit the measurement statistics given the limited experimental time available at the DAF. For delayed neutrons with energy of 250–500 keV, the probability of interacting in a 1-inch layer of polyethylene is 80–90%, which was estimated from transmission calculations based on tabular cross-section data in the ENDF/B-VII.1 library [136]. For prompt neutrons from delayed-neutron-induced fission, which have a mean energy of approximately 2 MeV, the interaction probability is still greater than 50%.

The test objects were surrounded by an array of detectors including NaI(Tl), Eljen EJ309 organic liquid scintillators [93], and custom-built capture-based composite detectors. The composite detectors all consist of ^{6}Li-enriched glass suspended in a cylindrical

matrix of scintillating polyvinyl toluene (PVT), though they differ in their geometrical design. The first design, which is described in detail in Chapter 3, features square rods of lithium glass embedded in a cylinder of PVT with height and diameter of 12.7 cm. In the second design, described in detail in Ref. [137], the lithium glass is ground into small shards and distributed throughout the PVT matrix, providing similar neutron capture discrimination at a much lower construction cost. Two different shards-type detectors were used in the experiment, with lithium glass loading of 7% and 3% by weight, respectively. The principle of operation for the composite detectors is presented in Chapter 3.

Neutron capture events were identified in the composite detectors both by their pulse shape and the characteristic Q-value of the ^{6}Li(n,t)^{4}He capture reaction. As in previous measurements, a pulse shape parameter (PSP) value was defined for each waveform using Eq. (2.1). Fig. 4.1 shows the PSP and light output distribution for the rods- and shards-type composite detectors when exposed to an AmBe source for calibration. For both detectors, a clear capture region is distinguishable, which is located in the parameter space between PSP values of about 0.45 and 0.65, and between light outputs of 0.5 and 0.7 MeVee. Gaussian fits were used to define a 3-σ cut in both the PSP and light output dimensions around each capture region, and any pulses falling within the cut region were classified as neutron captures.

Figure 4.2 shows the experimental setup used for both uranium object measurements. The shards-type composite detectors were placed at a distance of about 22 cm from the center of the test object, while the rods-type composite, NaI(Tl), and EJ309 detectors were placed at a distance of about 28 cm. The output of each detector was digitized using a CAEN DT5730 14-bit, 500-MHz desktop waveform digitizer with digital-pulse-processing pulse-shape-discrimination (DPP-PSD) firmware. Light output pulse data were collected in list mode, with short-gate (Q_{short}) and long-gate (Q_{long}) charge integrals recorded for each waveform to provide the basis for pulse shape discrimination. The

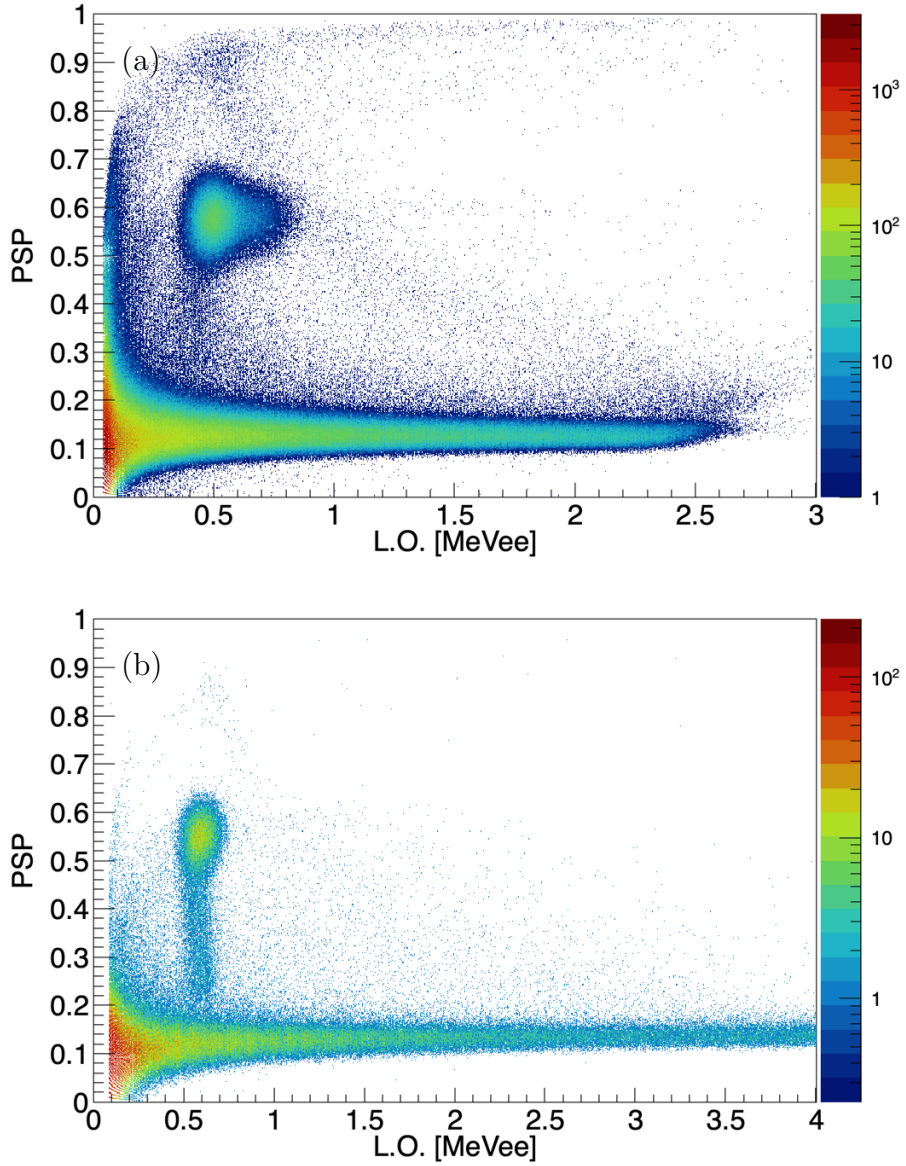

Figure 4.1: PSP and light output distribution for the (a) rods- and (b) shards-type composite detectors when exposed to an AmBe source. Neutron captures were identified using a 3-σ cut around the island feature centered at $PSP = 0.55$ and light output of approximately 0.6 MeVee.

leading edge threshold-crossing trigger time in the digitizer, t_{start}, was used as the pulse time stamp. The fine time stamp step resolution is 2 ps, and the trigger time stamp resolution is 2 ns [138]. The boundary parameters for the charge integration regions were

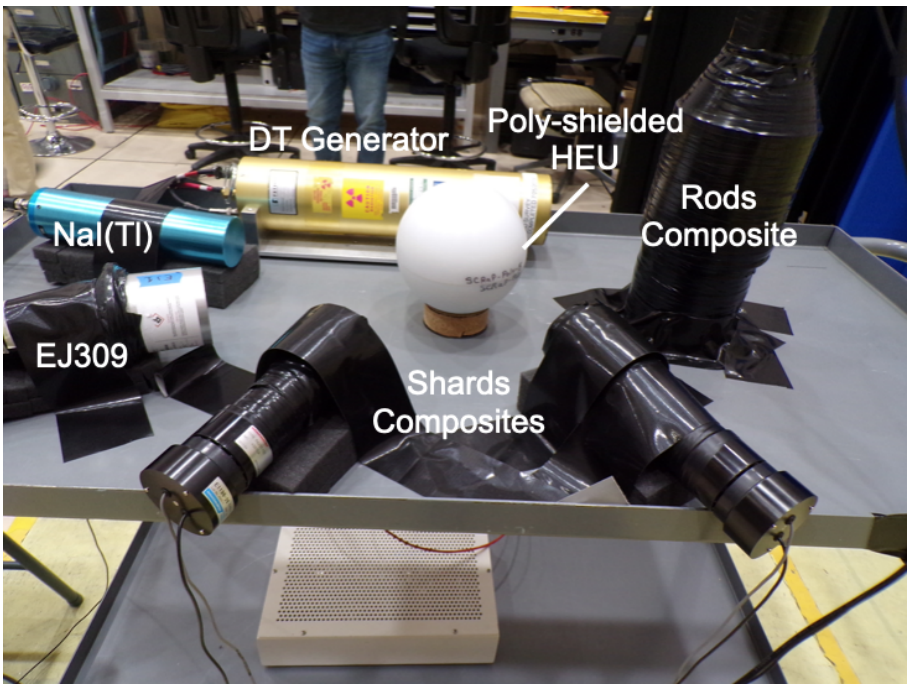

Figure 4.2: Experimental setup during measurement of the HEU object.

defined relative to t_{start}, with Q_{short} integrated from $t_{\text{start}} - t_{\text{offset}}$ to $t_{\text{start}} + t_{\text{short}}$, and Q_{long} integrated from $t_{\text{start}} - t_{\text{offset}}$ to $t_{\text{start}} + t_{\text{long}}$, where t_{offset} is the offset time prior to the start of the waveform, and t_{short} and t_{long} are the endpoints for the short-gate and long-gate integration windows, respectively. A summary of the integration parameters for each detector is presented in Table 4.1.

Table 4.1: Waveform integration parameters.

Detector	t_{offset} (ns)	t_{short} (ns)	t_{long} (ns)
Rods Composite	24	36	376
7% Shards Composite	24	36	376
3% Shards Composite	24	36	376
EJ309	24	36	376
NaI(Tl)	24	200	776

The uranium objects were interrogated with 14.1-MeV neutrons produced by a Thermo Scientific P211 DT neutron generator, with an approximate isotropic yield of 10^8 n/s. Each object was placed 20 cm from the generator, as measured from the center of the

object to the source location within the DT generator. Across all measurements, the DT generator was operated at a pulse rate of 100 Hz, with a pulse width of approximately 10 µs. To record the delayed neutron time profiles, the neutron generator was operated in a series of on/off cycles over measurement time of about 2.5 hours for each object. During each cycle, the generator was turned on for one minute, then off for one minute. Delayed neutron decay data were recorded when the generator was off, while the buildup data were acquired between generator pulses while it was on. Passive measurements were also recorded for the HEU and DU assemblies over a period of 10 minutes each, and the detectors were calibrated using ^{137}Cs, ^{60}Co, and AmBe sources.

4.3 Results

The temporal profile of delayed neutron emission in uranium is parameterizable based on the enrichment of the sample and tabular nuclear data for the associated delayed neutron groups. Using the six-group delayed neutron framework, the buildup of delayed neutron emission for a mixed sample of ^{235}U and ^{238}U can be expressed as

$$R_b(t) = B + C \sum_{i=1}^{2} \sum_{j=1}^{6} f_i P_i Y_{i,j} \epsilon_{i,j} \left[1 - \exp(-t/\tau_{i,j})\right], \tag{4.1}$$

where $R_b(t)$ is the detected rate of delayed neutron buildup at time t, B is the constant neutron background rate, C is a scaling constant, index i denotes the uranium isotope, index j denotes the delayed neutron group number, f_i is the probability of 14.1-MeV neutron induced fission for isotope i, P_i is the fraction of isotope i in the sample, $Y_{i,j}$ is the delayed neutron yield per fission for group j of isotope i, $\epsilon_{i,j}$ is the detection efficiency for group j of isotope i, and $\tau_{i,j}$ is the decay time constant for group j of isotope i. The corresponding expression for the decay of delayed neutron emission, $R_d(t)$, is described

by

$$R_d(t) = B + C \sum_{i=1}^{2} \sum_{j=1}^{6} f_i P_i Y_{i,j} \epsilon_{i,j} \left[\exp(t_b/\tau_{i,j}) - 1\right] \exp(-t/\tau_{i,j}), \tag{4.2}$$

where the additional parameter t_b represents the time period over which the constant-intensity active interrogation source is turned on [113].

The buildup profile of the delayed neutron population was measured by recording neutron capture events in the detectors between generator pulses while the generator was on. To eliminate interference with the delayed neutron signal caused by die-away from the neutron generator, a veto window was applied after the end of each generator pulse. A veto window length of 3 ms was chosen, after which the vast majority of prompt neutrons have died away [101]. The delayed neutron buildup signal was then recorded in the time following the veto window and before the start of the next generator pulse. The delayed neutron buildup profiles for HEU and DU measured by the rods-type composite detector are shown in Fig. 4.3. The measured buildup profiles show good agreement with the shapes predicted by Eq. (4.1) for HEU and DU.

The delayed neutron decay time profile was measured by recording neutron capture events over the time period when the generator was turned off. As with the buildup measurement, a veto window of a few ms was applied immediately after the generator was turned off to account for neutron die-away. Fig. 4.4 shows the delayed neutron decay time profiles for HEU and DU measured with the rods-type composite detector. Once again, the measured data show good agreement with the shapes predicted by Eq. (4.2).

For both the buildup and decay time profile measurements, the agreement between the measured data and the models in Eqs. (4.1) and (4.2) show that this technique can discriminate and identify HEU and DU even in the presence of 2.5 cm of polyethylene shielding. To quantify the discrimination of HEU and DU, the reconstructed enrichment for each sample was determined according to the method detailed in Ref. 101. In this method, the neutron count rate is integrated over two different regions of the delayed

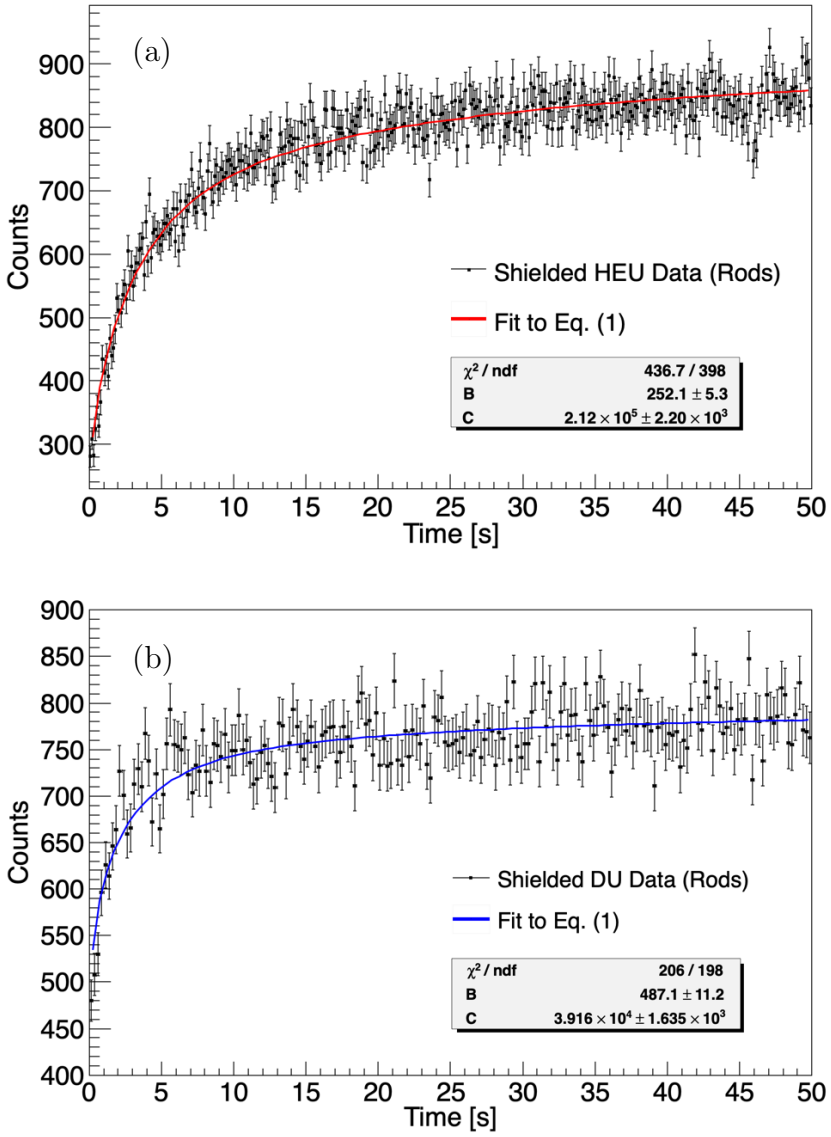

Figure 4.3: Delayed neutron buildup time profiles for (a) HEU and (b) DU measured with the rods-type composite detector. The fit based on Eq. (4.1) is shown in red for HEU and blue for DU.

neutron time profile, A_1 and A_2. The bounds of A_1 and A_2 are defined as $[t_0, t_0 + 30\text{ s}]$ and $[t_0, t_0 + 3\text{ s}]$, respectively, where t_0 is the beginning of the delayed neutron window after the interrogation source has been turned off. The ratio of those two integrals serves as a pulse shape parameter related to the proportional contribution of the ^{235}U and

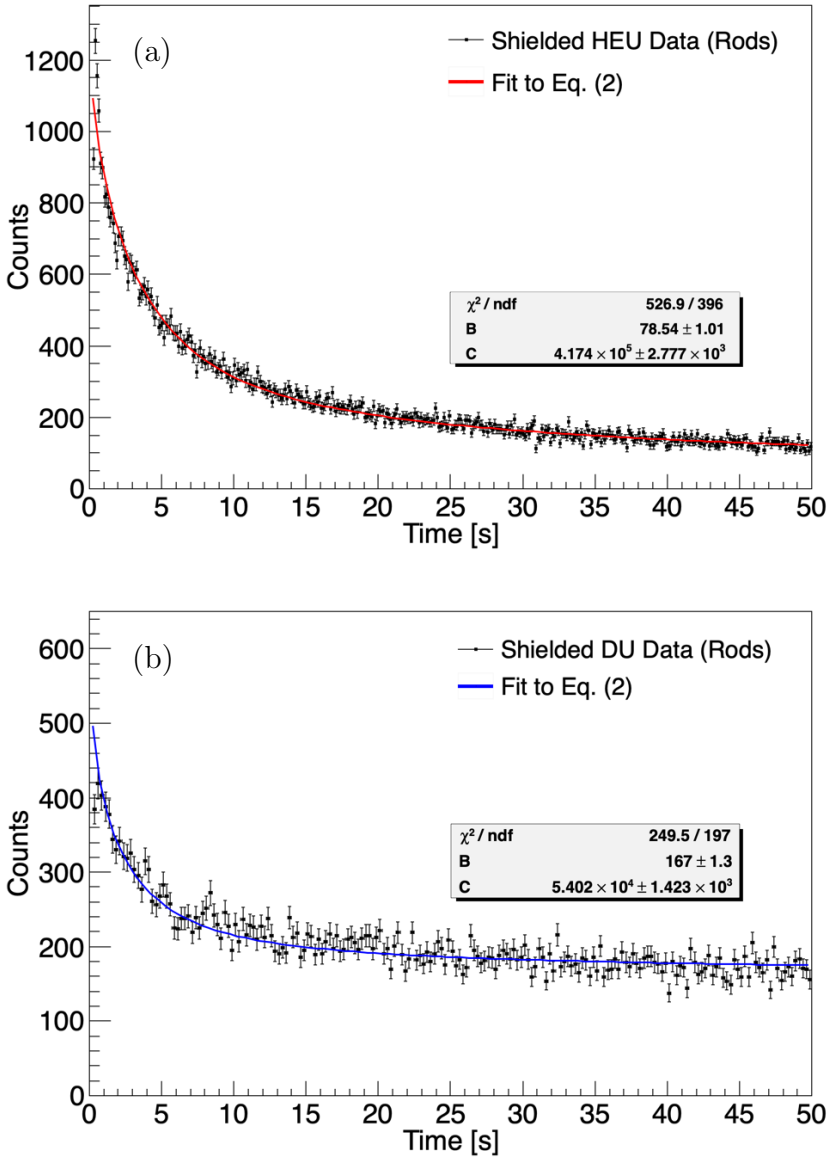

Figure 4.4: Delayed neutron decay time profiles for (a) HEU and (b) DU measured with the rods detector. The fit based on Eq. (4.2) is shown in red for HEU and blue for DU.

^{238}U profiles, which is used to reconstruct enrichment. The conversion from the integral ratio to reconstructed enrichment is determined by interpolation of the simulated delayed neutron profile results at various enrichment levels from 0 to 100%. Table 4.2 shows the reconstructed enrichment values based on the delayed neutron decay time profiles for

HEU and DU, which are both within 1-σ error of the true enrichment.

Table 4.2: Reconstructed enrichment for HEU and DU objects based on the delayed neutron decay time profile shape.

Sample	Reconstructed Enrichment (%)
HEU	$96.1^{+3.9}_{-4.7}\%$
DU	$0^{+5.1}_{-0}\%$

It is worth noting that Eqs. (4.1) and (4.2) are defined for the unshielded scenario, and do not include a parameter for the transmission of individual delayed neutron groups through a certain thickness of shielding material. The fact that the fit to experimental data is still good despite the omission of such a quantity suggests that transmission is relatively constant across delayed neutrons groups, and thus the difference from the unshielded case is adequately accounted for by the simple scaling constant. This raises the question of to what extent transmission through the shielding is influenced by the characteristics of different delayed neutron groups, and whether there may be shielding scenarios where the shapes of the delayed neutron time profiles are significantly altered by the presence of shielding.

Similarities in the energy spectra for the individual ^{235}U and ^{238}U delayed neutron groups [139] suggest that shielding materials are unlikely to preferentially attenuate one group over another to an extent significant enough to influence the overall emission time profile. To test this idea, simulations were performed using the Geant4 Monte Carlo framework [92] to model the transmission of delayed neutrons from each individual group through various thicknesses of polyethylene shielding. Table 4.3 shows the results for ^{235}U, and Table 4.4 shows the results for ^{238}U. For both isotopes, the group 1 delayed neutrons are attenuated slightly more than the delayed neutrons from groups 2–6, which have very similar transmission rates. However, the group 1 yields for ^{235}U and ^{238}U are only 3.8% and 1.3% of the total yield, respectively. Furthermore, the high likelihood

Table 4.3: Simulated ^{235}U delayed neutron transmission through various thicknesses of polyethylene shielding.

Group	Yield (%)	Avg. Energy (MeV)	Transmission (%) 1 cm	2.5 cm	5 cm	10 cm
1	3.8	0.265	44.6	17.3	6.24	1.42
2	21.3	0.457	51.8	23.1	8.80	2.08
3	18.8	0.465	52.0	23.4	8.94	2.11
4	40.7	0.487	52.5	24.0	9.25	2.19
5	12.8	0.481	52.0	23.6	9.17	2.16
6	2.6	0.496	53.0	24.2	9.37	2.26

Table 4.4: Simulated ^{238}U delayed neutron transmission through various thicknesses of polyethylene shielding.

Group	Yield (%)	Avg. Energy (MeV)	Transmission (%) 1 cm	2.5 cm	5 cm	10 cm
1	1.3	0.240	43.6	16.5	5.90	1.34
2	13.7	0.490	53.3	24.4	9.28	2.14
3	16.2	0.408	50.1	21.8	8.21	1.90
4	38.8	0.465	51.9	23.2	8.93	2.10
5	22.5	0.437	50.8	22.5	8.52	2.02
6	7.5	0.462	52.0	23.4	8.93	2.05

of delayed-neutron-induced fission in ^{235}U serves to further mitigate the differences in transmission between individual delayed neutron groups. Because the observed neutron signal during the delayed neutron time window is dominated by prompt neutrons from fission induced by delayed neutrons, and those prompt neutrons follow the Watt fission energy spectrum, any differences in transmission due to variations in the delayed neutron group energy spectra will be diminished. As a result, uranium samples containing a significant quantity of ^{235}U are unlikely to exhibit distortion in the delayed neutron time profiles due to transmission through shielding alone, and transmission-based distortion of the time profiles for DU would depend on variations in the relative transmission of delayed neutrons that make up only about 1% of the total yield. Further work may be required

to determine if resonances in the neutron interaction cross-sections for other materials such as copper, iron, and lead could cause more significant variations in transmission, but the broad similarities of the delayed neutron group energy spectra are likely to have a mitigating effect in these materials as well.

Apart from transmission, it is also important to consider the effects of neutron reflection by the shielding materials. Because ^{235}U is much more likely to be induced to fission by lower-energy neutrons, delayed neutrons that are moderated and reflected by the shielding material will disproportionately induce additional fission events in ^{235}U relative to ^{238}U, which may bias the delayed neutron decay time profile more toward ^{235}U than is warranted by the material composition, leading to an overestimate of enrichment. To investigate the effects of neutron reflection on the shape of the delayed neutron time profile, the delayed neutron profiles following 14.1-MeV neutron interrogation of uranium at various enrichment levels were modeled using MCNP6 [140]. When no shield is present, the results agree closely with the predictions from Eqs. (4.1) and (4.2). When a 2.5 cm thick spherical polyethylene shield is included in the model, the delayed neutron decay time profiles for HEU and DU deviate only slightly from the unshielded case, with the difference being more noticeable for DU. Figs. 4.5a and 4.5b show a comparison of the simulated delayed neutron time profiles with and without shielding for HEU and DU, respectively. In contrast, the simulated delayed neutron time profiles for intermediate enrichment levels show a much greater difference between the bare and shielded configurations. Figs. 4.5c-4.5e show a comparison of the simulated delayed neutron time profiles with and without shielding for uranium enrichment levels of 5%, 20%, and 50%, respectively. To provide a quantitative metric for assessing the deviation of the shielded and unshielded profiles, a residual was calculated by subtracting the unshielded profile from the shielded one. The residuals for each enrichment level are given in Table 4.5, where the residual is expressed as the percent change in the total profile integral from

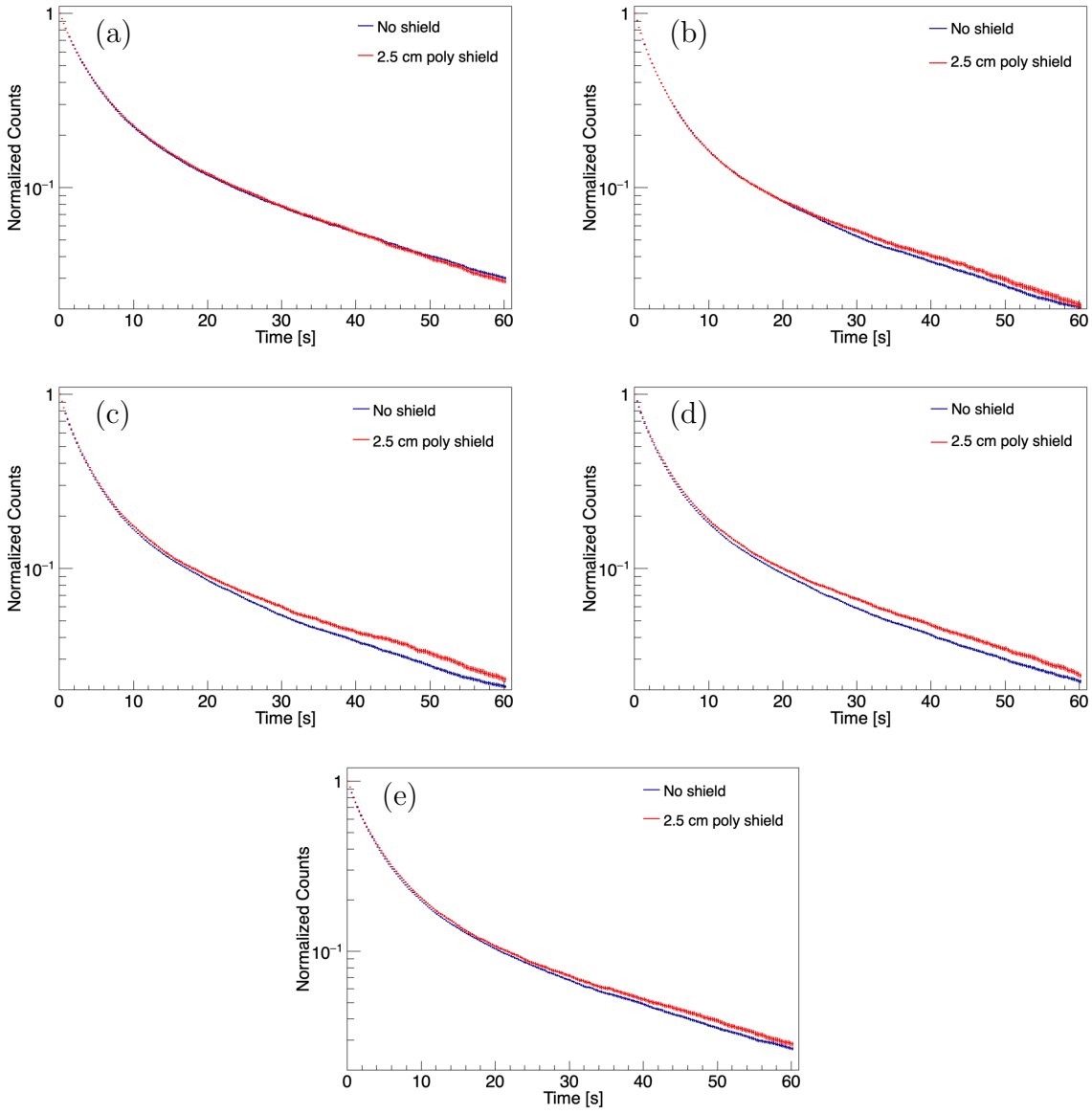

Figure 4.5: Simulated delayed neutron decay time profiles with and without polyethylene shielding for (a) HEU, (b) DU, (c) 5% enriched LEU, (d) 20% enriched LEU, and (e) 50% enriched HEU.

0 to 30 seconds. The integration time bounds were chosen to align with the integration boundaries used in the enrichment reconstruction calculations.

Based on the simulation results, it is clear that the shape of the delayed neutron time profile is not entirely impervious to the effects of shielding. Although the effects

Table 4.5: Residual difference between the delayed neutron decay time profile for the unshielded and shielded (2.5 cm poly) case. The residual is expressed in relative terms as the percent change in the total profile integral from 0 to 30 seconds (the time period used to determine reconstructed enrichment).

Enrichment (%)	Residual (%)
0.2	0.25
5	3.28
20	4.18
50	2.68
93	1.40

of shielding appear to be small for the high and low extremes of enrichment, where a single isotope dominates the delayed neutron spectrum, intermediate enrichment levels are susceptible to significant skew caused by preference for fissions in ^{235}U induced by lower-energy neutrons reflected from the shielding. This preference arises from the difference in the total neutron-induced fission cross-section between ^{235}U and ^{238}U, which is 4–5 orders of magnitude greater for ^{235}U over the delayed neutron energy range (approximately 100 keV to 1 MeV) [136]. The shift to a higher proportion of delayed neutron counts at longer times after interrogation, which can be seen in Figs. 4.5c-4.5e, is consistent with an over-representation of ^{235}U in the composite profile. To quantify the effects of such distortions in the delayed neutron time profile on estimates of enrichment, the enrichment was reconstructed from the simulated delayed neutron time profile using the integration method from Ref. 101, which was described previously. A summary of the reconstructed enrichment estimate for bare and shielded (2.5 cm and 5 cm thick) configurations of uranium at five different enrichment levels is presented in Table 4.6.

For the intermediate enrichment levels, the inclusion of the 2.5-cm thick polyethylene shield leads to a significant overestimate of the enrichment of the uranium sample. The extreme cases of HEU and DU are affected substantially less, which is consistent with the experimental results showing close agreement with the prediction from tabular data for a bare configuration, despite the presence of the polyethylene shield. While the rel-

Table 4.6: Reconstructed enrichment based on simulated delayed neutron time profiles at various enrichment levels. Statistical error is less than 0.1% for each simulation (10^8 simulated events).

	Reconstructed Enrichment (%)		
Enrichment (%)	No Shield	2.5 cm Poly	5 cm Poly
0.2	0.15	0.47	3.2
5	5.1	14.0	46.5
20	20.0	39.5	50.1
50	50.2	65.2	76.2
93	92.9	100	98.4

ative difference between the reconstructed enrichment for DU in the shielded (2.5 cm) and unshielded case is large, the small absolute change does not prevent it from being correctly identified as DU, and even in the case of thicker shielding (5 cm), easily discriminated from HEU. Furthermore, the ability to discern the small changes in the delayed neutron profile associated with such small changes in enrichment would require exceptionally high measurement statistics. This result implies that measurements of the delayed neutron time profile may still be used to identify and differentiate extreme enrichment cases (weapons-grade HEU, DU). Although intermediate enrichment levels may require additional information on shielding materials or complementary measurements to resolve ambiguities, the ability of delayed neutron time profile measurements to discriminate weapons-grade HEU from other uranium enrichment levels, even in the presence of shielding, could be a useful tool in a treaty verification setting.

4.4 Summary

In conclusion, it has been demonstrated that the buildup and decay time profiles of long-lived delayed neutrons emitted by HEU and DU can be accurately measured even in the presence of neutron-moderating shielding. The measurement of long-lived delayed neutron time profiles has already been shown by prior work to be effective means for

discriminating uranium isotopes without the need for a calibration standard, and this work provides experimental evidence that the method is also applicable in shielded scenarios at the high and low extremes of enrichment. Simulated results show that while transmission through shielding material is unlikely to distort the shape of the temporal profile, neutron reflection can lead to a significant overestimate of enrichment, especially at intermediate enrichment levels. The shielding-resilient nature of delayed neutron time profile measurements at the extremes of enrichment may increase their attractiveness in many nonproliferation applications that require determination of the presence or absence of weapons-grade HEU. Specifically, treaty verification scenarios stand to benefit from this method, as it would allow an accurate confirmation of the presence or absence of HEU, even with incidental shielding in place, such as a storage cask or missile housing that the host would not want to open. Delayed neutron time profile measurements also provide a useful complement to other methods, such as die-away or multiplicity counting, which allows for cross-checks and confirmation of results in different domains.

Further work is needed to determine the effects of a broader range of shielding materials and configurations which may be present during verification measurements. Experimental measurements of the delayed neutron time profiles for intermediate enrichment levels of uranium could provide validation of the simulations presented in this study and place defined limits on the applicability of the method over the full range of uranium enrichment. Studies involving higher-Z shielding materials, such as tungsten, lead, or depleted uranium, could provide additional insight into the effects on the delayed neutron time profile under different reflection or multiplication conditions. Finally, an investigation of the effects of shielding materials with neutron interaction cross-section resonances (*e.g.*, iron, copper, lead) may be useful to determine if such resonances can influence the relative transmission of delayed neutron groups, or if the resonant interactions can provide information about the characteristic energy spectrum of the delayed

neutron source.

Chapter 5

Calibration Source Development for Large Antineutrino Detectors

Besides inducing fission, fast neutrons possess enough energy to drive a wide variety of nuclear reactions, such as (n,p), (n,xn), and (n,α). Many of the radioisotopes that result from these reactions are impractical to produce by other means, and may be useful as detector calibration sources. One prominent example involves the calibration of large-scale antineutrino detectors, which require extensive background suppression methods in order to successfully isolate rare antineutrino interactions. Correlated-particle calibration sources are especially useful in this regard, as the timing information of the coincident particles improves background rejection and event reconstruction.

In particular, ^{16}N and ^{17}N are radionuclides that can be produced via (n,p) reactions in oxygen-containing targets and are of interest for the calibration of large water-based Cherenkov detectors used for antineutrino detection. ^{16}N emits high-energy, beta-correlated gamma rays, while ^{17}N is a beta-delayed neutron precursor, making them both interesting as potential correlated-particle calibration sources. In this chapter, demonstrations of the production of ^{16}N and ^{17}N using a DT generator neutron source are presented, and time-correlated measurements conducted using a specialized beta-tagging

detector are used to examine the feasibility of ^{17}N as a time-tagged neutron source for antineutrino detector calibration.

5.1 Introduction

Antineutrino signals have long been recognized as a useful means for monitoring nuclear reactors [141], which is of great interest in the field of nuclear security and nonproliferation. Antineutrino measurements at reactors in the former Soviet Union and United States have demonstrated the ability to determine the reactor operational state (on or off) and power level, as well as the changes in the antineutrino rate and spectrum associated with fuel composition changes due to burnup [142–145]. Such signals are of great interest for treaty verification applications, as they could provide the means for discovery of undeclared nuclear reactors or detection of operational modes associated with plutonium production or material diversion [23].

Because nuclear reactors produce such large quantities of antineutrinos, which are impossible to shield and thus travel long distances, antineutrino detectors offer the potential for remote nuclear reactor monitoring. Naturally, as the standoff distance increases, larger detector sizes are needed to maintain an appreciable interaction rate. It is estimated that standoff distances beyond about 10 km require a kiloton-scale detector mass, which increases to the megaton-scale for distances on the order of 100–200 km [23]. For such massive detectors, only low-cost, highly-scalable fill materials are feasible, such as water or liquid scintillator. At the larger end of the scale, water-based detectors appear most promising, as liquid scintillator becomes too expensive and impractical to implement for detector sizes greater than a few kilotons [146]. Currently, the goal of the US-UK WATCHMAN Collaboration is to demonstrate far-field reactor monitoring using a kiloton-scale water-based antineutrino detector [147].

The use of hydrogenous detectors to observe the inverse beta decay (IBD) reaction,

$$\bar{\nu}_e + p \rightarrow e^+ + n, \tag{5.1}$$

is a long-established means for recording antineutrino signatures [148]. However, in pure water detectors, the flash of Cherenkov light produced by the recoiling positron can be challenging to distinguish from the response to other radiation types, including gamma rays, cosmogenic muons and neutrons, and neutrinos from other sources [23]. To enable better isolation of the antineutrino signal, gadolinium is added to the water as a dopant in concentrations of a few tenths of a percent [149]. ^{155}Gd and ^{157}Gd, which account for about 30% of the natural isotopic composition of gadolinium, have extremely high thermal neutron capture cross-sections and release a cascade of gamma rays with total energy up to approximately 8 MeV following neutron capture [150]. The gadolinium neutron captures thus provide a second measurable signal that can be used to tag IBD events based on the close time coincidence of neutron and positron detection and thereby reject many background events.

The calibration of large-volume rare-event detectors is a critical step to ensure that the desired signals can be successfully distinguished from background. For Gd-doped water Cherenkov detectors, a variety of calibration source particles and energies are needed to characterize the detector response to potential IBD events, which includes the broad range of gamma-ray energies associated with Gd neutron capture. Just as coincidence detection is used to suppress background in measurements of the antineutrino IBD signal, correlated-particle radiation sources are particularly useful for antineutrino detector calibration. The ability to "time-tag" the calibration source greatly reduces the effects of background, facilitating a more accurate understanding of the detector response to the radiation of interest.

One such correlated-particle source is ^{16}N, which has been used for calibration of the

Super-Kamiokande (SK) [151] and Sudbury Neutrino Observatory (SNO) [152] neutrino detectors. ^{16}N decays by beta emission to ^{16}O, which then promptly emits a 6.1-MeV gamma ray with a branching ratio of approximately 66%. The 6.1-MeV gamma ray is useful for calibration of Gd-doped detectors due to its location near the high-energy end of the Gd neutron capture gamma-ray continuum. A simplified decay scheme for ^{16}N is shown in Fig. 5.1. ^{16}N can be produced via the ^{16}O$(n,p)^{16}$N reaction using high-energy

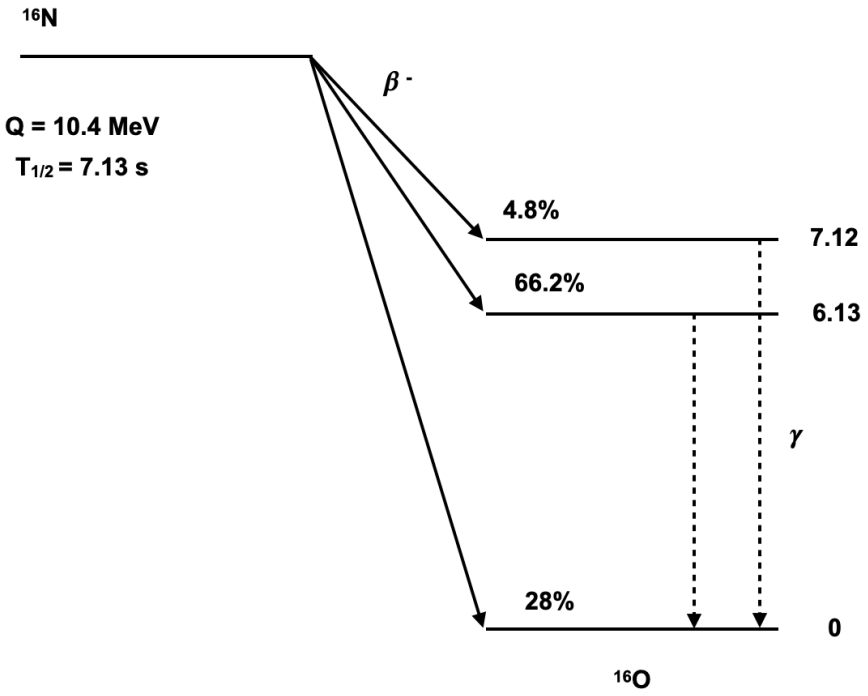

Figure 5.1: Simplified decay scheme for ^{16}N.

neutrons, such as those from a DT generator, and readily available target materials such as CO_2 or water. However, its short half-life makes it a considerable challenge to maintain the population necessary for an appreciable gamma-ray emission rate over a time period greater than a few tens of seconds. For SK, this challenge is addressed by inserting a portable DT neutron generator into the detector volume and using the water of the detector itself as the target material for ^{16}N production [151]. The neutron generator is then withdrawn, and ^{16}N decays are observed. In contrast, the SNO calibration system

utilizes a DT generator located outside the detector to produce ^{16}N in a target chamber filled with CO_2 gas, which is then transferred via an umbilical line to a second chamber inside the detector volume, where the majority of decays take place [152]. The decay volume is lined with plastic scintillator, which detects the beta particles from ^{16}N decay as a time-tag for the 6.1-MeV gamma rays. By locating the DT neutron source away from the detector volume, the active background can be sufficiently shielded to allow constant operation of the generator, and thus a constant population of ^{16}N can be maintained in the decay chamber through gas circulation. The secondary decay volume also allows the calibration source to be moved to different locations within the detector volume, which is important for determining any position-dependent variations in the detector response. The plans for calibrating the WATCHMAN detector have considered a ^{16}N system based on the design developed by the SNO Collaboration [153].

An additional feature of the SNO-type DT-neutron-generator-driven system is that other radioisotope sources can be produced by simply substituting a different target material. Specifically, by using a target material enriched in ^{17}O, ^{17}N can be produced via the ^{17}O$(n,p)^{17}$N reaction and delivered to the decay chamber using the same transfer mechanism. ^{17}N emits beta-delayed neutrons with a discrete energy spectrum ranging from approximately 380 keV to 1.7 MeV and a half-life of 4.17 s [154]. Fig. 5.2 shows a simplified decay scheme for ^{17}N. Because the ^{17}N delayed neutrons are accompanied by beta particle emission, they can be time-tagged in the same manner as ^{16}N gamma rays, making ^{17}N potentially interesting as a correlated-particle calibration source. While AmBe has typically been employed as the primary neutron calibration source for large-scale neutrino detectors [155–157], the characteristics of ^{17}N may make it attractive as an alternative or complementary source. For example, whereas AmBe neutrons are time-tagged based on detection of the coincident 4.4-MeV gamma ray emitted by ^{12}C, which requires a fairly substantial tagging detector size and mass [158], ^{17}N beta particles are

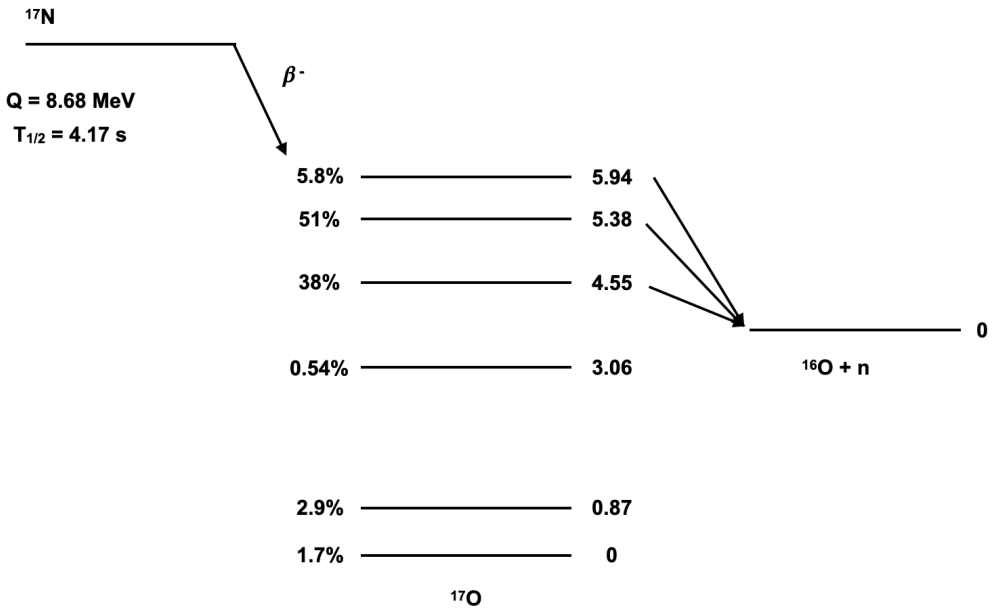

Figure 5.2: Simplified decay scheme for ^{17}N. Branching ratios are based on the data presented in Ref. [154].

relatively easy to detect with high efficiency. This allows for different source geometries and form factors which, coupled with the different tagging efficiency and neutron energy spectrum of ^{17}N, may facilitate complementary measurements of the neutron capture efficiency and light output response in a Gd-doped detector.

Previous studies by the SNO Collaboration have examined the ^{17}O$(n,p)^{17}$N reaction cross-section and ^{17}N production rate based on measurements of characteristic ^{17}N gamma rays following irradiation of ^{17}O-enriched gas with 14.1-MeV DT neutrons, and the results suggest that ^{17}N is feasible as a neutron calibration source for antineutrino detectors[159–161]. This work presents a demonstration of ^{17}N as a time-tagged calibration source based on beta particle and delayed neutron measurements. An ^{17}O-enriched water target is interrogated using a DT neutron generator, and the ^{17}N production rate and delayed neutron time profile are measured and validated against nuclear data, Monte Carlo simulations, and prior cross-section measurements. Beta-correlated delayed neutron measurements, including the beta-neutron coincidence time distribution and tagging

efficiency, are made using a specialized beta tagging detector prototype and validated with Monte Carlo simulations. The results of these measurements show that the timing information for ^{17}N delayed neutrons can be well-characterized and that a reasonable beta-tagging efficiency (45–50%) can be achieved with a rudimentary beta detection system, providing further evidence for the feasibility of ^{17}N as a calibration source for large-scale antineutrino detectors.

In addition to the investigation of ^{17}N, this chapter presents the results of preliminary tests of ^{16}N production and detector response characterization in support of the development effort for the WATCHMAN ^{16}N calibration system. ^{16}N is produced by DT neutron interrogation of water and CO_2 targets, and the light output response of large NaI(Tl) detectors to the resulting gamma-ray emission spectrum is characterized. ^{241}Am^{13}C is also explored as a potential alternative source of neutrons and 6.1-MeV gamma rays that does not require an external neutron source. Finally, the implications of potential ^{16}N, ^{17}N, and ^{241}Am^{13}C calibration sources for the detector response characterization and systematics are discussed.

5.2 Materials & Methods

5.2.1 Experimental Approach

Experimental measurements of ^{16}N and ^{17}N were performed at the University of Michigan's Neutron Science Laboratory. For the ^{16}N experiments, both CO_2 and water target object were tested. The CO_2 target was an Airgas CD FG20 tank filled with 20 lbs of CO_2 by weight and pressurized at 835 psi, while a simple 2-gallon bucket was used for the water target. While denser than the planned CO_2 gas target in the anticipated calibration system design, the chosen target objects allowed for test measurements to be performed using readily available materials in a simple configuration. An example exper-

imental configuration with the CO_2 target is shown in Fig. 5.3. A $2 \times 4 \times 16$ inch NaI(Tl)

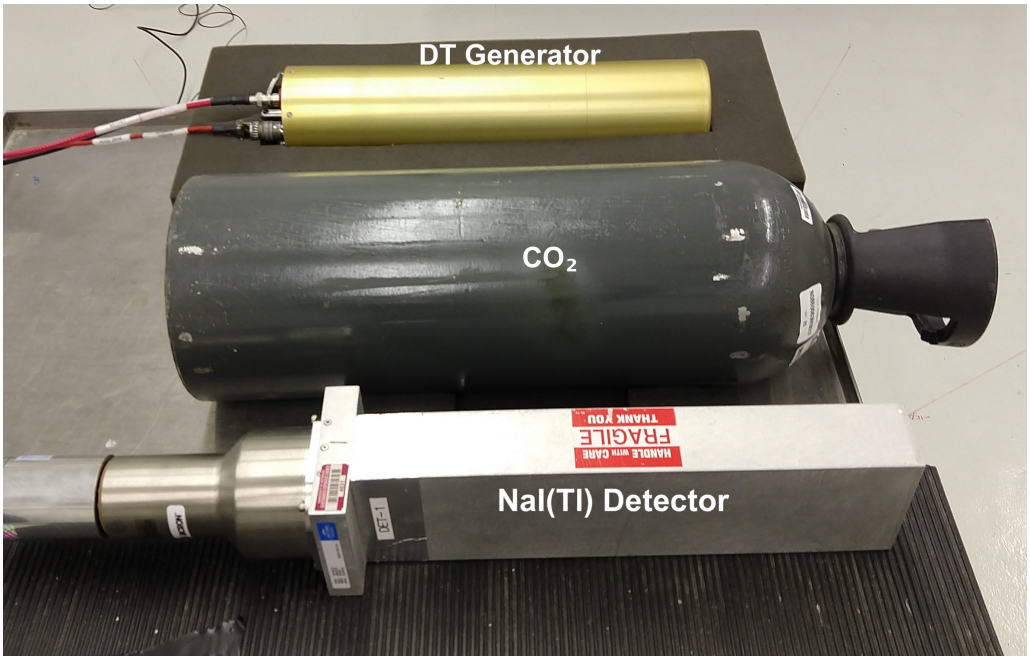

Figure 5.3: Experimental setup for ^{16}N test measurements using a CO_2 target.

detector was used to measure the gamma-ray spectrum of ^{16}N. Output pulses from the detector were digitized using a CAEN DT5730 14-bit, 500-MHz desktop waveform digitizer, and CAEN Multi-Parameter Spectroscopy Software (CoMPASS) [124] was used to acquire and store the data.

The water and CO_2 target objects were irradiated with 14.1-MeV neutrons produced by a Thermo Scientific P211 DT neutron generator. The generator was operated at a pulse rate of 100 Hz, with a pulse width of approximately 10 µs. To account for the short half-life of ^{16}N, the generator was run in a series of on/off cycles to periodically rebuild the ^{16}N population. During each cycle, the generator was turned on for 30 seconds, then off for 30 seconds. To reduce interference from active background radiation produced by the generator, ^{16}N decay events were recorded while the generator was off. The total measurement time for each target material was 20 minutes. Calibration measurements were also performed using ^{137}Cs and ^{60}Co radioisotope sources.

For the ^{17}N experiments, a 2-gram sample of ^{17}O-enriched water was used as the test object. The ^{17}O isotopic fraction of the enriched water was 60%. A custom-built BF_3 neutron detector was used to measure the delayed neutron signal from ^{17}N. The detector consists of six LND model 2035 BF_3 proportional counters connected in series, which are embedded in a rectangular block of polyethylene moderator. The BF_3 tubes are about 2 inches in diameter and are placed in cylindrical holes in the polyethylene block, which are evenly spaced radially around a central cylindrical cavity with a diameter of 11.5 cm. The moderator block is surrounded on five sides by 1-inch thick slabs of 5% borated polyethylene to reduce thermal neutron background. The polyethylene slab opposite the open side has a circular hole with a diameter of 16.5 cm. Front and back views of the BF_3 detector are provided in Fig. 5.4. The BF_3 detector output signal was passed through

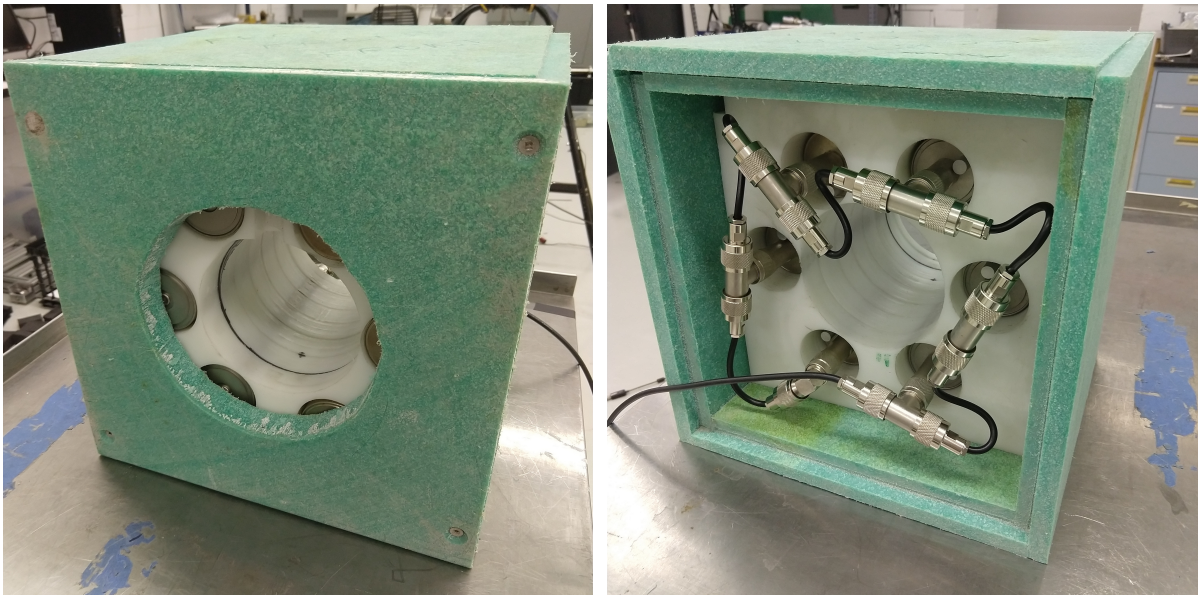

Figure 5.4: Front (left) and back (right) view of the BF_3 detector.

a Canberra model 1706 proportional counter preamplifier. The same CAEN digitizer hardware and data acquisition software used in the ^{16}N measurements were also used for ^{17}N. The ^{17}N beta signal was measured using a custom-built beta tagging detector designed to reflect the principle of operation of the decay chamber used by SNO. The

design of the beta tagging detector is described in detail in Section 5.2.2. In addition to the detector output signals, a reference signal from the DT generator was also digitized and acquired to aid in identifying the exact on and off times during operation.

During the experimental measurements, the vial of enriched water was placed inside the beta tagging detector, which was then placed in the central cavity of the BF_3 detector. The DT generator and detectors were placed such that the distance from the center of the generator target plane was approximately 15 cm from the vial of water inside the beta detector. The experimental setup is shown in Fig. 5.5. To provide a

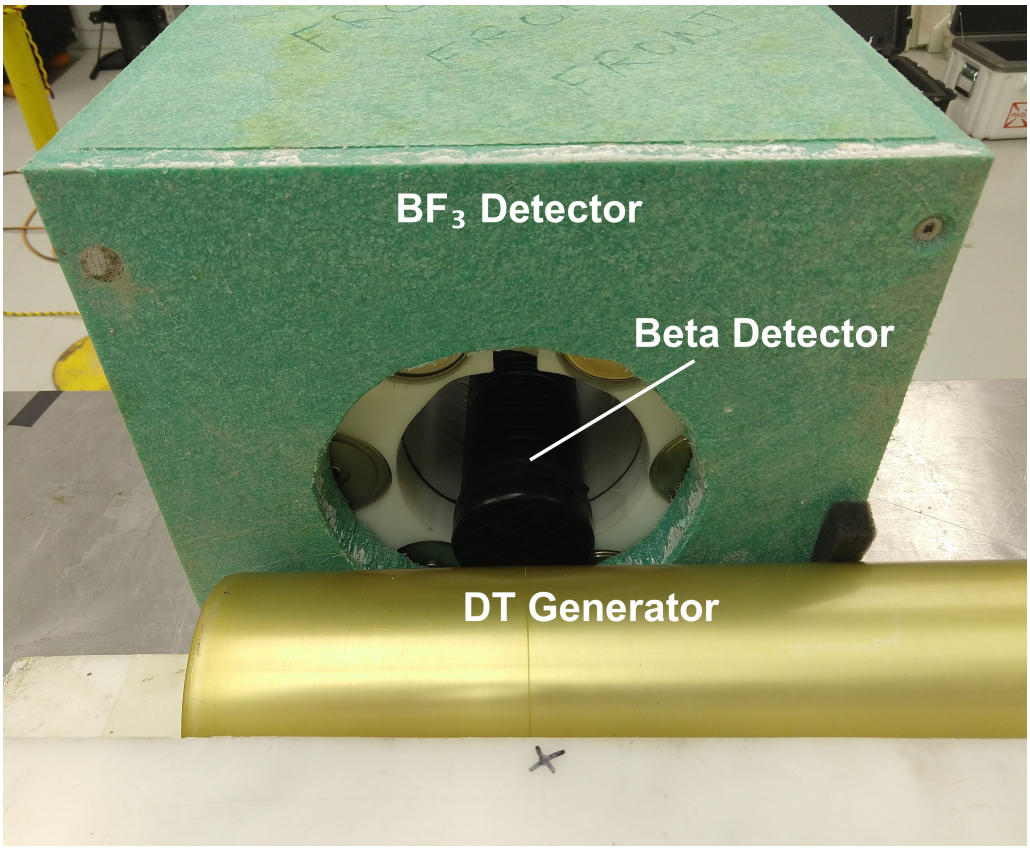

Figure 5.5: Experimental setup for ^{17}N measurements. Polyethylene blocks seen at the bottom of the photo were used to secure the generator in place.

baseline for comparison against the ^{17}N delayed neutron signal, measurements were also performed using natural water in an identical configuration. Both enriched and natural water samples were contained in 5 mL polyethylene vials. Polyethylene was chosen as the

vial material because its constituent elements produce fewer activation products relative to other standard materials, such as borosilicate glass.

As in the ^{16}N experiments, the generator was operated in a series of on/off cycles, and the ^{17}N delayed neutron signal was recorded when the generator was off. Due to the shorter half-life of ^{17}N, the generator was turned on for 10 seconds, then off for 20 seconds during each cycle. All other operational characteristics of the DT generator remained the same from the ^{16}N measurements. Five measurements of approximately 2 hours each, for a total of 10 hours, were made for each water target. To establish the background spectrum in the beta tagging detector following fast neutron activation, a pair of 2-hour measurements were also performed using an empty vial as the target object.

To provide an analogous comparison to the correlated ^{17}N data, beta-tagged gamma ray measurements were also performed using the natural water target and a pair of NaI(Tl) detectors. The vial of natural water was placed inside the beta detector, which was then placed between the two NaI(Tl) detectors. To reduce the contributions of natural and activation background, the detectors were surrounded with lead shielding. Fig. 5.6 shows the experimental configuration for the tagged ^{16}N gamma-ray measurements. The same DT generator cycling regime was used for the correlated gamma ray measurements, and the total measurement time was two hours.

Calibration measurements for the BF_3 were conducted before each 2-hour measurement using a ^{252}Cf spontaneous fission source. During all other measurements, the ^{252}Cf source was removed from the experimental area, which significantly reduced the background neutron count rate in the BF_3 detector. Aside from ^{252}Cf calibration, the gamma-ray response of the BF_3 detector was tested using ^{137}Cs, ^{22}Na, and ^{60}Co sources simultaneously. Measurements of background were also recorded. In addition to the test measurements described in Section 5.2.2, the beta tagging detector was also calibrated before each generator run using a ^{137}Cs source.

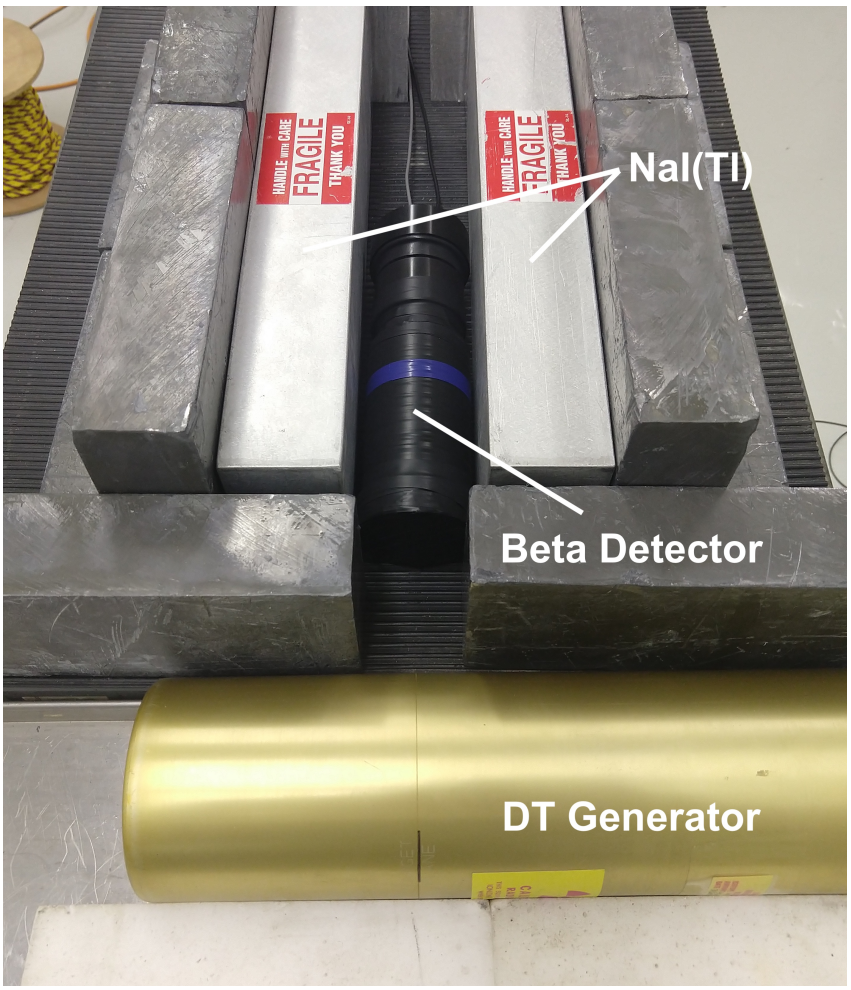

Figure 5.6: Experimental setup for tagged ^{16}N gamma ray measurements. Not pictured: an additional plate of lead shielding was placed over the top of the NaI(Tl) and beta detectors.

5.2.2 Beta Tagging Detector Development

To record beta emission by ^{16}N and ^{17}N and provide the time-tag for correlated-particle measurements, a specialized beta detector prototype was constructed. The beta detector design is based on the decay chamber used by the SNO Collaboration for ^{16}N calibration [152], which is also the basis for the planned calibration system for a large antineutrino detector. The main requirement for the beta detector prototype is to provide good detection efficiency for beta particles with energy of a few MeV while suppressing

background contributions as much as possible. Because enriched water target is placed inside the detector, thus subjecting the detector to a high fast neutron flux from the DT generator, the detector materials must be resilient to activation in order to minimize the contribution of background betas and gamma rays. Materials containing oxygen are a particular concern in ^{17}N measurements, as the beta particles from ^{16}N decay are similar in energy to those emitted by ^{17}N, and a large contribution from ^{16}N produced in the detector structure would significantly degrade the signal-to-noise ratio. By using plastic scintillator with small thicknesses (a few mm), significant energy deposition by ^{16}N or ^{17}N beta particles can be achieved while presenting a short path length, and thus a low interaction probability, for background gamma rays. Monte Carlo simulations were performed using Geant4 to predict the detector response to ^{16}N and ^{17}N beta particles and validate the detector design prior to construction. Fig. 5.7 shows the simulated initial energy spectra of ^{16}N and ^{17}N beta particles, as well as their simulated energy deposition in a 3 mm EJ-212 plastic scintillator. To account for energy losses by the beta particles

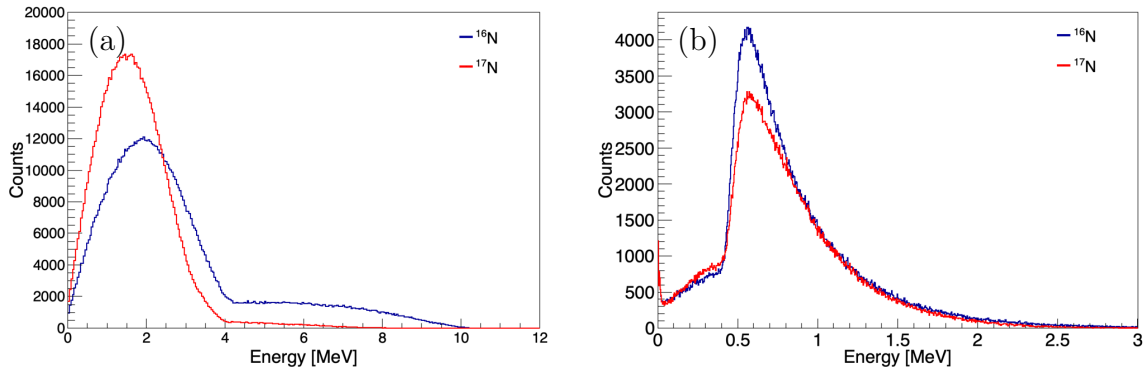

Figure 5.7: Simulations of the (a) initial energy and (b) energy deposition in a 3 mm EJ-212 plastic scintillator following escape from a 2-gram vial of water for ^{16}N and ^{17}N beta particles.

as they exit the water target where they are produced, the simulated beta particles are generated uniformly within a 2-gram volume of water inside a polyethylene vial with same dimensions as the experimental target objects. As a result, the average energies of

the escaping ^{16}N and ^{17}N beta particles are between approximately 1 and 1.5 MeV, somewhat lower than the average initial energies indicated in Fig. 5.7a. As Fig. 5.7b shows, the energy deposition for each isotope is peaked near 600 keV, which should generate a readily detectable light output signal in the scintillator.

The beta detector consists of five panels of Eljen EJ-212 plastic scintillator arranged to form a rectangular hollow chamber with dimensions of 31.5 × 31.5 × 67 mm. Four rectangular panels with dimensions of 31.5 × 70 × 3 mm form the sides of the detector, with a square 31.5 × 31.5 × 3 mm panel used as the base of the enclosure. The sixth side is left open to allow sources and target objects to be freely placed inside the detector volume. The scintillators are held in place by a support structure, which is 3D-printed from oxygen-free acrylonitrile butadiene styrene (ABS) resin to reduce interference from activation produced during neutron irradiation. The housing structure also includes a removable cap, which allows a light-tight environment to be maintained inside the detector when closed. Figure 5.8 shows a schematic of the beta detector design, as well as a photograph of the assembled detector. A Hamamatsu R6231 photomultiplier tube

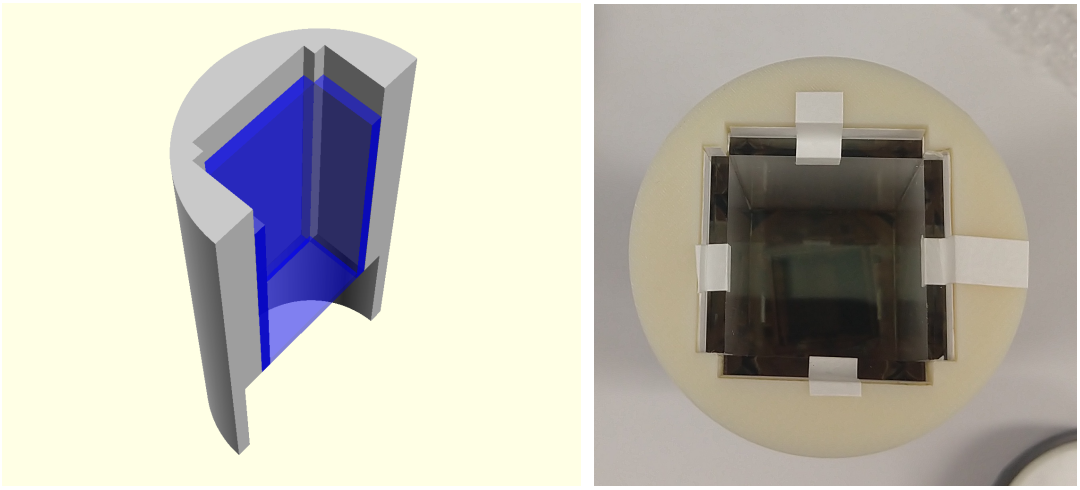

Figure 5.8: *Left:* Cutaway schematic of the beta tagging detector housing and scintillators. *Right:* Photo of the fully assembled detector with the end cap removed.

was used to detect the scintillation light. A circular socket was included in the detector

support structure (shown in Fig. 5.8) to facilitate coupling to the square scintillator panel and edges of the side panels, as well as to maintain light-tightness at the detector-photomultiplier interface. To improve light collection, reflective Tyvek paper was placed between the scintillator panels and the support structure walls. Because the ABS housing material is slightly translucent, all outer surfaces of the detector were wrapped with electrical tape to provide an additional light seal. After construction, the beta tagging detector response was tested using ^{90}Sr and ^{204}Tl check sources. While the beta tagging detector is not designed for high-resolution measurements of beta energy, basic energy calibration was performed using a ^{137}Cs source.

5.3 Results & Discussion

5.3.1 Beta Tagging Detector Response

Due to its geometry, the beta tagging detector light output response is somewhat idiosyncratic, and a few systematic factors must be taken into account. For example, the light transport is likely to exhibit some position dependence and is highly sensitive to attenuation by opaque sources or other objects objects inside the detector chamber. To illustrate this point, Fig. 5.9a shows a comparison of the measured light output spectrum for a ^{137}Cs calibration source with and without the enriched water vial inside the detector. The vial itself is translucent, but is covered with an opaque label. This causes some attenuation of the scintillation light, which shifts the ^{137}Cs Compton edge to a lower light output. As a result, measurements must be performed under similar light transport conditions if any comparisons are to be made, such as taking a residual energy spectrum. To address this issue, opaque stickers were placed over the natural water and empty vial test objects to create a light transport profile similar to that of the enriched water target. A comparison of the resulting ^{137}Cs light output spectrum for each test object is shown in

Fig. 5.9b. While there is still some variation, the addition of the opaque stickers signifi-

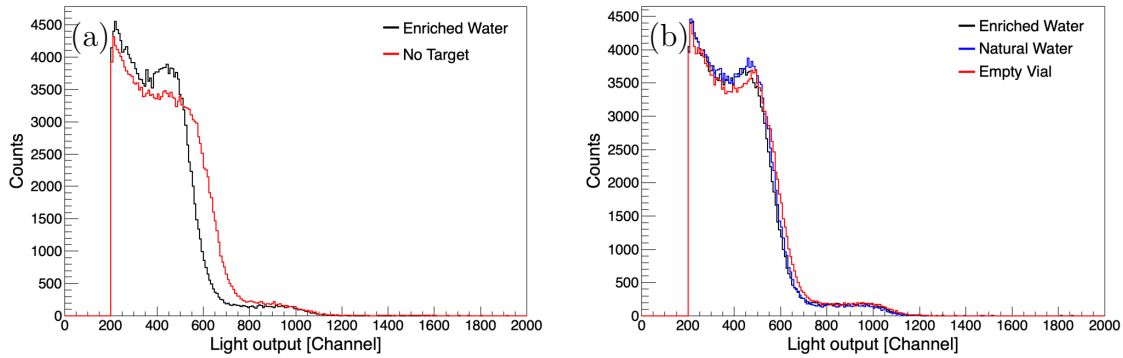

Figure 5.9: (a) Comparison of ^{137}Cs light output spectrum for the enriched water target and no target in the beta detector. (b) Comparison of ^{137}Cs light output spectrum for enriched water, natural water, and empty vial targets with opaque stickers added for more consistent light transport.

cantly improves the agreement between each spectrum, such that a reasonably consistent energy measurement can be made.

Fig. 5.10 shows the calibrated light output spectra for ^{90}Sr and ^{204}Tl check sources in the beta detector. The general shape of each spectrum conforms with expectation for each

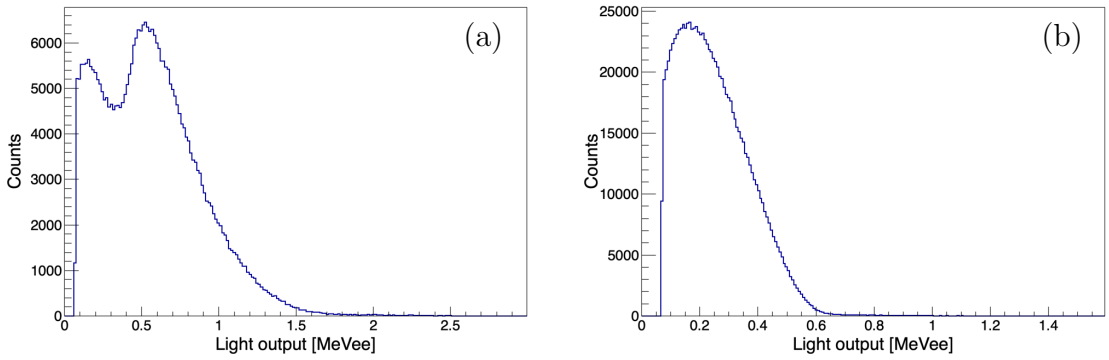

Figure 5.10: Light output spectra for (a) ^{90}Sr and (b) ^{204}Tl check sources in the beta detector.

source, although the high-energy tail appears somewhat suppressed, especially for ^{90}Sr. This is likely due to incomplete energy deposition by higher-energy beta particles as they

pass through the thin layer of plastic scintillator, which is consistent with the simulated energy deposition by ^{16}N and ^{17}N beta particles shown in Fig. 5.7b. Calculations of the absolute beta detection efficiency are complicated by the fact that the beta particle flux is heavily influenced by attenuation within the source housing. Based on Geant4 simulations, small changes in the geometry of the plexiglass container on the order of a few tenths of mm can significantly reduce the flux, with as little as 15–20% of the emitted betas escaping the source container. However, the estimates for intrinsic efficiency are more encouraging, with simulated results showing 88% and 92% intrinsic efficiency with a detection threshold of 75 keV for ^{204}Tl and ^{90}Sr, respectively. Even if the intrinsic efficiency is reduced somewhat due to light transport, it is still sufficient to provide a reliable tagging pulse.

5.3.2 ^{16}N Results

Fig. 5.11 shows the light output spectrum for ^{16}N in the NaI(Tl) detector, which was measured by recording the cumulative spectrum from each 30-second generator off cycle during interrogation of the CO_2 target object. A clear photopeak, as well as single- and double-escape peaks, are observed in the detector response, corresponding to 6.1-MeV gamma rays from ^{16}N. An additional photopeak can be seen near 7 MeV, which is associated with a lower-probability decay branch of ^{16}N. Monte Carlo simulations were performed using Geant4 to model the response of the NaI(Tl) detector to 6.1-MeV gamma rays and validate the experimental measurement. The simulated light output response is also shown in Fig. 5.11, and shows good agreement with the experimental results between about 5 and 6.5 MeVee. The deviations from the experimental result at higher and lower energies appear because the simulation only considers the response to 6.1-MeV gamma rays.

In addition to the light output spectrum, the time profile of ^{16}N gamma rays was also

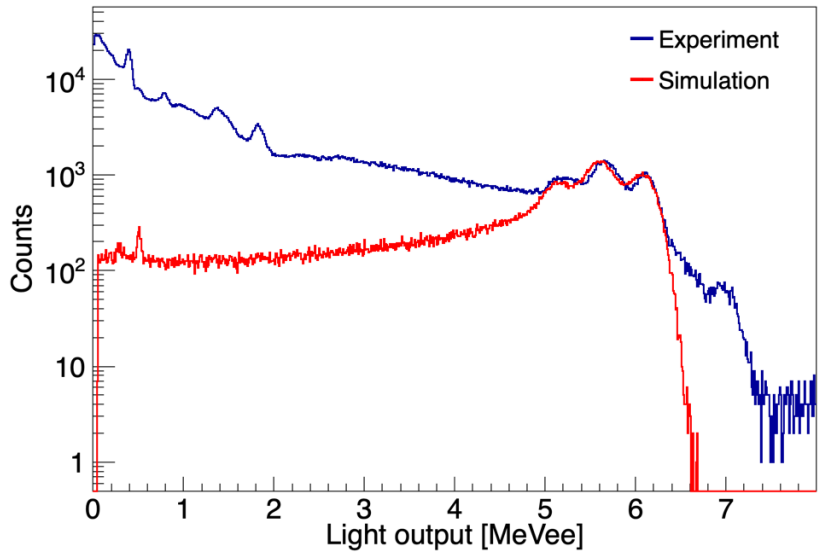

Figure 5.11: Comparison of the measured and simulated light output spectrum for ^{16}N in a large NaI(Tl) detector. Disagreement outside of the 5–6 MeV range is due to the fact that the simulation did not include activation gamma rays or other decay branches for ^{16}N other than the 6.1-MeV gamma ray.

examined. Fig. 5.12 shows the cumulative time distribution of NaI(Tl) detector pulses between 5 and 6.5 MeVee taken while the neutron generator was turned off. The data show good agreement with a simple exponential model based on the known decay time constant for ^{16}N. The only fitting parameters used in the model include a scaling constant and a constant additive term to account for background.

Although ^{16}N has already been developed and successfully employed as an antineutrino detector calibration source, the exact system used by the WATCHMAN Collaboration is likely to be somewhat different from the SNO design. For this reason, a good understanding of the NaI(Tl) detector response to ^{16}N gamma rays is useful to the large antineutrino detector calibration system development effort, as the large NaI(Tl) detectors will likely be used to measure the ^{16}N production of the calibration system prototypes.

Correlated ^{16}N measurements were also performed using the beta tagging detector and a pair of large NaI(Tl) detectors to provide a point of comparison for the correlated

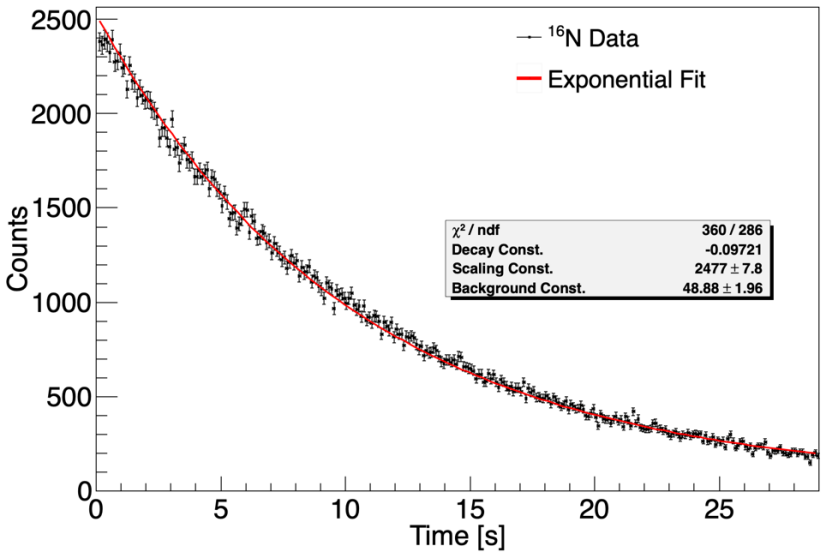

Figure 5.12: Caption

^{17}N measurements presented in Section 5.3.4. Fig. 5.13 shows a comparison of the light output spectra for the natural water and empty vial test objects for both uncorrelated and beta-correlated measurements. Despite the presence of a significant amount of lead shielding, the gamma-ray signature for the 2-gram natural water target proved difficult to isolate. This is due in large part to the fact that the DT generator readily produces ^{16}N in the surrounding air, leading to a significant activation background at 6.1 MeV. Since the water target inside the beta tagging detector is small, relatively little ^{16}N is produced, and the signal is overwhelmed. As a result, the uncorrelated light output spectra for the natural water target and the empty vial are nearly identical, as Fig. 5.13a shows. Even when the beta-coincidence is enforced, there is still little difference between the spectra for each target object. As Fig. 5.13b shows, there may be a slight difference in the 5–6.5 MeVee light output region corresponding to ^{16}N gamma rays. However, due to the high rate of chance coincidences from activation background, it is difficult to draw any conclusions with confidence. It may be possible to resolve the contribution of tagged ^{16}N gamma rays in such an environment, but extracting the signal would require either

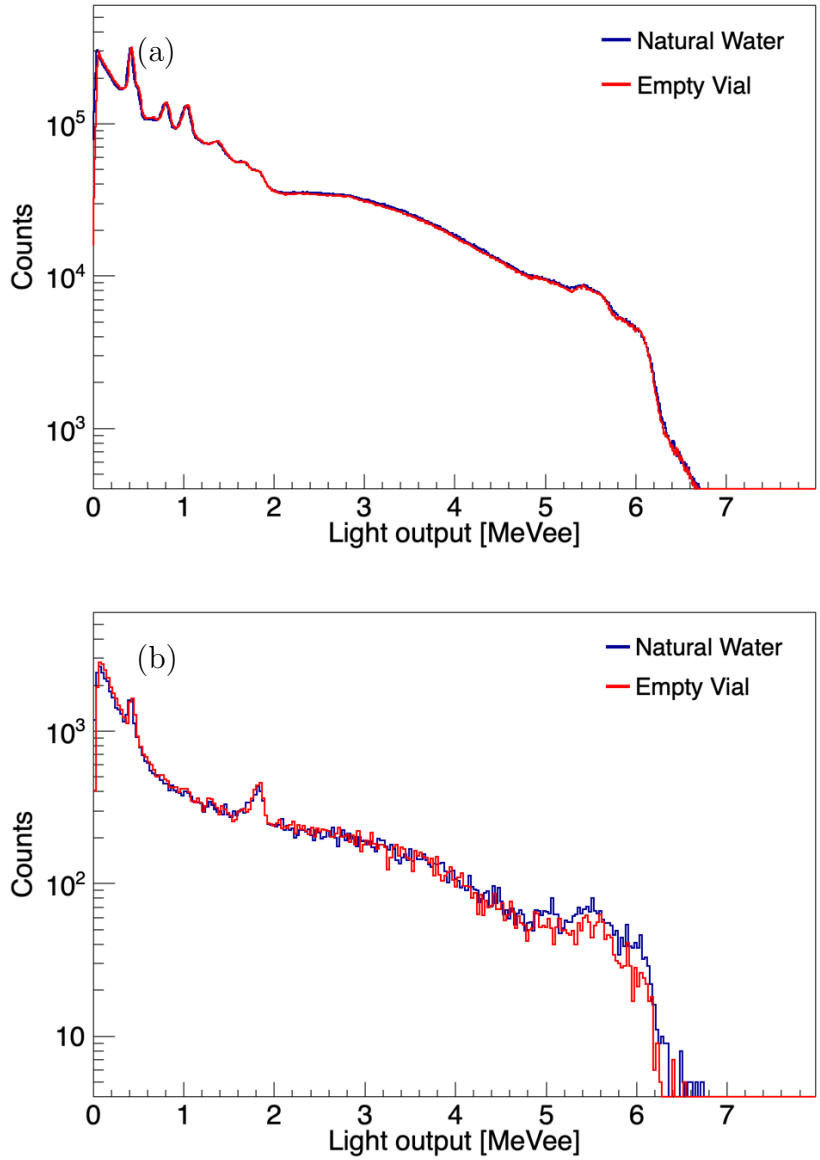

Figure 5.13: Comparison of the (a) uncorrelated and (b) beta-correlated light output spectra in the NaI(Tl) detector for natural water and empty vial targets following irradiation with the DT generator.

very long measurement times or a redesign of the experimental approach (such as the inclusion of a mechanical transfer system to remove the ^{16}N sample from the surrounding activated materials), which are beyond the scope of this dissertation.

5.3.3 $^{241}Am^{13}C$ as an Alternative Source of High-Energy Gamma Rays

One of the difficulties associated with ^{16}N as a calibration source is the need for a high-energy external neutron source to drive the radioisotope production. DT neutron generators are expensive and require a number of factors to be taken into account, such as shielding, location, and operator safety, before they can be installed in a laboratory facility. As a lower-cost alternative, $^{241}Am^{13}C$ may provide a source of 6.1-MeV gamma rays without the need for an external neutron source. Furthermore, the long half-life of ^{241}Am would allow for a constant source activity without the need for type of circulation system required to maintain the ^{16}N population.

$^{241}Am^{13}C$ primarily emits neutrons via the $^{13}C(\alpha,n)^{16}O$ reaction. However, at higher alpha energies, branching to the 6.1-MeV excited state of ^{16}O becomes possible, which results in the emission of the same 6.1-MeV gamma ray associated with ^{16}N decay. Specifically, above an alpha energy threshold of $E_\alpha \approx 5.05$ MeV, the branching ratio to the 6.1-MeV state of ^{16}O increases sharply, with values of approximately 0.3 at $E_\alpha = 5.48$ MeV (the most common energy for ^{241}Am alpha emission) and 0.45 at $E_\alpha = 6$ MeV[162]. Given these branching ratios, a significant fraction of the (α,n) reactions will lead to gamma-ray emission, provided that the incident alpha particles are restricted to the high energy range. Because the gamma rays will always be accompanied by neutron emission, $^{241}Am^{13}C$ may be useful as a time-correlated neutron-gamma source, as well as an alternative source of 6.1-MeV gamma rays.

While $^{241}Am^{13}C$ has previously been used as a neutron calibration source for neutrino detectors [163] and liquid argon detectors for dark matter search [164], its potential as a source of time-correlated neutrons and gamma rays has not been fully exploited. In fact, for the Daya Bay Neutrino Experiment, gamma-ray emission was actively suppressed by surrounding the ^{241}Am source with a gold foil to reduce the energy of the emitted alphas

before they reached the ^{13} target[163]. As a proposed alternative to ^{16}N, however, the goal of the ^{241}Am^{13}C source design would be to maximize the gamma-ray emission rate relative to the neutron rate, thereby increasing the proportion of coincident neutron-gamma events. Toward this end, an ideal source geometry would feature very thin layers of ^{241}Am and ^{13}C to minimize energy loss by the alpha particles prior to the (α,n) reaction. There are many ways to accomplish this, but one potential design involves depositing the thin layer of ^{241}Am on a substrate via electroplating. This method would allow the layer thickness to be controlled by the substrate area and the amount of ^{241}Am. For example, a thickness of about 100 nm could be achieved with a 0.3 mg ^{241}Am sample (approximately 1 mCi activity) deposited over an area of 2 cm^2.

While the ^{241}Am layer should be as thin as possible, the ^{13}C layer thickness must balance alpha particle energy loss against the overall (α,n) reaction rate. According to the NIST ASTAR database, the stopping power for an alpha particle in graphite is about 163 keV/µm at 5.5 MeV [165]. Based on interpolation of the ASTAR data, a 5.5-MeV alpha particle would travel between 2 and 2.5 µm before falling below the energy threshold for production the 6.1-MeV excited state of ^{16}O. Any additional thickness beyond 2.5 µm would not contribute to gamma-ray production. The ^{13}C$(\alpha,n)^{16}$O reaction cross-section is fairly consistent between $E_\alpha = 5$ and 5.5 MeV, varying by $\pm$ 20 mb around an average of 150 mb [166]. This means that the (α,n) reaction rate will be roughly proportional to the ^{13}C layer thickness, with a thickness of 2.5 µm providing the maximum total gamma-ray production. However, in terms of the proportion of coincident neutron-gamma events, the optimal ^{13}C layer thickness would likely be somewhat less than 2.5 µm. This is because the decrease in the 6.1-MeV ^{16}O excited state branching ratio with decreasing alpha energy leads to a diminishing marginal increase per unit thickness added. A 1–2 µm ^{13}C layer could be achieved by depositing a thin layer of ^{13}C (such as multiple layers of graphene) on a copper substrate, which would serve as an absorber for the alpha

particles after they pass through the layer. A simple sketch of the potential ^{241}Am^{13}C source geometry is shown in Fig. 5.14. Copper is chosen as the substrate material over

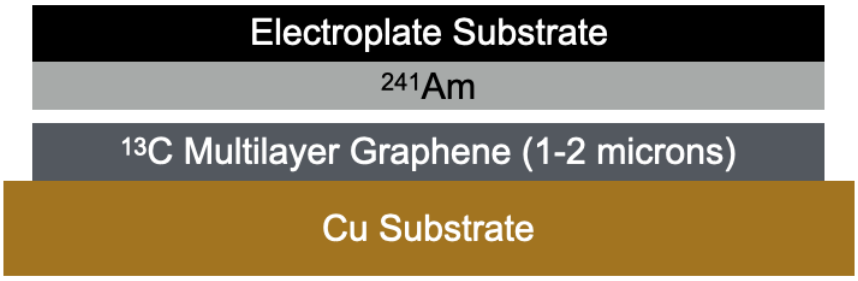

Figure 5.14: Sketch of a potential ^{241}Am^{13}C source geometry.

other commonly used alternatives (such as silicon) due to the low (α,n) cross-sections of ^{63}Cu and ^{65}Cu below 5 MeV.

Based on Monte Carlo simulations performed using Geant4, the estimated rate of ^{13}C(α,n)^{16}O reactions is 175 $\pm$ 6 s^{-1}, assuming 1 mCi ^{241}Am source activity, ^{13}C layer thickness of 2 µm, and 50% solid angle coverage for the ^{241}Am source as depicted in Fig. 5.14. Assuming an average branching ratio of 0.25 to the 6.1-MeV excited state of ^{16}O, the estimated rate of 6.1-MeV gamma rays is 43.7 $\pm$ 1.4 s^{-1}. While the rate of gamma-ray emission is relatively low, background radiation rates are also typically very low above a few MeV, especially in underground antineutrino detectors, which typically have a significant overburden. The emission of a coincident neutron will also significantly aid the isolation of the ^{241}Am^{13}C signal, making it a feasible source of 6.1-MeV gamma rays for large-scale antineutrino detector calibration. Apart from ^{241}Am, other alpha emitters with even higher energy, such as ^{244}Cm or ^{238}Pu, could potentially provide a higher 6.1-MeV gamma-ray production rate. The higher specific activity of ^{244}Cm and ^{238}Pu would also allow a smaller amount of material to be used, which could allow for a thinner layer of alpha-emitting material to further reduce energy losses.

5.3.4 ^{17}N Results

The ^{17}N delayed neutron time profile was measured by recording neutron captures in the BF_3 detector after the generator was turned off. The time the generator was turned off was determined from the reference signal, and a veto window of 10 ms was applied to account for neutron die-away. Following the veto window, a 15-second collection window was opened, during which delayed neutron events were recorded. For both uncorrelated and beta-correlated measurements, the delayed neutron profile for the natural water target was subtracted from the profile for the enriched water target, yielding the residual ^{17}N delayed neutron profile. The coincidence window for beta-correlated events was defined as $-80 < t_c < 400$ µs, where t_c is the coincidence time between a detected beta particle and the subsequent neutron capture in the BF_3 detector. Fig. 5.15 shows the uncorrelated and beta-correlated residual ^{17}N delayed neutron time profiles measured in the BF_3 detector. In each case, the data were fitted with a simple exponential using the known decay time constant, $\lambda = 0.1661$, for ^{17}N. The measured delayed neutron decay time profiles showed good agreement with the exponential model with reduced χ^2 values of 25.11/29 and 37.16/29 for the uncorrelated and beta-correlated cases, respectively. The error and overall variability observed in the beta-correlated residual time profile are likely increased due to the lower delayed neutron counting statistics for the natural water target when beta-coincidence is enforced.

While the shape of the delayed neutron time profile provides confirmation of ^{17}N production, the feasibility of ^{17}N as a calibration source is dependent upon the ability to produce sufficient quantities and a solid understanding of the population dynamics within the calibration system. To determine the absolute neutron detection efficiency of the BF_3 detector, a ^{252}Cf spontaneous fission source with known activity was placed inside the detector cavity at approximately the same location as the enriched water target during the ^{17}N experiments. Based on the observed neutron count rate, the absolute efficiency

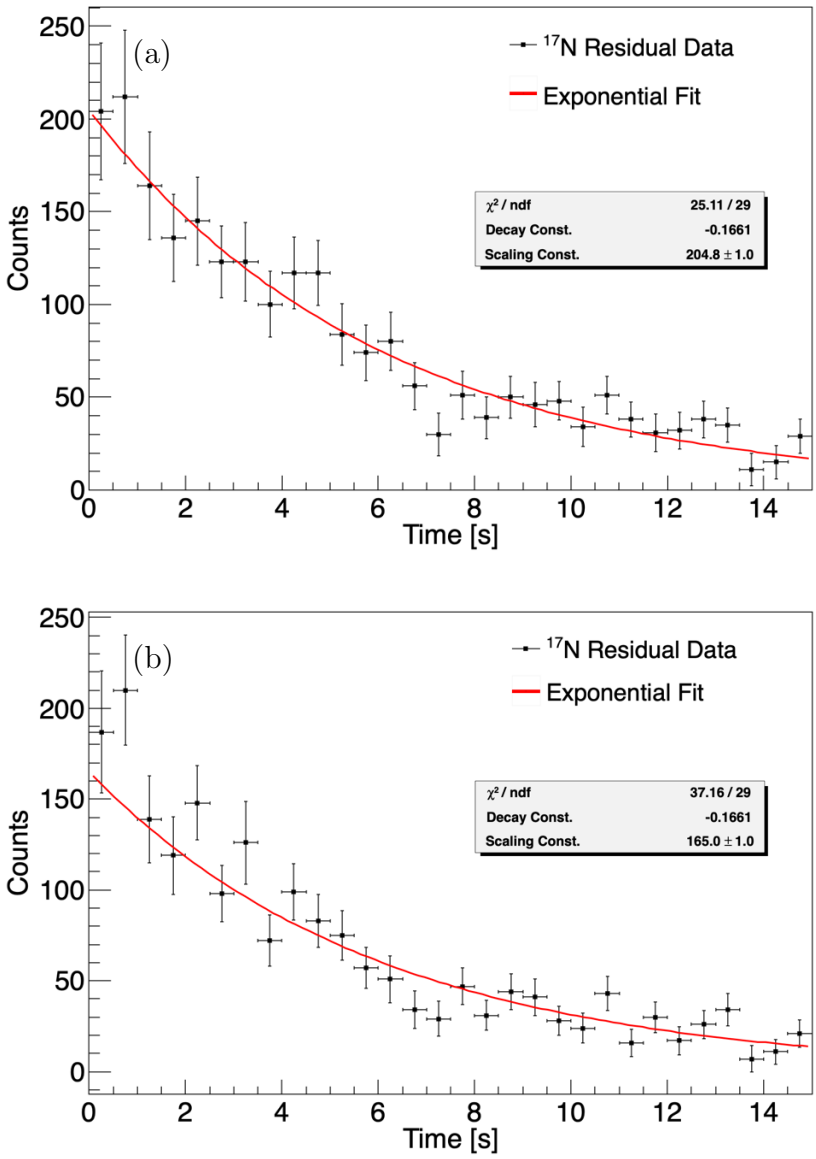

Figure 5.15: (a) Uncorrelated and (b) beta-correlated ^{17}N delayed neutron time profiles measured in the BF_3 detector. Simple exponential fits using the known decay time constant for ^{17}N are overlaid.

was determined to be 1.1% for ^{252}Cf fission neutrons. However, due to the lower average energy of ^{17}N delayed neutrons, the detection efficiency is expected to be slightly higher than for ^{252}Cf. Geant4 simulations were performed to estimate the difference in the BF_3

detector intrinsic efficiency for the ^{252}Cf and ^{17}N energy spectra. The simulation results showed that the efficiency for ^{17}N is expected to be about 15% higher than for ^{252}Cf. Applying this to the absolute efficiency measured using ^{252}Cf, the estimated absolute detection efficiency for ^{17}N delayed neutrons is 1.27%.

To calculate the experimental production rate of ^{17}N, the uncorrelated delayed neutron residual was used to determine the average number of delayed neutrons detected per generator on/off cycle. During each 15-second delayed neutron window, an average of 1.93±0.06 delayed neutrons were detected. Given the 4.17-s half-life of ^{17}N, approximately 92% of the initial ^{17}N population is expected to decay within the 15-second window after the generator is turned off. Assuming an absolute detection efficiency of 1.27%, a total branching ratio of about 95% for delayed neutron emission, and that 92% of decays take place within the 15-second measurement window, the estimated ^{17}N population in the enriched water target following a 10-second irradiation is 173.9 ± 5.4.

Geant4 simulations of the experimental configuration were performed to validate the measured production rate. Assuming a 4π generator flux of 10^8 neutrons/s, the simulated ^{17}N production rate in the enriched water target is 15.2 ± 0.55 nuclei per second. For a constant production rate, the ^{17}N population at time t is given by

$$N(t) = N_o e^{-\lambda t} + \frac{Q_o}{\lambda}\left(1 - e^{-\lambda t}\right), \tag{5.2}$$

where Q_o is the constant production rate, and λ is the decay constant of ^{17}N. Using the simulated production rate over an irradiation time of 10 seconds, the simulated population determined by Eq. (5.2) is 74.1 ± 2.7. While this result appears to be in disagreement with the experimentally measured production, the simulated rate strongly depends on the reaction cross-section used by the model, and there are substantial differences in the ^{17}O(n,p)^{17}N cross-section across different references. For example, Geant4 utilizes the JEFF-3.3 library, which specifies a cross-section of about 11.5 mb [167]. In contrast, pre-

vious experiments by Norman and Sur measured the cross-section to be 27.4±6.1 mb [161], and cross-sections as high as 40 mb can be found in other reference libraries [168, 169].

Because the reaction rate is nearly proportional to the cross-section, the change in the simulated production rate can be easily estimated for a given proportional change in the cross-section. If a cross-section of 27.4 mb is assumed, the expected production rate in simulation increases to 176.6 ± 6.4 nuclei per 10-second irradiation, which agrees closely with the experimental result. In fact, the difference between the measured ^{17}N production and the Geant4 simulation implies a cross-section of approximately 27 mb in the experimental measurement, which is consistent with the results obtained previously by Norman and Sur. Table 5.1 provides a summary of the measured and simulated ^{17}N production rates and their associated estimated cross-sections. While the statistical error

Table 5.1: Summary of measured and simulated ^{17}N production rates. The production rates listed are the population of ^{17}N nuclei following a 10-second irradiation with the DT generator. The adjusted simulation results specify the expected production for the same simulated flux rate assuming a reaction cross-section of 27.4 mb.

	Experiment	Simulation	Adjusted Simulation
Production Rate	173.9 ± 5.4	74.1 ± 2.7	176.6 ± 6.4
Estimated Cross-Section (mb)	27.0	11.5	27.4

associated with the ^{17}N population measurement is about 3%, other sources of potential systematic error must be considered in the reaction cross-section estimate. For example, there is likely some deviation in the overall neutron flux from the nominal 10^8 neutrons/s produced by the DT generator. Furthermore, the simulated flux over the target object volume and the absolute efficiency of the BF_3 detector are both sensitive to the assumptions made about the experimental geometry. These sources of error are too variable to quantify with the precision needed to claim a measurement of the cross-section based on the experimental results. However, even if a relative error as large as 15–20% were assumed, the estimated cross-section remains consistent with the previous measurement,

which is encouraging. It also implies that the accuracy of Geant4 simulations could be improved by incorporating a larger cross-section for $^{17}O(n,p)^{17}N$ than the value currently included from the JEFF-3.3 library.

Although the demonstrated ^{17}N production rate is modest, the amount of target material available was small, and larger production systems may be able to achieve higher rates to more easily facilitate the use of ^{17}N for calibration. The 2-gram enriched water target used for the present experiments contains approximately 1.07 g of ^{17}O. For comparison, a 678 cm^3 target reservoir of 60% enriched CO_2 gas at 6.5 atm and 300 K, such as the one used by SNO [152], would contain approximately 8.1 g of ^{17}O. In a favorable geometry, a much higher neutron flux could be achieved over the target mass, and it is reasonable to assume that ^{17}N production rates could be increased by at least one order of magnitude over the rates observed here. These results provide further evidence that ^{17}N can be produced in sufficient quantities to be feasible as a calibration source.

To demonstrate the utility of ^{17}N as a correlated-particle source, its beta-tagging and timing characteristics were also investigated. Since the beta energy spectra for ^{16}N and ^{17}N overlap significantly, it is not possible to discriminate between the two isotopes based on beta energy alone. However, the higher energy of ^{16}N and ^{17}N beta particles makes it possible to separate them from lower-energy background or activation sources. To isolate the ^{17}N beta signature, a residual beta energy spectrum was taken by subtracting the energy spectrum measured with an empty vial as the target object in the beta tagging detector from the spectrum measured with the enriched water target in place. The resulting ^{17}N residual beta energy spectrum is shown in Fig. 5.16 with the simulated ^{17}N beta energy deposition from Fig. 5.7b overlaid for comparison. The residual energy spectrum shows some features, which which may be due to the inconsistencies in light transport and the difficulty in calibrating the beta detector for different target objects, as discussed in Section 5.3.1. However, it is generally consistent with the expected response

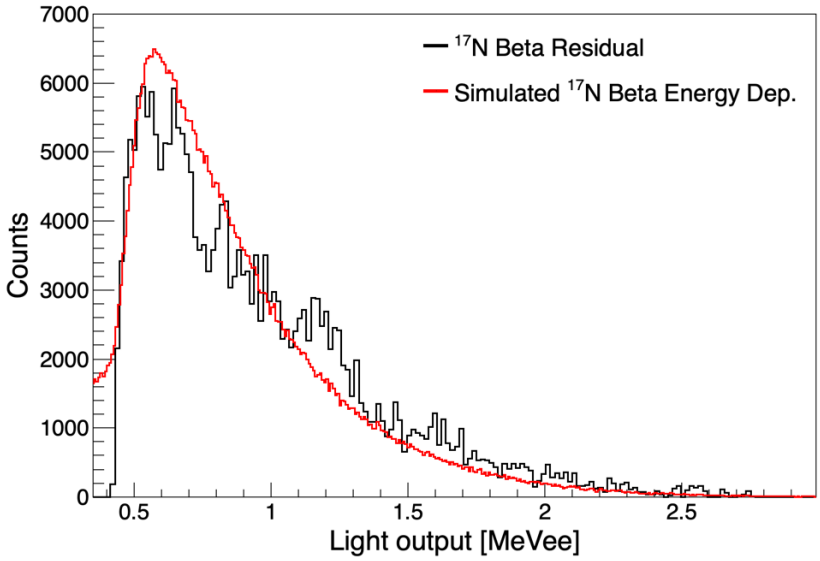

Figure 5.16: Comparison of the measured ^{17}N residual beta energy spectrum and simulated ^{17}N beta energy deposition in the beta tagging detector.

based on simulation, which provides some evidence that the detected events are most likely ^{17}N betas.

Having isolated the ^{17}N beta and neutron signals, their timing relationship was subsequently examined. Fig. 5.17 shows the measured beta-neutron coincidence time distribution, which is compared against a Geant4 simulation of the time-to-capture distribution for ^{17}N neutrons in the experimental detector configuration. In the measured coincidence time distribution, an estimated constant accidental rate of about 6 counts per 10-µs bin has been subtracted to allow for direct comparison with the simulated result, which is background-free. The experimental data show good agreement with the shape predicted by simulation. In the simulation, 95% of captures take place within 250 µs of emission, and 99% take place within 300 µs. The experimental distribution is subject to much more statistical fluctuation, but still agrees well with the simulated benchmarks, with about $92 \pm 6\%$ of neutron captures occurring within 250 µs of beta detection, and $96^{+4}_{-6}\%$ occurring within 300 µs. The close agreement between the measured and simulated time

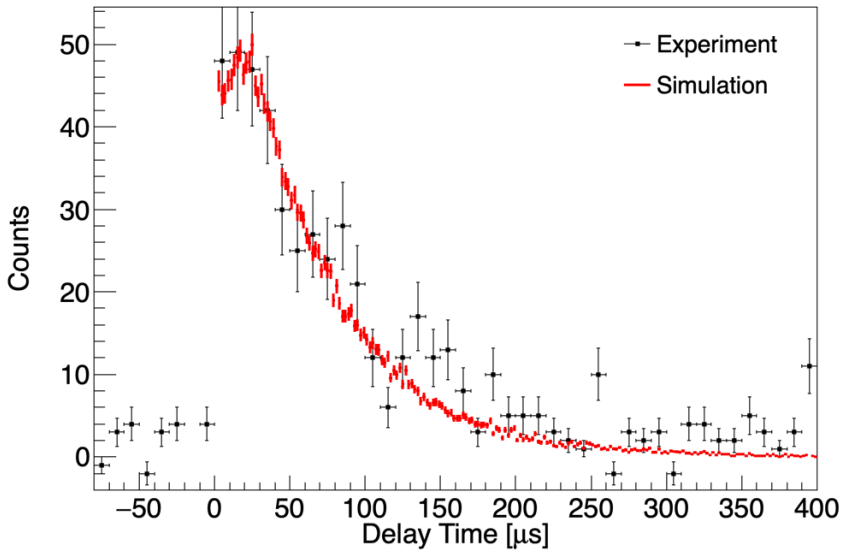

Figure 5.17: Comparison of the measured beta-neutron coincidence time distribution and simulated time-to-capture distribution for ^{17}N neutrons in the experimental configuration.

distributions provides a strong confirmation that true beta-tagged ^{17}N delayed neutron events have been recorded.

Furthermore, by taking the energy information of detected beta particles into account, the overall tagging performance can be improved. Based on the ^{17}N residual beta energy spectrum in Fig. 5.16, a threshold of 435 keV was applied to detected pulses in the tagging detector with the goal of reducing contributions to the accidental rate from background or activation radiation. Fig. 5.18 shows a comparison of the beta-neutron coincidence time distribution with and without the 435 keV threshold applied to beta events. The improvement in the signal-to-background ratio, $R_{S/B}$ was quantified by comparing the coincidence peak integral to the number of accidental events over the same time period using the expression

$$R_{S/B} = \frac{\int_{t=0\,\mu s}^{t=250\,\mu s} (D(t) - B)\, dt}{\int_{t=0\,\mu s}^{t=250\,\mu s} B\, dt}, \tag{5.3}$$

where $D(t)$ is the coincidence distribution at time t and B is the accidental background rate determined from the average counts per bin from -80 to 0 μs. When all beta events

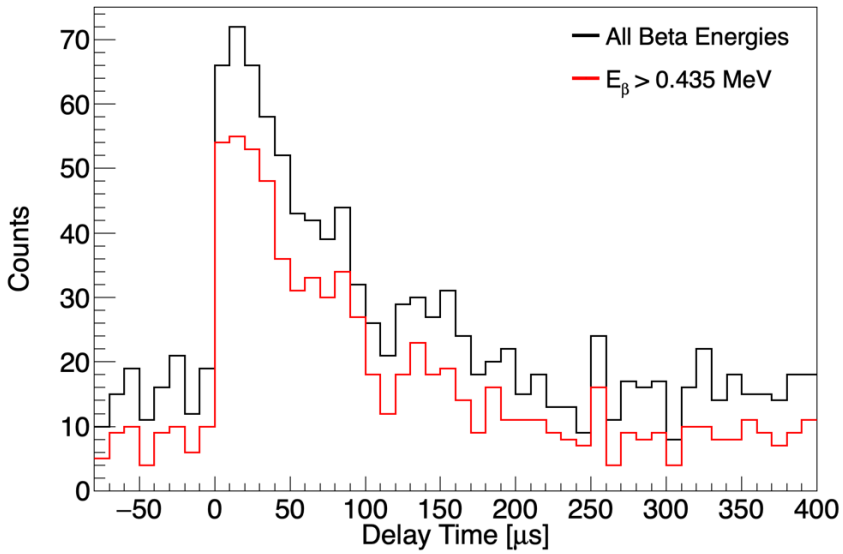

Figure 5.18: Comparison of the beta-neutron coincidence time distribution for ^{17}N with and without a 435 keV beta energy threshold applied.

are accepted as valid tags, $R_{S/B}$ is approximately 1.2. When the beta energy threshold is applied, $R_{S/B}$ improves significantly, to a value of about 3.

Finally, the tagging efficiency for the beta-neutron detection system was calculated and validated against simulation. The beta-tagging efficiency is defined as the percentage of detected neutrons that are accompanied by a detected beta particle above the 435-keV energy threshold. By subtracting the ^{17}N residual neutron count rate with the beta energy threshold applied from the uncorrelated count rate, the experimental beta-tagging efficiency is $46.5 \pm 4.2\%$. This result agrees with tagging efficiency determined by the Geant4 model, which was $47.7 \pm 0.36\%$. In sum, the beta-neutron coincidence results show that ^{17}N delayed neutrons can be successfully time-tagged using beta particle detection and their timing information can be well-characterized within a given detection system.

5.4 Summary & Future Work

In conclusion, it has been demonstrated that ^{17}N may be used as a source of time-tagged delayed neutrons for calibration. Through measurements of the delayed neutron time profile, ^{17}N production rates were recorded which were consistent with previous experimental measurements of the ^{17}O(n,p)^{17}N reaction cross-section and provide further evidence that ^{17}N can be produced in sufficient quantities for use as a calibration source. Furthermore, ^{17}N beta particles can be efficiently detected and used as a time-tag for delayed neutron emission. The agreement between measured and simulated beta-neutron coincidence time distributions shows that the timing characteristics of ^{17}N are well understood. The ability to tag ^{17}N delayed neutrons may prove useful for large-scale antineutrino detector calibration, as the timing information improves the signal-to-background ratio and allows for more precise calibration of the detector response to IBD-like events.

Additional work was also performed to advance the development efforts for a DT-generator-driven ^{16}N calibration source production system for the WATCHMAN Collaboration. Preliminary ^{16}N production tests were conducted, and the response of large NaI(Tl) detectors to 6.1-MeV gamma rays was successfully modeled for use in future calibration source characterizations. Demonstration of time-tagged gamma rays using ^{16}N beta particles was complicated by high activation rates and ambient ^{16}N production, but future experiments with much longer count times and more favorable configurations may be successful in replicating the results obtained by the SNO Collaboration. As an alternative to DT-generator-driven sources, the combination of ^{241}Am or other high-energy alpha emitters with ^{13}C may provide a source of 6.1-MeV gamma rays without the need for an external neutron source.

In the future, an important aspect of assessing the utility of ^{17}N as a calibration source for large-scale antineutrino detectors will include modeling the detector response to ^{17}N and determining any systematic effects on detector performance metrics. At this

moment, the ultimate detector design that will be implemented by the WATCHMAN Collaboration remains only partially defined, and may be subject to significant future changes. Once the design elements have been finalized, additional work will be needed to model the response characteristics for a ^{17}N source, such as the position resolution, coincidence time distribution, and neutron capture efficiency.

Another interesting question left to future studies involves the potential of ^{17}N as a complementary calibration source for use alongside AmBe. Specifically, one of the systematic considerations involved with an AmBe source stems from the need for a fairly large inorganic crystal to efficiently detect 4.4-MeV gamma rays as a time-tag for emitted neutrons. In Gd-doped detectors, gamma rays from Gd neutron capture events may interact with the tagging detector, leading to a false tag. A diagram illustrating this scenario is shown in Fig. 5.19. Depending on whether the neutron capture pulse is

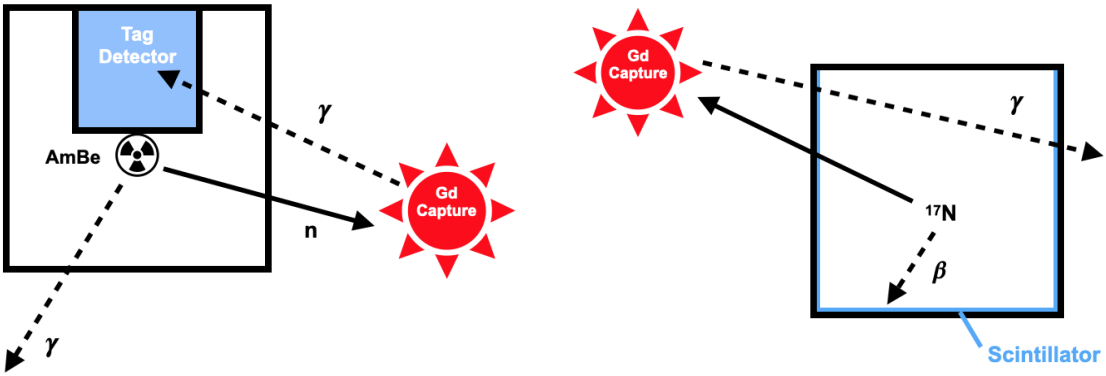

Figure 5.19: *Left:* Tagging systematic diagram for AmBe. *Right:* Tagging systematic diagram for ^{17}N.

detected in the larger detector, this can lead to systematic effects in the measured neutron capture efficiency and coincidence time distribution. Because a ^{17}N calibration system would likely utilize thin layers of plastic scintillator to provide the beta tag, the geometric profile of the source would differ significantly from AmBe, resulting in different systematic effects. By employing both sources for neutron calibration, the systematic effects of any

one source may be mitigated, resulting in a more accurate picture of the detector response overall.

Furthermore, any ^{17}N calibration source is likely to be contaminated with ^{16}N, either from ^{16}O in the target material or the ^{17}O$(n,d)^{16}$N reaction channel. Additional studies are necessary to determine the extent to which ^{16}N betas and gamma rays introduce systematic effects in the detector response to ^{17}N. For example, the 6.1-MeV ^{16}N gamma rays overlap with the Gd neutron capture cascade, as do the ^{16}N and ^{17}N beta energy spectra, which may significantly complicate measurements of the neutron capture efficiency and light output response. However, each isotope exhibits different time-tagging characteristics, as ^{16}N gamma rays will be detected in much closer coincidence with beta emission than ^{17}N neutrons, which must thermalize in the detector medium. The ability to separate the two signals based on their timing information may serve as a good test for IBD event identification in antineutrino detectors.

Finally, further investigation is needed to explore the possibility of ^{241}Am^{13}C as a high-energy gamma-ray calibration source. Production and testing of an experimental source prototype, such as the design outlined in Section 5.3.3, will provide insight on the feasibility of implementing an ^{241}Am^{13}C source with a sufficient gamma-ray emission rate for calibration of a large antineutrino detector. Detailed simulation models may also be useful to determine whether higher-energy alpha emitters, such as ^{238}Pu or ^{244}Cm, may offer an appreciable increase in the gamma ray production rate for the same alpha activity.

Chapter 6

Conclusions and Future Work

6.1 Summary and Conclusions

Just as nuclear energy can provide the power to drive a flourishing society, it can also provide the means for its destruction. The perpetual challenge facing the field of nuclear security and nonproliferation is to strike a balance between promoting and enabling the spread of peaceful nuclear energy technologies and containing the threat posed by nuclear weapons. Toward this end, fast neutron sources and signatures provide invaluable tools to detect and characterize SNM. In this work, applications of fast neutrons as a measurable signal, as well as sources of probing radiation, have been developed to expand the range of tools available for securing and safeguarding nuclear materials.

As a highly penetrating radiation type, fast neutrons are useful for radiographic imaging. Whereas photons are more easily shielded by dense, high-Z materials, neutrons are more easily shielded by low-Z materials. These complementary interaction properties mean that neutron radiography techniques can fill the informational gaps in standard photon-based radiography to strengthen imaging capabilities in treaty verification or cargo screening applications. In the context of SNM detection, the ability to penetrate dense shielding and induce fission signals in the SNM makes neutron-based imaging meth-

ods even more attractive. The combination of neutron transmission imaging and induced fission signatures can provide detailed information for characterizing the geometry and composition of SNM objects. However, in a treaty verification setting, simple, inexpensive, and easy-to-operate systems may be favored over highly sensitive methods that typically involve greater complexity and cost. A simple approach was demonstrated for performing spectroscopic neutron transmission measurements using readily available detection equipment. Geometric profiles were recorded using a crude, 1-D imaging array to detect material diversion. Spectroscopic neutron measurements were also used to confirm fissionable content and detect material diversion by recording the prompt fission neutron rate above a high light-output threshold. The methods demonstrated may be useful in treaty verification scenarios, such as differential measurements in a template-matching system.

Pulsed fast-neutron sources are well-suited to examining the timing characteristics of induced fission signatures. In particular, the temporal profiles of delayed-neutron emission induced by active interrogation can provide the basis for isotopic discrimination and estimation of uranium enrichment. In bulk samples of SNM, this signal is complicated by the interactions of delayed neutrons, which can induce additional fission events within the material. By parsing the delayed-neutron signal to separate the contributions of primary delayed neutrons and the prompt neutrons emitted by delayed-neutron-induced fission, additional information can be obtained to aid in discrimination. Two experimental methods have been demonstrated for differentiating the components of the delayed neutron signal based on fission radiation coincidence counting and measurements of the neutron energy spectrum using capture-gated composite scintillators. Both approaches demonstrate a refinement in the ability to extract information from the delayed neutron signal and apply it to isotopic identification, and may serve a useful complementary role alongside other temporal SNM characterization techniques.

As noted previously, the ability of fast neutrons to penetrate shielding is a key component of their utility. While neutron signals are difficult to shield completely, low-Z moderating materials can effectively obscure the information contained in the neutron energy spectrum. However, due to the short time scale of neutron scattering interactions, long-lived temporal signatures, such as the buildup and decay time profiles of delayed-neutron emission, are resilient to the delays associated with scattering and thermal diffusion. To test this principle, the effects of low-Z shielding on the discrimination of uranium isotopes using delayed neutron time profile measurements were investigated for the first time. It was demonstrated that the delayed neutron time profiles of HEU and DU can be accurately measured in the presence of neutron-moderating shielding. While simulated results showed that neutron reflection by the shielding material can lead to an overestimate of uranium enrichment, the extreme enrichment cases remained easily distinguishable, suggesting that delayed-neutron time profile measurements may offer sufficient resilience to shielding in nonproliferation applications where a binary determination of the presence or absence of HEU is required.

Beyond the use of active interrogation methods in the detection and characterization of SNM, fast-neutron sources are useful for producing a variety of radioisotopes through transmutation. Among these are ^{16}N and ^{17}N, which are attractive as potential calibration sources for large antineutrino detectors due to their emission of time-correlated radiation. In support of the calibration source development efforts for the WATCHMAN Collaboration, ^{16}N production tests were conducted, including modeling of the response of large NaI(Tl) detectors to 6.1-MeV ^{16}N gamma rays. Investigations were conducted to examine the potential use of ^{17}N as a time-tagged neutron calibration source, which could be co-deployed alongside ^{16}N using the same DT-generator-driven production system. Experimental measurements of ^{17}N production were consistent with previous measurements of the ^{17}O$(n,p)^{17}$N reaction cross-section and showed that ^{17}N can be produced in

sufficient quantities for use as a calibration source. The ability to time-tag ^{17}N delayed neutrons was also successfully demonstrated via beta-correlated measurements, including accurate characterization of the time distribution of beta-neutron coincidences in the detection system. These results suggest that ^{17}N may prove useful as a time-tagged neutron calibration source for large antineutrino detectors.

6.2 Future Work

Given the wide range of signals, instrumentation, and measurement methods encompassed in this dissertation, the line of inquiry for future work extend in many different directions. One logical progression would be to investigate the potential application of delayed neutron time profile measurements to other elements and isotopes, such as ^{237}Np and ^{232}Th, which are not specifically classified as SNM but are still of interest in the context of nuclear security. Given the potential of ^{232}Th in particular as a next-generation reactor fuel source, further development of this method is needed to extend safeguards capabilities and improve the understanding of how delayed neutrons influence the observed signal for fissionable materials. In support of this work, capture-gated neutron spectroscopy has been shown to be useful for measuring fast neutron signatures. However, as discussed in Chapter 3, low-energy neutron measurements remain a challenge. Future work is needed to continue developing new detector materials and measurement approaches to improve gamma-ray background rejection and detector sensitivity to extend the applicable range of capture-gated spectroscopy to lower energies, which may improve the ability to record certain fission signatures, such as delayed-neutron energy spectra.

Despite the benefits of fast-neutron sources for penetrating shielding, the characterization of shielded SNM still presents a significant challenge. Although measurements of temporal delayed-neutron signatures have shown a certain degree of shielding-resilience,

future work is needed to fully examine the potential effects on the signal of a broader range of shielding materials, geometric configurations, and SNM compositions. As described in Chapter 4, the results of such studies would be helpful to define the limits of applicability of the measurement method, and may provide new insights on how distortions in the delayed-neutron time profile may be used to glean additional information about the shielding material or configuration. Also, while many of the delayed-neutron measurement methods presented in this dissertation share a common thread of application in the context of treaty verification, other application spaces, such as material accountancy, may benefit from their adoption. Future work may be needed to tailor the methods to the specific challenges presented by other safeguards settings, such as restricted counting times, different material compositions, and variable shielding scenarios.

Finally, the field of rare-event detection provides many opportunities and potential use-cases for radioisotopes developed using fast neutron sources. While the immediate future work for continued development of ^{16}N, ^{17}N, and ^{241}Am^{13}C has been covered in detail in the previous chapter, additional work will be required to address the needs of future detectors that attempt to push the current boundaries of sensitivity and scale. At the multi-kiloton- or megaton-scale masses required for antineutrino detection at very long standoff distances (1000 km or greater), characterization and rejection of background becomes increasingly critical, which will require the development of calibration sources suited to providing a finely-tuned understanding of the detector response. Furthermore, new and innovative antineutrino detector designs are being developed, which may rely on novel detection media, such as opaque scintillators [170]. In the case of opaque scintillators, the unique light transport mechanism may require calibration sources with specialized characteristics to fully probe the detector response. In this regard, the wide variety of radioisotopes made accessible via fast-neutron transmutation may offer some useful options.

References

[1] J. Chadwick, "Possible Existence of a Neutron," *Nature*, vol. 129, no. 312, 1932.

[2] J. Chadwick, "The Existence of a Neutron," *Proceedings of the Royal Society, A*, vol. 136, no. 830, pp. 692–708, 1932.

[3] O. Hahn and F. Strassmann, "Über den Nachweis und das Verhalten der bei der Bestrahlung des Urans mittels Neutronen entstehenden Erdalkalimetalle," *Die Naturwissenshaften*, vol. 27, pp. 11–15, 1939.

[4] L. Meitner and O. R. Frisch, "Disintegration of Uranium by Neutrons: a New Type of Nuclear Reaction," *Nature*, vol. 143, pp. 239–240, 1939.

[5] L. Szilard, "Albert Einstein to F. D. Roosevelt, August 2, 1939."

[6] G. Herken, ""A Most Deadly Illusion": The Atomic Secret and American Nuclear Weapons Policy, 1945-1950," *Pacific Historical Review*, vol. 49, no. 1, pp. 51–76, 1980.

[7] D. A. Rosenberg, "American Atomic Strategy and the Hydrogen Bomb Decision," *Journal of American History*, vol. 66, no. 1, pp. 62–87, 1979.

[8] "The Nuclear Testing Tally," *Arms Control Association*, 2020.

[9] D. Kimball and W. Boese, "Limited Test Ban Treaty Turns 40," *Arms Control Today*, vol. 33, no. 8, pp. 37–38, 2003.

[10] "U.S.-Russian Nuclear Arms Control Agreements at a Glance," *Arms Control Association*, 2020.

[11] "Nuclear Weapons: Who Has What at a Glance," *Arms Control Association*, 2020.

[12] D. B. Thomson, "A Guide to the Nuclear Arms Control Treaties," *Tech. Rep. LA-UR-99-3173, Los Alamos National Laboratory*, 1999.

[13] T. Shanker, "Battle Turns Gentle With Proverbs Galore," *Chicago Tribune*, 1987.

[14] M. I. Kalkstein, "Test Detection by Nuclear Chemistry," *IEEE Transactions on Nuclear Science*, pp. 279–284, 1963.

[15] Bhartendu and B. W. Currie, "Atmospheric Waves From U.S.S.R. Nuclear Test Explosions in 1962," *Canadian Journal of Physics*, vol. 42, 1964.

[16] R. Latter, R. F. Herbst, and K. M. Watson, "Detection of Nuclear Explosions," *Ann. Rev. Nuclear Sci.*, vol. 11, no. June, 1961.

[17] L. J. Carter, "Strategic Weapons : Verification Keeps Ahead of Arms Control," *Science*, vol. 187, no. 4180, pp. 936–939, 1975.

[18] H. Brooks, "The Military Innovation System and the Qualitative Arms Race," *Daedalus*, vol. 104, no. 3, pp. 75–97, 1975.

[19] L. Aspin, "The Verification of the SALT II Agreement," *Scientific American*, vol. 240, no. 2, pp. 38–45, 1979.

[20] J. M. Deutch, "The New Nuclear Threat," *Foreign Affairs*, vol. 71, no. 4, pp. 120–134, 1992.

[21] D. L. Donohue, "Key Tools for Nuclear Inspections: Advances in Environmental Sampling Strengthen Safeguards," *IAEA Bulletin*, vol. 44, no. 2, pp. 17–23, 2002.

[22] M. B. Nikitin, "North Korea's Nuclear Weapons : Technical Issues," *CRS Report for Congress*, 2009.

[23] A. Bernstein, N. Bowden, B. Goldblum, P. Huber, I. Jovanovic, and J. Mattingly, "Colloquium: Neutrino detectors as tools for nuclear security," *Reviews of Modern Physics*, vol. 92, no. 1, p. 11003, 2020.

[24] R. Carr, J. Coleman, M. Danilov, G. Gratta, P. Huber, Y. Hor, T. Kawasaki, S.-b. Kim, Y. Kim, J. Learned, M. Lindner, K. Nakajima, S.-h. Seo, F. Suekane, A. Vacheret, W. Wang, J. Wilhelmi, L. Zhan, R. Carr, J. Coleman, M. Danilov, G. Gratta, P. Huber, Y. Hor, T. Kawasaki, S.-b. Kim, Y. Kim, M. Lindner, K. Nakajima, J. Nikkel, S.-h. Seo, F. Suekane, A. Vacheret, W. Wang, J. Wilhelmi, and L. Zhan, "Neutrino-Based Tools for Nuclear Verification and Diplomacy in North Korea," *Science & Global Security*, vol. 27, no. 1, pp. 15–28, 2019.

[25] R. C. Runkle, "Neutron sensors and their role in nuclear nonproliferation," *Nuclear Instruments and Methods in Physics Research, A*, vol. 652, no. 1, pp. 37–40, 2011.

[26] R. C. Runkle, D. L. Chichester, and S. J. Thompson, "Rattling nucleons: New developments in active interrogation of special nuclear material," *Nuclear Instruments and Methods in Physics Research, A*, vol. 663, no. 1, pp. 75–95, 2012.

[27] I. Jovanovic and A. S. Erickson, *Active Interrogation in Nuclear Security Science, Technology, and Systems*. Springer Verlag, 2018.

[28] V. I. Lushchikov, Y. N. Pokotilovskii, A. V. Strelkov, and F. L. Shapiro, "Observation of Ultracold Neutrons," *Journal of Experimental and Theoretical Physics Letters (USSR) (Engl. Transl.)*, 1969.

[29] T. Dombeck, J. Lynn, S. Werner, T. Brun, J. Carpenter, V. Krohn, and R. Ringo, "Production of Ultra-Cold Neutrons Using Doppler-Shifted Bragg Scattering and an Intense Pulsed Neutron Spallation Source," *Nuclear Instruments and Methods*, vol. 165, pp. 139–155, 1979.

[30] H. Yoshiki, K. Sakai, M. Ogura, T. Kawai, Y. Masuda, T. Nakajima, T. Takayama, S. Tanaka, and A. Yamaguchi, "Observation of Ultracold-Neutron Production by 9-A Cold Neutrons in Superfluid Helium," *Physical Review Letters*, vol. 68, no. 9, pp. 1323–1326, 1992.

[31] G. L. Squires, *Introduction to the Theory of Thermal Neutron Scattering*. Courier Corporation, 1996.

[32] A. Foderaro, *The Elements of Neutron Interaction Theory*. Massachusetts Institute of Technology, 1971.

[33] J. W. Behrens, R. G. Johnson, and R. A. Schrack, "Neutron Resonance Transmission Analysis of Reactor Fuel Samples," *Nuclear Technology*, vol. 67, no. 1, 1984.

[34] P. Schillebeeckx *et al.*, "Neutron resonance spectroscopy for the characterization of materials and objects," *Journal of Instrumentation*, vol. 7, no. C03009, 2012.

[35] B. E. Watt, "Energy Spectrum of Neutrons from Thermal Fission of U235," *Physical Review*, vol. 87, no. 6, 1952.

[36] P. I. Johansson and B. Holmqvist, "An Experimental Study of the Prompt Fission Neutron Spectrum Induced by 0.5-MeV Neutrons Incident on Uranium-235," *Nuclear Science and Engineering*, vol. 62, pp. 695–708, 1976.

[37] D. Reilly, N. Ensslin, H. Smith Jr., and S. Kreiner, *Passive Nondestructive Assay of Nuclear Materials*. Los Alamos National Laboratory, 1991.

[38] R. B. Roberts, R. C. Meyer, and P. Wang, "Further observations on the splitting of uranium and thorium," *Phys. Rev.*, vol. 55, pp. 510–511, Mar 1939.

[39] R. B. Roberts, L. R. Hafstad, R. C. Meyer, and P. Wang, "The delayed neutron emission which accompanies fission of uranium and thorium," *Phys. Rev.*, vol. 55, pp. 664–664, Apr 1939.

[40] N. Bohr and J. A. Wheeler, "The mechanism of nuclear fission," *Phys. Rev.*, vol. 56, pp. 426–450, Sep 1939.

[41] G. R. Keepin, T. F. Wimett, and R. K. Zeigler, "Delayed neutrons from fissionable isotopes of uranium, plutonium, and thorium," *Physical Review*, vol. 6, pp. 1–21, 1957.

[42] M. L. E. Oliphant, P. Harteck, and E. Rutherford, "Transmutation Effects Observed with Heavy Hydrogen," *Proceedings of the Royal Society of London, Series A*, vol. 144, no. 853, pp. 692–703, 1934.

[43] J. E. Bounden, P. D. Lomer, and J. D. L. H. Wood, "A Neutron Tube with Constant Output (10^{10} n/sec) for Activation Analysis and Reactor Applications," *Nuclear Instruments and Methods*, vol. 33, 1965.

[44] J. Reijonen, F. Gicquel, S. K. Hahto, M. King, T. Lou, and K. Leung, "D – D neutron generator development at LBNL," *Applied Radiation and Isotopes*, vol. 63, pp. 757–763, 2005.

[45] K. N. Leung, J. Reijonen, F. Gicquel, S. Hahto, and T. P. Lou, "Compact Neutron Generator Development and Applications," in *The World Conference on Non-Destructive Testing (WCNDT 2004)*, (Montreal, Canada), 2004.

[46] S. D. Clarke, B. M. Wieger, A. Enqvist, R. Vogt, J. Randrup, R. C. Haight, H. Y. Lee, B. A. Perdue, E. Kwan, C. Y. Wu, R. A. Henderson, and S. A. Pozzi, "Measurement of the energy and multiplicity distributions of neutrons from the photofission of 235U," *Physical Review C*, vol. 95, no. 064612, 2017.

[47] D. J. S. Findlay, "Applications of Photonuclear Reactions," *Nuclear Instruments and Methods and Methods in Physics Research B*, vol. 50, pp. 314–320, 1990.

[48] G. S. Bauer, "Physics and technology of spallation neutron sources," *Nuclear Instruments and Methods and Methods in Physics Research A*, vol. 463, pp. 505–543, 2001.

[49] J. Alvarez, J. Fernandez-Tobias, K. Mima, S. Nakai, S. Kar, Y. Kato, and J. Perlado, "Laser Driven Neutron Sources: Characteristics, Applications and Prospects," *Physics Procedia*, vol. 60, pp. 29–38, 2014.

[50] F. Sutanto, O. A. Akindele, M. Askins, M. Bergevin, A. Bernstein, N. S. Bowden, S. Dazeley, P. Jaffke, I. Jovanovic, S. Quillin, C. Roecker, and S. D. Rountree, "Measurement of muon-induced high-energy neutrons from rock in an underground Gd-doped water detector," *Physical Review C*, vol. 102, no. 034616, 2020.

[51] P. E. Garrett, N. Warr, and S. W. Yates, "Nuclear Structure Studies with the Inelastic Neutron Scattering Reaction and Gamma-Ray Detection," *Journal of Research of the National Institute of Standards and Technology*, vol. 105, no. 1, pp. 141–145, 2000.

[52] A. Buffler and J. Tickner, "Detecting contraband using neutrons: Challenges and future directions," *Radiation Measurements*, vol. 45, pp. 1186–1192, 2010.

[53] G. F. Knoll, *Radiation Detection and Measurement*. John Wiley & Sons, 4th ed., 2010.

[54] F. W. K. Firk, G. G. Slaughter, and R. J. Ginther, "An Improved Li6-Loaded Glass Scintillator for Neutron Detection," *Nuclear Instruments and Methods*, vol. 13, pp. 313–316, 1961.

[55] C. D. Bass, E. J. Beise, H. Breuer, C. R. Heimbach, T. J. Langford, and J. S. Nico, "Characterization of a 6Li-loaded liquid organic scintillator for fast neutron spectrometry and thermal neutron detection," *Applied Radiation and Isotopes*, vol. 77, pp. 130–138, 2013.

[56] J. Birks, *Theory and Practice of Scintillation Counting*. Pergamon Press, 1964.

[57] D. L. Smith, R. G. Polk, and T. G. Miller, "Measurement of the response of several organic scintillators to electrons, protons and deuterons," *Nuclear Instruments and Methods*, vol. 64, no. 2, pp. 157–166, 1968.

[58] R. L. Craun and D. L. Smith, "Analysis of Response Data for Several Organic Scintillators," *Nuclear Instruments and Methods*, vol. 80, no. 2, pp. 239–244, 1970.

[59] F. D. Brooks, "A Scintillation Counter with Neutron and Gamma-Ray Discriminators," *Nuclear Instruments and Methods*, vol. 4, pp. 151–163, 1959.

[60] N. Zaitseva, B. L. Rupert, I. Pawe, A. Glenn, H. P. Martinez, L. Carman, M. Faust, N. Cherepy, and S. Payne, "Plastic scintillators with efficient neutron/gamma pulse shape discrimination," *Nuclear Instruments and Methods in Physics Research A*, vol. 668, pp. 88–93, 2012.

[61] A. DiFulvio, T. H. Shin, T. Jordan, C. Sosa, M. L. Ruch, S. D. Clarke, D. L. Chichester, and S. A. Pozzi, "Passive assay of plutonium metal plates using a fast-neutron multiplicity counter," *Nuclear Inst. and Methods in Physics Research, A*, vol. 855, pp. 92–101, 2017.

[62] J. Manfredi *et al.*, "The single-volume scatter camera," in *Proc. SPIE 11494, Hard X-Ray, Gamma-Ray, and Neutron Detector Physics XXII*, vol. 114940V, 2020.

[63] P. Hausladen, J. Newby, F. Liang, and M. Blackston, "The Deployable Fast-Neutron Coded- Aperture Imager : Demonstration of Locating One or More Sources in Three Dimensions," *Tech. Rep. ORNL/TM-2013/446*, 2013.

[64] N. P. Shah, J. Vanderzanden, and D. K. Wehe, "Design and construction of a 1-D, cylindrical, dual-particle, time-encoded imaging system," *Nuclear Inst. and Methods in Physics Research, A*, vol. 954, p. 161785, 2020.

[65] J. Nattress, *Discriminating Materials Using a Multi-particle Approach in an Active Interrogation Environment*. PhD thesis, University of Michigan, 2018.

[66] C. C. Lawrence, A. Enqvist, M. Flaska, S. A. Pozzi, and F. D. Becchetti, "Comparison of spectrum-unfolding performance of (EJ315) and (EJ309) liquid scintillators on measured 252Cf pulse-height spectra," *Nuclear Instruments and Methods and Methods in Physics Research A*, vol. 729, pp. 924–929, 2013.

[67] M. Bruggeman, P. Baeten, W. D. Boeck, and R. Carchon, "Neutron coincidence counting based on time interval analysis with one- and two-dimensional Rossi-alpha distributions: an application for passive neutron waste assay," *Nuclear Instruments and Methods and Methods in Physics Research A*, vol. 382, pp. 511–518, 1996.

[68] J. H. Scatliff and P. J. Morris, "From Röntgen to Magnetic Resonance Imaging: The History of Medical Imaging," *North Carolina Medical Journal*, vol. 75, no. 2, pp. 111–113, 2014.

[69] R. C. Koch, *Activation Analysis Handbook*. Academic Press, 1960.

[70] S. C. Van Der Marck, A. J. Koning, and K. E. Charlton, "The options for the future production of the medical isotope 99Mo," *European Journal of Nuclear Medicine and Molecular Imaging*, vol. 37, pp. 1817–1820, 2010.

[71] A. P. Kushelevsky, Z. B. Alfassi, T. Schlesinger, and W. Wolfs, "14 MeV Neutron Generators for Radionuclide Production," *International Journal of Applied Radiation and Isotopes*, vol. 30, pp. 275–278, 1979.

[72] K. Ogren, J. Nattress, and I. Jovanovic, "Spectroscopic fast neutron transmission imaging in a treaty verification setting," *AIP Advances*, vol. 8, no. 015205, 2018.

[73] C. Comley, M. Comley, P. Eggins, G. George, S. Holloway, M. Ley, P. Thompson, and K. Warburton, *Confidence, Security & Verification: The challenge of global nuclear weapons arms control*. Reading, UK: Atomic Weapos Establishment, 2000.

[74] R. T. Kouzes and J. L. Fuller, "Authentication of monitoring systems for nonproliferation and arms control," in *Proceedings of Symposium on International Safeguards: Verification and Nuclear Material Security*, no. October, (Vienna, Austria), International Atomic Energy Agency, 2001.

[75] A. Glaser, B. Barak, and R. J. Goldston, "A zero-knowledge protocol for nuclear warhead verification," *Nature*, vol. 510, no. 7506, pp. 497–502, 2014.

[76] C. J. Macgahan, M. A. Kupinski, E. M. Brubaker, N. R. Hilton, and P. A. Marleau, "Linear models to perform treaty verification tasks for enhanced information security," *Nuclear Instruments and Methods in Physics Research, A*, vol. 844, no. November 2016, pp. 147–157, 2017.

[77] D. Spears, ed., *Technology R & D for Arms Control*. Washington DC: US Department of Energy, Office of Nonproliferation Research and Engineering, 2001.

[78] J. T. Mihalczo, V. K. Pare, E. D. Blakeman, B. Damiano, T. E. Valentine, L. D. Phillips, R. B. Banner, D. B. Bopp, T. R. Chilcoat, J. Declue, E. P. Elliott, G. D. Hackett, N. W. Hill, D. J. Nypaver, L. H. Thacker, W. T. Thomas, J. A. Williams, and R. E. Zumstein, "NWIS Signatures for Confirmatory Measurements With B33 Trainers," *Journal of Nuclear Materials Management*, vol. 25, no. 3, 1997.

[79] J. T. Mihalczo, T. E. Valentine, J. K. Mattingly, J. A. Mullens, and S. S. Hughes, "Active Neutron Interrogation for Verification of Storage of Weapons Components at the Oak Ridge Y-12 Plant," *Tech. Rep. YLB-15-964*, 1998.

[80] P. B. Rose, A. S. Erickson, M. Mayer, J. Nattress, and I. Jovanovic, "Uncovering Special Nuclear Materials by Low-energy Nuclear Reaction Imaging.," *Scientific reports*, vol. 6, no. April, p. 24388, 2016.

[81] J. Rahon, A. Danagoulian, T. D. Macdonald, Z. S. Hartwig, and R. C. Lanza, "Spectroscopic neutron radiography for a cargo scanning system," *Nuclear Instruments and Methods in Physics Research, A*, vol. 820, pp. 141–145, 2016.

[82] S. V. Naydenov, V. D. Ryzhikov, and C. F. Smith, "Direct reconstruction of the effective atomic number of materials by the method of multi-energy radiography," *Nuclear Instruments and Methods in Physics Research, B*, vol. 215, pp. 552–560, 2004.

[83] T. A. Wellington, B. A. Palles, J. A. Mullens, J. T. Mihalczo, D. E. Archer, T. Thompson, C. L. Britton, N. D. Bull Ezell, M. N. Ericson, E. Farquhar, R. Lind, and J. Carter, "Recent Fast Neutron Imaging Measurements with the Fieldable Nuclear Materials Identification System," *Physics Procedia*, vol. 66, pp. 432–438, 2015.

[84] P. A. Hausladen, P. R. Bingham, J. S. Neal, J. A. Mullens, and J. T. Mihalczo, "Portable fast-neutron radiography with the nuclear materials identification system for fissile material transfers," *Nuclear Instruments and Methods in Physics Research B*, vol. 261, pp. 387–390, 2007.

[85] P. A. Hausladen, M. A. Blackston, E. Brubaker, D. L. Chichester, P. Marleau, and R. J. Newby, "Fast-Neutron Coded-Aperture Imaging of Special Nuclear Material Configurations," *Tech. Rep. INL/CON-12-26506, Idaho National Laboratory*, 2012.

[86] P. A. Hausladen, M. A. Blackston, and J. Newby, "Demonstration of Emitted-Neutron Computed Tomography to Quantify Nuclear Materials," *Tech. Rep. ORNL/TM-2011/357*, no. September, 2011.

[87] P. A. Hausladen, M. A. Blackston, J. Mullens, S. Mcconchie, J. T. Mihalczo, P. R. Bingham, M. N. Ericson, and L. Fabris, "Induced-Fission Imaging of Nuclear Material Induced," in *INMM 51st Annual Meeting*, (Oak Ridge, Tennessee), Oak Ridge National Laboratory, 2010.

[88] S. M. Robinson, K. D. Jarman, W. K. Pitts, A. Seifert, A. C. Misner, M. L. Woodring, and M. J. Myjak, "Imaging for dismantlement verification : Information management and analysis algorithms," *Nuclear Instruments and Methods in Physics Research, A*, vol. 662, no. 1, pp. 81–89, 2012.

[89] N. Ensslin, M. S. Krick, D. G. Langner, and M. C. Miller, "Active Neutron Multiplicity Counting of Bulk Uranium," *Tech. Rep. LA-UR-91-2470, Los Alamos National Laboratory*, 1991.

[90] I. Israelashvili, C. Dubi, H. Ettedgui, A. Ocherashvili, B. Pedersen, A. Beck, E. Roesgen, J. M. Crochmore, T. Ridnik, and I. Yaar, "Fissile mass estimation by pulsed neutron source interrogation," *Nuclear Instruments and Methods in Physics Research, A*, vol. 785, pp. 14–20, 2015.

[91] R. E. Rothe, "Extrapolated Experimental Critical Parameters of Unreflected and Steel-Reflected Massive Enriched Uranium Metal Spherical and Hemispherical Assemblies," *Tech. Rep INEEL/EXT-97-01401, Lockheed Idaho Technologies Co., Idaho National Engineering and Environmental Lab.*, 1997.

[92] S. Agostinelli *et al.*, "Geant4—a simulation toolkit," *Nuclear Instruments and Methods in Physics Research, A*, vol. 506, no. 3, pp. 250–303, 2003.

[93] "NEUTRON / GAMMA PSD LIQUID SCINTILLATOR EJ301, EJ309," 2016.

[94] A. Enqvist, C. C. Lawrence, B. M. Wieger, S. A. Pozzi, and T. N. Massey, "Neutron light output response and resolution functions in EJ-309 liquid scintillation detectors," *Nuclear Instruments and Methods in Physics Research, A*, vol. 715, pp. 79–86, 2013.

[95] G. Dietze and H. Klein, "GAMMA-CALIBRATION OF NE 213 SCINTILLATION COUNTERS," *Nuclear Instruments and Methods*, vol. 193, pp. 549–556, 1982.

[96] J. R. Verbus, C. A. Rhyne, D. C. Malling, M. Genecov, S. Ghosh, A. G. Moskowitz, S. Chan, J. J. Chapman, L. de Viveiros, C. H. Faham, S. Fiorucci, D. Q. Huang, M. Pangilinan, W. C. Taylor, and R. J. Gaitskell, "Proposed low-energy absolute calibration of nuclear recoils in a dual-phase noble element TPC using D-D neutron scattering kinematics," *Nuclear Instruments and Methods in Physics Research, A*, vol. 851, pp. 68–81, aug 2016.

[97] R. Remetti, L. Lepore, and N. Cherubini, "Development and experimental validation of a monte carlo modeling of the neutron emission from a d-t generator,"

Nuclear Instruments and Methods in Physics Research, A, vol. 842, no. March 2016, pp. 7–13, 2017.

[98] M. B. Chadwick, M. Herman, P. Oblozinsky, B. Pritychenko, G. Arbanas, R. Arcilla, R. Brewer, D. A. Brown, R. Capote, A. D. Carlson, Y. S. Cho, H. Derrien, K. Guber, G. M. Hale, S. Hoblit, S. Holloway, T. D. Johnson, T. Kawano, B. C. Kiedrowski, H. Kim, S. Kunieda, N. M. Larson, L. Leal, J. P. Lestone, R. C. Little, E. A. Mccutchan, R. E. Macfarlane, M. Macinnes, C. M. Mattoon, R. D. Mcknight, S. F. Mughabghab, G. P. A. Nobre, G. Palmiotti, A. Palumbo, M. T. Pigni, V. G. Pronyaev, R. L. Vogt, S. C. van der Marck, A. Wallner, M. C. White, D. Wiarda, and P. G. Young, "ENDF / B-VII . 1 Nuclear Data for Science and Technology : Cross Sections , Covariances , Fission Product Yields and Decay Data," *Nuclear Data Sheets*, vol. 112, pp. 2887–2996, 2011.

[99] D. G. Madland, "New Fission-Neutron-Spectrum Representation for ENDF," *Tech. Rep. LA-9285-MS, Los Alamos National Laboratory*, no. April, 1982.

[100] R. McConn Jr, C. Gesh, R. Pagh, R. Rucker, and R. Williams III, "Compendium of Material Composition Data for Radiation Transport Modeling," *Tech. Rep. PIET-43741-TM-963, Pacific Northwest National Laboratory*, 2011.

[101] J. Nattress, K. Ogren, A. Foster, A. Meddeb, Z. Ounaies, and I. Jovanovic, "Discriminating Uranium Isotopes Using the Time-Emission Profiles of Long-Lived Delayed Neutrons," *Physical Review Applied*, vol. 10, no. 2, 2018.

[102] K. Ogren, J. Nattress, and I. Jovanovic, "Discriminating uranium isotopes based on fission signatures induced by delayed neutrons," *Phys. Rev. Applied*, vol. 14, p. 014033, Jul 2020.

[103] R. Berndt, E. Franke, and P. Mortreau, "^{235}U enrichment or UF_6 mass determination on UF_6 cylinders with non-destructive analysis methods," *Nuclear Instruments and Methods in Physics Research A*, vol. 612, no. 2, pp. 309–319, 2010.

[104] R. C. Runkle, A. Bernstein, and P. E. Vanier, "Securing special nuclear material: Recent advances in neutron detection and their role in nonproliferation," *Journal of Applied Physics*, vol. 108, no. 11, 2010.

[105] K. H. Beckurts, "Measurements with a Pulsed Neutron Source," *Nuclear Science and Engineering*, vol. 2, no. 4, pp. 516–522, 1957.

[106] J. T. Caldwell and W. E. Kunz, "Experimental Evaluation of the Differential Die-Away Pulsed-Neutron Technique for the Fissile Assay of Hot Irradiated Fuel Waste," *Tech. Rep. No. LA-UR-82-788, Los Alamos National Laboratory*, 1982.

[107] K. A. Jordan and T. Gozani, "Pulsed neutron differential die away analysis for detection of nuclear materials," *Nuclear Instruments and Methods in Physics Research, B*, vol. 261, pp. 365–368, 2007.

[108] S. Amiel, "Analytical Applications of Delayed Neutron Emission in Fissionable Elements," *Analytical Chemistry*, vol. 34, no. 13, pp. 1683–1692, 1962.

[109] G. R. Keepin, "Nuclear safeguards research and development," *Tech. Rep. No. LA-4368-MS, Los Alamos National Laboratory*, 1969.

[110] J. L. Jones, K. J. Haskell, J. M. Hoggan, D. R. Norman, and W. Y. Yoon, "Photonuclear-based Detection of Nuclear Smuggling in Cargo Containers," in *AIP Conference Proceedings*, vol. 680, pp. 947–950, 2003.

[111] D. Slaughter, M. Accatino, A. Bernstein, J. Candy, A. Dougan, J. Hall, A. Loshak, D. Manatt, A. Meyer, B. Pohl, S. Prussin, R. Walling, and D. Weirup, "Detection of special nuclear material in cargo containers using neutron interrogation," *Tech. Rep. No. UCRL-ID-155315, Lawrence Livermore National Laboratory*, no. August, 2003.

[112] D. L. Chichester and E. H. Seabury, "Addressing different active neutron interrogation signatures from fissionable material," in *IEEE Nuclear Science Symposium Conference Record (NSS/MIC)*, pp. 956–960, 2009.

[113] M. Mayer, J. Nattress, and I. Jovanovic, "Detection of special nuclear material from delayed neutron emission induced by a dual-particle monoenergetic source," *Applied Physics Letters*, vol. 108, no. 26, p. 264102, 2016.

[114] M. T. Kinlaw and A. W. Hunt, "Fissionable isotope identification using the time dependence of delayed neutron emission," *Nuclear Instruments and Methods in Physics Research, Section A: Accelerators, Spectrometers, Detectors and Associated Equipment*, vol. 562, pp. 1081–1084, 2006.

[115] X. Li, R. Henkelmann, and F. Baumgärtner, "Rapid determination of uranium and plutonium content in mixtures through measurement of the intensity-time curve of delayed neutrons," *Nuclear Instruments and Methods in Physics Research B*, vol. 215, pp. 246–251, 2004.

[116] W. L. Myers, C. A. Goulding, and C. L. Hollas, "Determination of the 235 U Enrichment of Bulk Uranium Samples Using Delayed Neutrons," *Tech. Rep. No. LA-UR-06-3984, Los Alamos National Laboratory*, 2006.

[117] M. T. Sellers, D. G. Kelly, and E. C. Corcoran, "An automated delayed neutron counting system for mass determinations of special nuclear materials," *Journal of Radioanalytical and Nuclear Chemistry*, vol. 291, no. 2, pp. 281–285, 2012.

[118] S. Shalev and J. M. Cuttler, "The Energy Distribution of Delayed Fission Neutrons," *Nuclear Science and Engineering*, vol. 51, no. 1, pp. 52–66, 1973.

[119] R. Batchelor and H. R. M. Hyder, "The Energy of Delayed Neutrons from Fission," *Journal of Nuclear Energy*, vol. 3, pp. 7–17, 1956.

[120] C. L. Morris, K. Chung, S. Greene, G. Hogan, M. Makela, F. Mariam, E. C. Milner, M. Murray, A. Saunders, R. Spaulding, Z. Wang, L. Waters, and F. Wysocki, "Active Interrogation Using Energetic Protons," *Tech. Rep. LA-UR-10-04680, Los Alamos National Laboratory*, 2010.

[121] M. Mayer, J. Nattress, V. Kukharev, A. Foster, A. Meddeb, C. Trivelpiece, Z. Ounaies, and I. Jovanovic, "Development and characterization of a neutron detector based on a lithium glass-polymer composite," *Nuclear Instruments and Methods in Physics Research A*, vol. 785, pp. 117–122, 2015.

[122] T. Shi, J. Nattress, M. Mayer, M. W. Lin, and I. Jovanovic, "Neutron spectroscopy by thermalization light yield measurement in a composite heterogeneous scintillator," *Nuclear Instruments and Methods in Physics Research, A*, vol. 839, no. September, pp. 86–91, 2016.

[123] J. Nattress, M. Mayer, A. Foster, A. Barhoumi Meddeb, C. Trivelpiece, Z. Ounaies, and I. Jovanovic, "Capture-gated Spectroscopic Measurements of Monoenergetic Neutrons with a Composite Scintillation Detector," *IEEE Transactions on Nuclear Science*, vol. 63, no. 2, pp. 1227–1235, 2016.

[124] "User Manual - UM5960 CoMPASS Multiparametric DAQ Software for Physics Applications," May 2018.

[125] S. A. Pozzi, S. D. Clarke, W. J. Walsh, E. C. Miller, J. L. Dolan, M. Flaska, B. M. Wieger, A. Enqvist, E. Padovani, J. K. Mattingly, D. L. Chichester, and P. Peerani, "MCNPX-PoliMi for nuclear nonproliferation applications," *Nuclear Instruments and Methods in Physics Research A*, vol. 694, pp. 119–125, 2012.

[126] L. Cranberg, G. Frye, N. Nereson, and L. Rosen, "Fission Neutron Spectrum of U235," *Physical Review*, vol. 103, no. 3, pp. 662–670, 1956.

[127] J. Nattress and I. Jovanovic, "Response and calibration of organic scintillators for gamma-ray spectroscopy up to 15-MeV range," *Nuclear Instruments and Methods in Physics Research, A*, vol. 871, no. July, pp. 1–7, 2017.

[128] K. Ogren, T. Wu, J. Nattress, and I. Jovanovic, "The effects of low-Z shielding on uranium isotope discrimination using the time-emission profiles of long-lived delayed neutrons," *Nuclear Instruments and Methods and Methods in Physics Research A*, vol. 1019, 2021.

[129] S. Fetter, V. A. Frolov, M. Miller, R. Mozley, O. F. Prilutsky, S. N. Rodionov, and R. Z. Sagdeev, "Detecting Nuclear Warheads," *Science & Global Security*, vol. 1, pp. 225–253, 1990.

[130] R. T. Kouzes, "Detecting Illicit Nuclear Materials: The installation of radiological monitoring equipment in the United States and overseas is helping thwart nuclear terrorism," *American Scientist*, vol. 93, no. 5, pp. 422–427, 2005.

[131] R. T. Kouzes, E. R. Siciliano, J. H. Ely, P. E. Keller, and R. J. Mcconn, "Passive neutron detection for interdiction of nuclear material at borders," *Nuclear Instruments and Methods in Physics Research A*, vol. 584, pp. 383–400, 2007.

[132] D. L. Chichester and E. H. Seabury, "Active Neutron Interrogation to Detect Shielded Fissionable Material," in *International Topical Meeting on Nuclear Research Applications and Utilization of Accelerators*, pp. 1–9, Idaho National Laboratory, 2009.

[133] A. L. Lousteau, R. D. Mcelroy, S. Croft, and J. P. Hayward, "Determining 235U enrichment in bulk uranium items using dual-energy interrogation with delayed neutron measurement," *Nuclear Instruments and Methods in Physics Research, A*, vol. 904, no. July, pp. 74–80, 2018.

[134] C. L. Hollas, C. Goulding, and B. Myers, "Non Destructive Analysis of Shielded Highly Enriched Uranium," *Tech. Rep. LA-UR-01-5852, Los Alamos National Laboratory*, 2001.

[135] C. E. Moss, M. W. Brener, C. L. Hollas, and W. L. Myers, "Portable active interrogation system," *Nuclear Instruments and Methods in Physics Research B*, vol. 241, pp. 793–797, 2005.

[136] M. B. Chadwick, M. Herman, P. Oblozinsky, B. Pritychenko, G. Arbanas, R. Arcilla, R. Brewer, D. A. Brown, R. Capote, A. D. Carlson, Y. S. Cho, H. Derrien, K. Guber, G. M. Hale, S. Hoblit, S. Holloway, T. D. Johnson, T. Kawano, B. C. Kiedrowski, H. Kim, S. Kunieda, N. M. Larson, L. Leal, J. P. Lestone, R. C. Little, E. A. Mccutchan, R. E. Macfarlane, M. Macinnes, C. M. Mattoon, R. D. Mcknight, S. F. Mughabghab, G. P. A. Nobre, G. Palmiotti, A. Palumbo, M. T. Pigni, V. G. Pronyaev, R. L. Vogt, S. C. van der Marck, A. Wallner, M. C. White, D. Wiarda, and P. G. Young, "ENDF / B-VII.1 Nuclear Data for Science and Technology : Cross Sections , Covariances , Fission Product Yields and Decay Data," *Nuclear Data Sheets*, vol. 112, pp. 2887–2996, 2011.

[137] T. C. Wu, T. Shi, and I. Jovanovic, "Compound pulse characteristics of a heterogeneous composite scintillator in a gamma-ray field," *Nuclear Instruments and Methods in Physics Research A*, vol. 976, 2020.

[138] *DT5730 User Manual - UM3148.* CAEN, December 2014.

[139] D. Saphier, D. Ilberg, S. Shalev, and S. Yiftah, "Evaluated Delayed Neutron Spectra and Their Importance in Reactor Calculations," *Nuclear Science and Engineering*, vol. 62, no. 4, pp. 660–694, 1977.

[140] T. Goorley, M. James, T. Booth, F. Brown, J. Bull, L. J. Cox, J. Durkee, J. Elson, M. Fensin, R. A. Forster, J. Hendricks, H. G. Hughes, R. Johns, B. Kiedrowski, S. Mashnik, G. Mckinney, D. Pelowitz, R. Prael, J. Sweezy, L. Waters, T. Zukaitis,

G. Mckinney, D. Pelowitz, R. Prael, J. Sweezy, L. Waters, T. Wilcox, and T. Zukaitis, "Initial MCNP6 Release Overview," *Nuclear Technology*, vol. 180, no. 3, pp. 298–315, 2012.

[141] A. A. Borovoi and L. A. Mikaelyan, "Possibilities of the practical use of neutrinos," *Soviet Atomic Energy*, vol. 44, no. 6, pp. 589–592, 1978.

[142] Y. V. Klimov, V. I. Kopeikin, L. A. Mikaelyan, K. V. Ozerov, and V. V. Sinev, "Neutrino method remote measurement of reactor power and power output," *Atomic Energy*, vol. 76, no. 2, pp. 123–127, 1994.

[143] N. S. Bowden, A. Bernstein, M. Allen, J. S. Brennan, M. Cunningham, J. K. Estrada, C. M. R. Greaves, C. Hagmann, J. Lund, W. Mengesha, T. D. Weinbeck, and C. D. Winant, "Experimental results from an antineutrino detector for cooperative monitoring of nuclear reactors," *Nuclear Instruments and Methods and Methods in Physics Research, A*, vol. 572, pp. 985–998, 2007.

[144] A. Bernstein, N. S. Bowden, A. C. Misner, and T. Palmer, "Monitoring the thermal power of nuclear reactors with a prototype cubic meter antineutrino detector," *Journal of Applied Physics*, vol. 103, no. 074905, 2008.

[145] N. S. Bowden, A. Bernstein, S. Dazeley, R. Svoboda, A. C. Misner, and T. Palmer, "Observation of the isotopic evolution of pressurized water reactor fuel using an antineutrino detector," *Journal of Applied Physics*, vol. 105, no. 064902, 2009.

[146] A. Bernstein, T. West, and V. Gupta, "An Assessment of Antineutrino Detection as a Tool for Monitoring Nuclear Explosions," *Science & Global Security*, vol. 9, no. 3, pp. 235–255, 2001.

[147] M. Askins *et. al.* (WATCHMAN Collaboration), "The Physics and Nuclear Nonproliferation Goals of WATCHMAN: A WAter CHerenkov Monitor for ANtineutrinos." arXiv:1502.01132v1, 2015.

[148] C. L. Cowan, F. Reines, F. B. Harris, H. W. Kruse, and A. D. McGuire, "Detection of the Free Neutrino : a Confirmation," *Science*, vol. 124, no. 3212, pp. 103–104, 1956.

[149] J. F. Beacom and M. R. Vagins, "Antineutrino spectroscopy with large water Čerenkov detectors," *Phys. Rev. Lett.*, vol. 93, p. 171101, 2004.

[150] K. Hagiwara, T. Yano, T. Tanaka, M. S. Reen, T. Mori, T. Kayano, R. Dhir, Y. Koshio, M. Sakuda, A. Kimura, S. Nakamura, N. Iwamoto, H. Harada, M. Wurm, W. Focillon, M. Gonin, A. Ali, and G. Collazuol, "Gamma-ray spectrum from thermal neutron capture on gadolinium-157," *Progress of Theoretical and Experimental Physics*, vol. 2019, no. 2, 2019.

[151] E. Blaufuss *et al.*, "16N as a calibration source for Super-Kamiokande," *Nuclear Instruments and Methods and Methods in Physics Research, A*, vol. 458, pp. 638–649, 2001.

[152] M. R. Dragowsky, A. Hamer, Y. D. Chan, R. Deal, E. D. Earle, W. Frati, E. Gaudette, A. Hallin, C. Hearns, J. Hewett, G. Jonkmans, Y. Kajiyama, A. B. McDonald, B. A. Moffat, E. B. Norman, B. Sur, and N. Tagg, "The 16N calibration source for the Sudbury Neutrino Observatory," *Nuclear Instruments and Methods in Physics Research A*, vol. 481, pp. 284–296, 2002.

[153] M. Askins, "WATCHMAN Calibration Requirements." Personal Communication, 2021.

[154] A. R. Poletti and J. G. Pronko, "No Title," *Physical Review C*, vol. 8, no. 4, 1973.

[155] B. E. Berger *et al.*, "The KamLAND full-volume calibration system," *Journal of Instrumentation*, vol. 4, no. P04017, 2009.

[156] B. Aharmim *et. al.* (SNO Collaboration), "Combined analysis of all three phases of solar neutrino data from the Sudbury Neutrino Observatory," *Physical Review C*, vol. 88, no. 025501, 2013.

[157] B. Caccianiga and A. C. Re, "Calibration of the solar neutrino detectors," *European Physical Journal A*, vol. 52, no. 80, 2016.

[158] M. Sweany, A. Bernstein, N. S. Bowden, S. Dazeley, G. Keefer, R. Svoboda, and M. Tripathi, "Large-scale gadolinium-doped water Cherenkov detector for nonproliferation," *Nuclear Instruments and Methods and Methods in Physics Research A*, vol. 654, pp. 377–382, 2011.

[159] E. B. Norman and B. Sur, "17N: A Tagged Neutron Source for SNO," *Tech. Rep. SNO-STR-94-037*, 1994.

[160] B. Sur and E. D. Earle, "Gas Transport Calibration System for SNO: A Preliminary Design Document," *Tech. Rep. SNO-STR-95-053*, 1995.

[161] E. B. Norman and B. Sur, "Cross sections for the 17O(n,p)17N and 17O(n,d)16N reactions at 14 MeV," *Physical Review C*, vol. 57, no. 4, pp. 2043–2045, 1998.

[162] P. Mohr, "Revised cross section of the 13C(α,n)16O reaction between 5 and 8 MeV," *Physical Review C*, vol. 97, p. 064613, 2018.

[163] J. Liu, R. Carr, D. A. Dwyer, W. Q. Gu, G. S. Li, R. D. Mckeown, X. Qian, R. H. M. Tsang, F. F. Wu, and C. Zhang, "Neutron calibration sources in the Daya Bay experiment," *Nuclear Instruments and Methods in Physics Research A*, vol. 797, pp. 260–264, 2015.

[164] P. Agnes *et al.*, "Calibration of the liquid argon ionization response to low energy electronic and nuclear recoils with DarkSide-50," *Physical Review D*, vol. 104, no. 082005, 2021.

[165] M. Berger, J. Coursey, and M. Zucker, "ESTAR, PSTAR, and ASTAR: Computer Programs for Calculating Stopping-Power and Range Tables for Electrons, Protons, and Helium Ions (version 1.21)," 1999-01-01 1999.

[166] T. Murata, H. Matsunobu, and K. Shibata, "Evaluation of the (α, xn) Reaction Data for JENDL/AN-2005," *JAEA-Research 2006-052*, 2006.

[167] A. J. M. Plompen *et al.*, "The joint evaluated fission and fusion nuclear data library, JEFF-3.3," *The European Physical Journal A*, vol. 56, no. 7, pp. 1–108, 2020.

[168] D. A. Brown *et al.*, "ENDF/B-VIII.0: The 8th Major Release of the Nuclear Reaction Data Library with CIELO-project Cross Sections, New Standards and Thermal Scattering Data," *Nuclear Data Sheets*, vol. 148, pp. 1–142, 2018.

[169] A. J. Koning, D. Rochman, J. Sublet, N. Dzysiuk, M. Fleming, and S. V. D. Marck, "TENDL: Complete Nuclear Data Library for Innovative Nuclear Science and Technology," *Nuclear Data Sheets*, vol. 155, pp. 1–55, 2019.

[170] A. Cabrera *et al.*, "Neutrino Physics with an Opaque Detector." arXiv:1908.02859v1, 2019.